CHARACTERIZATION OF INGAAS/INP HETEROSTRUCTURE NANOWIRES

CHARACTERIZATION OF INGAAS/INP HETEROSTRUCTURE NANOWIRES GROWN BY GAS SOURCE MOLECULAR BEAM EPITAXY

By

DAVID M. CORNET, B.Sc. Engineering Physics

A Thesis
Submitted to the School of Graduate Studies
in Partial Fulfillment of the Requirements
for the Degree
Master of Applied Science

McMaster University

MASTER OF APPLIED SCIENCE (2007) McMaster University

(Engineering Physics) Hamilton, Ontario

TITLE: Characterization of InGaAs/InP Heterostructure Nanowires Grown by Gas Source Molecular Beam Epitaxy

AUTHOR: David M. Cornet, B.Sc. Engineering Physics (Queen's University)

SUPERVISOR: Dr. R.R. LaPierre

NUMBER OF PAGES: xii, 130

Abstract

InGaAs/InP heterostructure nanowires (NWs) grown by gas source molecular beam epitaxy (GS-MBE) have been analyzed by scanning electron microscopy (SEM), transmission electron microscopy (TEM), and energy dispersive x-ray spectroscopy (EDS). The morphology and interfacial properties of these structures have been compared to pure InP NWs and lattice-matched InGaAs/InP superlattice (SL) structures, respectively. Based on high-resolution x-ray diffraction (HRXRD) and photoluminescence (PL) measurements of the SLs a detailed structural model is proposed, consisting of strained InAsP and InGaAsP monolayers due to group-V gas switching and atomic exchange at the SL interfaces. The interfaces of the heterostructure NWs were an order of magnitude larger than those of the SLs and showed a distinct bulging morphology. Both of these characteristics are explained based on the slow purging of group-III material from the Au catalyst. Growth of InGaAs on the sidewalls of the InP base of these wires was also observed, and occurs due to the shorter diffusion length of Ga adatoms as compared to In.

Acknowledgements

I would like to thank my supervisor Dr. Ray LaPierre, whose guidance, technical insight, and commitment to finding time for meetings made the writing of this thesis an informative and productive experience. For their valuable advice and training I would like to acknowledge the staff of the Centre for Emerging Device Technologies and the Brockhouse Institute for Materials Research, particularly Brad Robinson for the GS-MBE growths, and Fred Pearson for his help with the EDS measurements and TEM images. I would also like to thank my fellow graduate students Hanna Budz and Martin Plante for sharing their knowledge and valued friendship. Finally, I would like to thank my family for their patience and support.

Table of Contents

List of Figures

List of Tables

1 Introduction

1.1 Semiconductor Nanowires: Motivation and Applications

As electronic devices continue to become smaller the practical shortcomings of photolithography techniques become more prevalent and the solutions become more costly. These issues include mask fabrication and resolution limitations such as diffraction, reduced depth of field, and even the finite size of photoresist molecules, causing undesirable variations in the gate length from device to device [1.1, 2]. In recent years there has been a tremendous interest in the fabrication of semiconductor nanowires (NWs) for electronic, biomedical, and photonic device applications. NWs are effectively one-dimensional structures, with diameters as small as 10 nm and lengths of several microns. NW-based electronics could be a viable solution to the limitations of conventional "top-down" microelectronic fabrication and many steps have already been taken to create useful NW devices, including resonant tunneling diodes [1.3], p-n junctions [1.4], superlattices [1.5], and single-electron transistors [1.6]. Also, NWs have been assembled into arrays of diodes, bipolar junction transistors, and logic gates that have been used to implement basic computation [1.7-11]. Recently, silicon NW field effect transistors (FETs) capable of detecting DNA and single virus particles have been demonstrated [1.12, 13], and photonic nanosystems consisting of integrated NW lasers, light-emitting diodes, waveguides, modulators, and photodetectors have been fabricated [1.14-19].

A useful feature of nanowire technology is the ability of these structures to accommodate significant lattice-mismatch. Due to the small cross-section of NWs, highly mismatched heterostructures are possible without the generation of dislocations, including InP/Ge [1.20], InP/Si [1.21], GaAs/Si [1.22], InAs/GaAs [1.23], and InP/GaP [1.24]. Thus, III-V heterostructures and superlattices not attainable in thin films may be produced in NWs, allowing for almost unlimited heterostructural design and bandgap engineering [1.25].

NW devices to date have been mostly limited to simple material systems such as Si, or binary III-V semiconductors such as GaAs and InP. However, functional NW devices will only be fully realized by their extension into more complex material systems that include multiple group-III (e.g., Al, In, Ga) and/or group-V elements (P, As, Sb). Few studies exist for NWs in ternary compound material systems that are of interest in long wavelength optoelectronic devices, such as InGaAs [1.26, 27]. This thesis considers the growth and compositional analysis of InGaAs/InP heterostructure NWs.

1.2 The Growth of Semiconductor Nanowires by VLS

The most dominant method for growing semiconductor NWs is the vapour-liquid-solid (VLS) technique. In the VLS growth process, source material is deposited on a substrate that is seeded with small metal (usually Au) particles. Preferential nucleation of the source material occurs at the seed particles, resulting in growth of one-dimensional semiconductor whiskers or wires. Wagner and coworkers [1.28] first proposed this mechanism in the 1960s to explain the growth of Si whiskers. In the early 1990s, Hiruma and coworkers were among the first to systematically investigate the VLS approach for the fabrication of GaAs NWs, demonstrating quantum size effects and electroluminescence [1.29]. Since then, VLS has been used as a general synthesis route for InP, GaP, and InAs NWs among other material systems [1.30].

In VLS growth, the adsorbed atoms (adatoms) arrive at the NW growth surface by one of three pathways: (i) direct impingement of adatoms on the Au catalyst particle followed by bulk diffusion of adatoms through the particle and incorporation at the growth surface, (ii) direct impingement of adatoms on the Au particle followed by diffusion of adatoms along the particle surface to the growth surface, and (iii) diffusion of adatoms along the sample surface and along the wire sidewalls to the growth surface [1.31, 32]. Of these three methods the diffusion of adatoms along the sample surface is dominant in MBE growth of NWs [1.33-35].

Metal-organic vapor phase epitaxy (MOVPE) is often the method of choice in the growth of semiconductor NWs [1.24, 29, 36-39]. In this case the Au acts as a site for the decomposition of gaseous precursors [1.40], whereas in the case of MBE the constituent elements arrive at the substrate decomposed [1.41]. Thus, VLS growth by MBE includes substantial growth on the non-activated surface (the surface not covered by Au) [1.34]. This often results in the partial burial of MBE NWs. However, a key advantage of MBE is the ability to grow NWs with a large height/diameter ratio at small diameters. This property stems from the very high diffusion length of adatoms on the surface [1.33, 35]. Thus, nanowire growth by MBE offers the ability to grow whiskers much higher than the effective thickness of deposited material because the growth rate is not restricted by the deposition rate, as is the case in chemical vapor deposition methods [1.33].

1.3 A Study of Heterostructure Nanowires

The first samples grown and analyzed in this study were simple planar superlattice (SL) structures consisting of alternating layers of lattice-matched $In_{0.532}Ga_{0.468}As$ and InP grown by GS-MBE on InP substrates. These InGaAs/InP SLs provided a simple starting point in the analysis of material interfaces in InGaAs/InP heterostructure nanowires undertaken in Chapter 5. The SLs demonstrate the capabilities of the GS-MBE process in the growth of simple planar layers in the absence of the growth catalyst used in NW growth. As will be demonstrated, there are many differences between NW and SL growth, but there are some effects present in the growth of SLs that can help in the explanation of the interfacial properties in NWs. The SL structures analyzed in this thesis were labeled with growth numbers 4297, 4298, 4394, 4395, 4396, 144, 145, and 146, and are described in detail in Chapter 3, which is a more detailed description of an article published previously in the Journal of Applied Physics [1.42].

Another valuable reference point was obtained in the growth of InP NWs on *n*-type (111)B InP substrate material (growth #219). Analysis of these wires permitted a more thorough understanding of the growth of InP wires by GS-MBE and could be compared to previous studies of GaAs NWs produced by the same method [1.32] to aid comprehension of the results of the InGaAs/InP NW growth. Much of this analysis (Chapter 4 of this thesis) has been published previously in Applied Physics Letters [1.43], and the analysis of the InGaAs/InP heterostructure NWs (Chapter 5) has recently been submitted for publication in Nanotechnology.

2 Experimental Methods

2.1 Molecular Beam Epitaxy

Molecular beam epitaxy (MBE) is a method by which high-quality single-crystal semiconductor thin films can be deposited on a substrate. The flux of the source material on the substrate is so small, and the pressure in the growth chamber so low ($\sim 10^{-9}$ Torr), that the particles do not interact as they travel from the source to the substrate. In other words, the mean free path of the particles in the source material flux is longer than the distance traveled to the target, resulting in a molecular beam.

MBE growth occurs under conditions far away from thermodynamic equilibrium and is governed by the interaction between the atoms of the surface and the impinging adatoms. This is different than the case, for example, of chemical vapor or liquid phase epitaxy where the growth takes place near thermodynamic equilibrium as the vapor or liquid crystallizes on the substrate surface. This characteristic of the MBE technique ensures abrupt compositional and doping transitions [2.1]. Also, growth rates during molecular beam epitaxy are typically on the order of 1 μm per hour. This slow growth rate allows for very precise control over changes to the material composition in the growth direction, making it possible to obtain the very abrupt material transitions desirable for a number of semiconductor applications. Another advantage of this slow growth rate is the ability of the adatoms to migrate on the surface, ensuring smooth films [2.1].

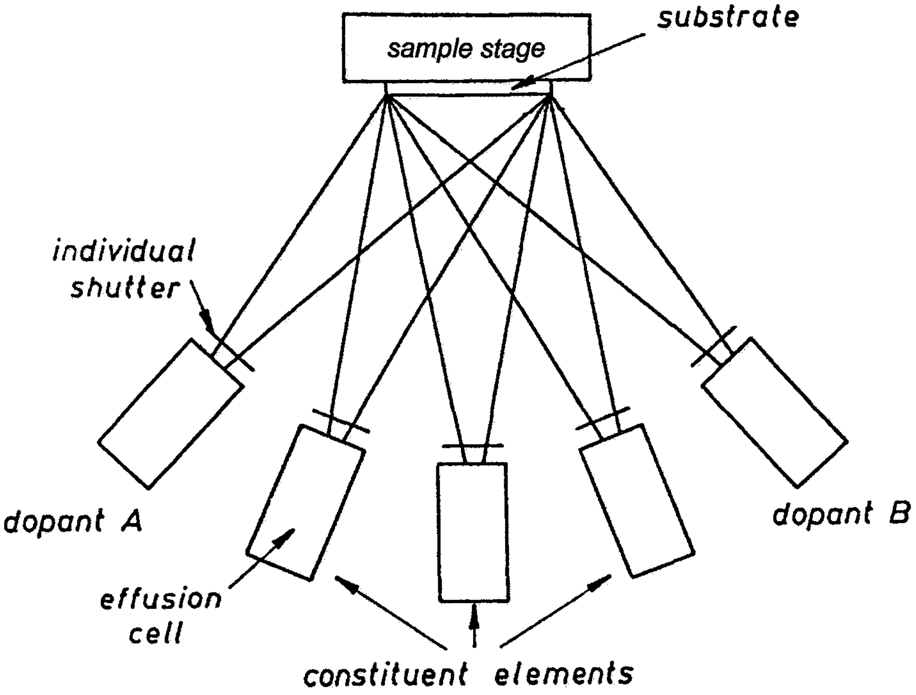

Figure 2.1. Basic MBE growth chamber schematic. Adapted from Herman and Sitter [2.1].

A basic schematic of an MBE system is shown in Figure 2.1. The substrate is fixed to a rotating sample stage that can be heated to the desired growth temperature. Since the sources are slightly off centre, the rotation of the stage helps to create a uniform film. The molecular beam is usually produced by heating elemental material in effusion cells contained within the growth chamber, in which an ultra high vacuum (UHV) environment is maintained (10^{-9} Torr). The temperature-induced elevation in the vapor pressure of the material allows atoms to escape from the surface and impinge on the substrate. Source material can also be supplied by gas sources, such as AsH_3 and PH_3, which are then thermally cracked to produce a flux of dimers and monomers. The use of gas sources results in a high number of these dimers and monomers, which can be incorporated into the growth much more easily than the tetramers typical in solid group V sources [2.2]. Also, due to the storage of gaseous material in tanks outside the growth chamber, gas sources also offer a nearly infinite supply of material, with no need to break the vacuum when replenishing the source. The use of gas sources is referred to as gas source molecular beam epitaxy (GS-MBE) and is the arrangement used to produce all the growths studied in this thesis.

2.2 High-Resolution X-Ray Diffraction Instrument and Measurement Theory

High-resolution x-ray diffraction (HRXRD) is a well-known method of characterizing crystal structures, and is particularly useful in the study of epitaxial semiconductor layers. X-ray sources with wavelengths on the order of a few Ångstroms are readily available, making it possible to probe the individual atomic plane spacings of a semiconductor crystal. The biaxial strain between layers of different materials causes a contraction or dilation of the crystal lattice in the growth direction, altering the lattice spacing between atomic planes. With knowledge of the constituent materials in the layer, measurements of these altered spacings allows for quantification of the material composition. In the measurements performed for this thesis, strain at the superlattice interfaces allowed for the development of an interfacial composition model in the InGaAs/InP material system.

A typical x-ray diffraction setup is illustrated in Figure 2.2. A sample is mounted on a movable stage and irradiated with a collimated and nearly monochromatic beam of x-rays. The x-rays enter the sample and interact with the crystal lattice, which acts like a diffraction grating. A movable detector then records the diffraction pattern formed by the emerging x-rays. Single-layer growths can often be analyzed by leaving the detector stationary and rocking the sample stage through a small angle. Hence, the diffraction patterns produced by XRD are often referred to as "rocking curves".

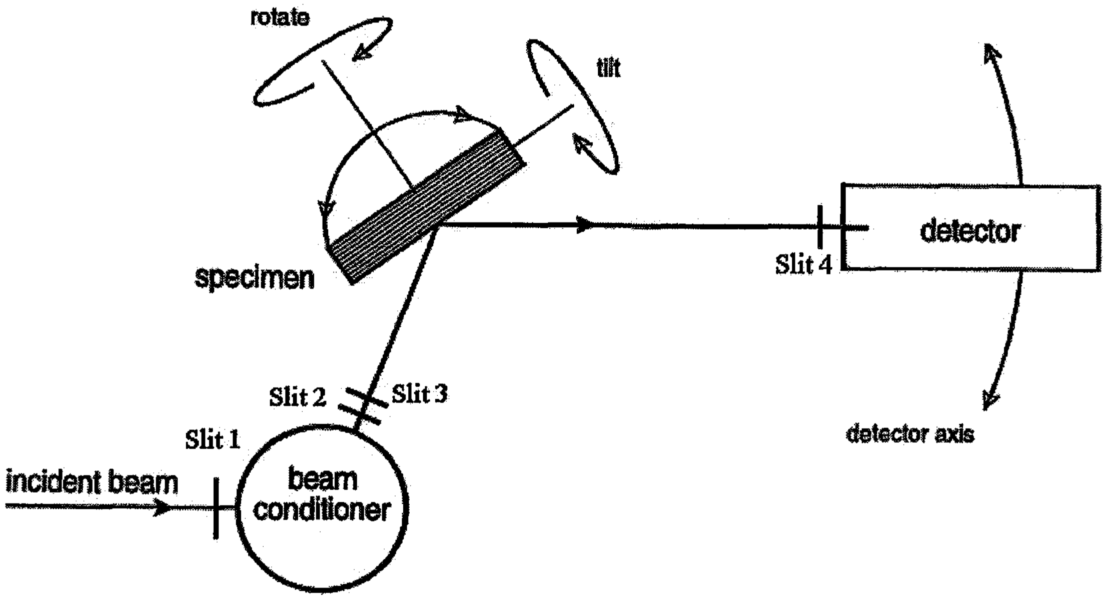

Figure 2.2. Basic x-ray diffraction arrangement, adapted from Bowen and Tanner [2.3].

Through use of the Bragg law one can determine the lattice constant of the crystal under investigation [2.4].

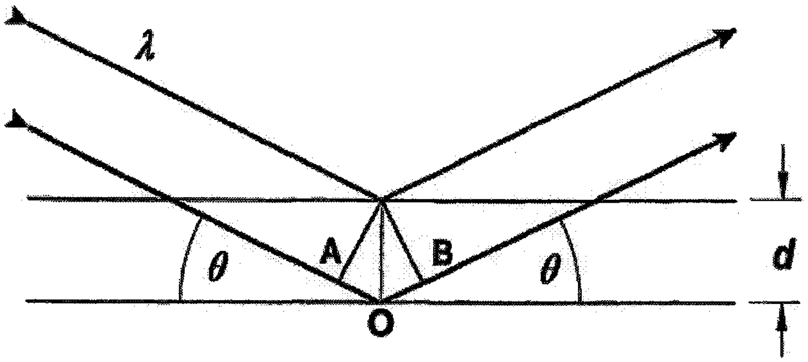

Figure 2.3. Bragg diffraction from the crystal planes of a semiconductor [2.4].

$$n\lambda = 2d\sin\theta \tag{2.1}$$

In Equation 2.1, n represents the diffraction order, λ is the x-ray wavelength, d is the distance between the diffracting planes, and θ is the Bragg angle. Thus, diffraction of the x-ray beam from a given set of crystal planes will create a signal, measurable by a detector. To probe the spacing between individual atomic layers in III-V semiconductor crystals it is necessary to perform the XRD measurement at the Bragg angle corresponding to $n = 4$. This necessity arises due to the fact that d in Equation 2.1 is typically defined as the lattice constant a. In the zincblende lattice there are 4 atomic layers in each unit cell. Choosing $n = 4$ ensures that the {004} family of planes will be probed and information on individual atomic plane spacing will be collected.

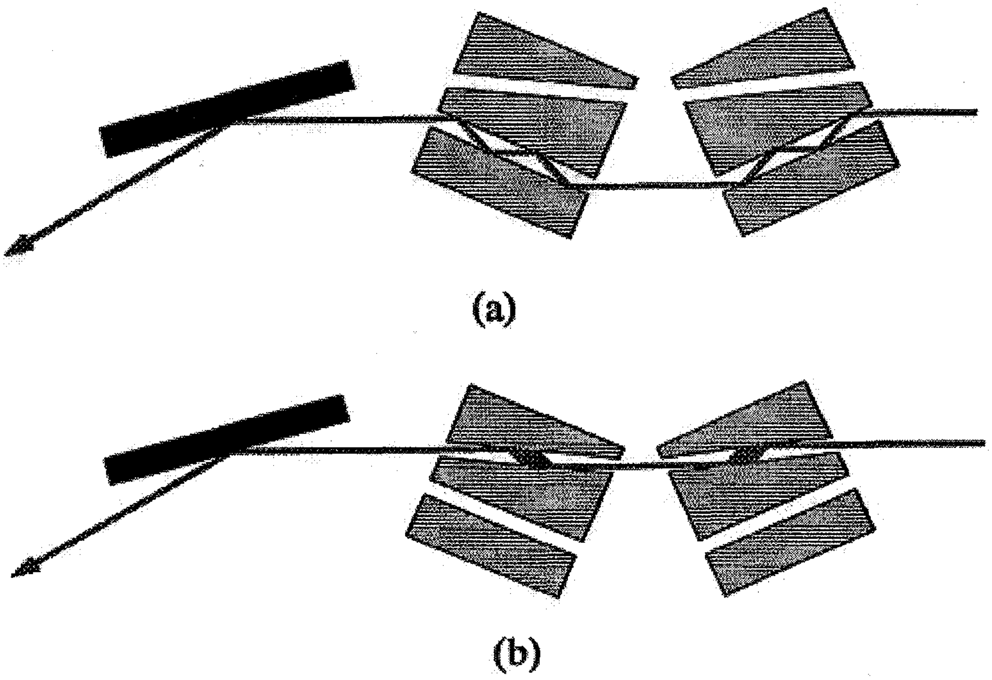

Figure 2.4. Channel cut crystal (CCC) beam conditioners used in XRD experiments [2.3]**. This particular conditioner can be used in two different arrangements: (a) high resolution, and (b) high intensity.**

To achieve the highest accuracy in the measurement of the lattice spacing from Equation 2.1 it is important to ensure that the incident x-ray beam is well collimated and nearly monochromatic. Due to the finite spectral width and beam divergence present in x-ray beams from common sources it is necessary to make use of beam conditioners to achieve the desired characteristics, as illustrated in Figure 2.4. In a channel cut crystal (CCC) beam conditioner the beam from the x-ray source is channeled through a series of reference crystal reflections. These consecutive reflections reduce the beam divergence and eliminate unwanted wavelengths. This results in a beam that is nearly monochromatic and very well collimated, allowing high-resolution measurements of the distances between crystal planes [2.3]. In the experiments performed for this study the beam conditioner was arranged as illustrated in Figure 2.4a to achieve the highest resolution.

In the characterization of an epitaxial layer on a reference substrate the splitting of the layer peak from the substrate peak can be used to quantify the difference in strain between the two materials. For example, consider a layer of InGaAs grown on an InP substrate with a nominal composition chosen to match the lattice of the substrate. From Equation 2.1, splitting of the layer peak from the substrate peak toward lower angles indicates compressive strain due to excess indium in the layer. Conversely, splitting to higher angles indicates tensile strain and a deficiency of indium in the layer. This relationship is demonstrated visually in Figure 2.5.

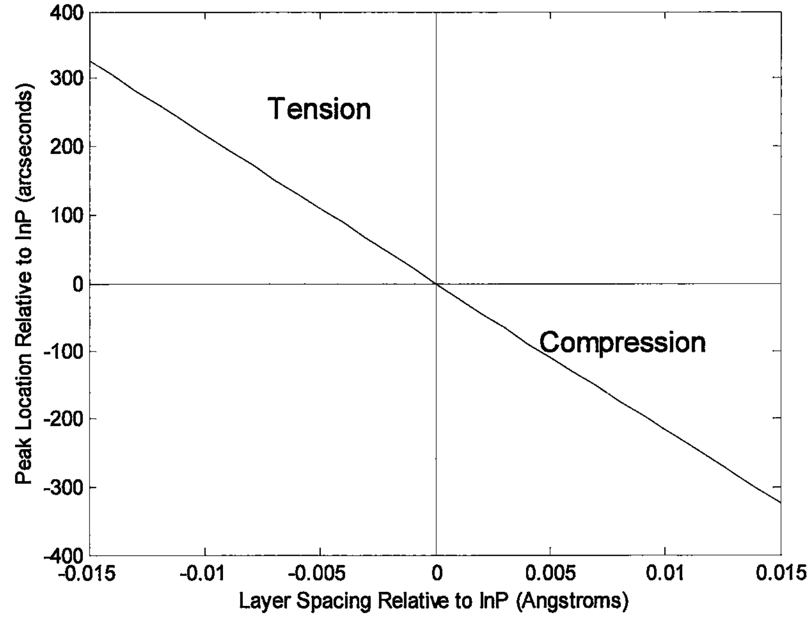

Figure 2.5. Epitaxial layer peak splitting relative to an InP substrate peak as a function of the epitaxial layer lattice constant. Compressive strain occurs in the lower right quadrant and tensile strain occurs in the upper left quadrant. $\theta = 28°$, $\Lambda = 1.541$ Å.

Equation 2.1 can be manipulated into a form more useful in quantifying mismatch between epitaxial layers and substrates. Taking the derivative with respect to the Bragg angle gives:

$$\frac{\delta d}{d} = -\delta\theta \cot\theta \tag{2.2}$$

where δd is the difference between the lattice constant of the epitaxial layer and the substrate in the growth direction. For use in the characterization of material strain this equation must be modified to account for Poisson ratio effects. As shown in Figure 2.6, the strain between the unrelaxed layer and substrate will exaggerate the difference between the two lattice constants. This exaggerated lattice constant is the value collected from the HRXRD measurement, and must therefore be corrected through use of the following expression:

$$m = m^*\left(\frac{1-\upsilon}{1+\upsilon}\right) \tag{2.3}$$

where m^* is the effective lattice mismatch, represented by the left hand side of Equation 2.2, and m is the actual lattice mismatch between the two relaxed materials [2.5]. Equation 2.2 and Equation 2.3 can be combined to form a corrected differential Bragg equation:

$$m = -\left(\frac{1-\upsilon}{1+\upsilon}\right)\delta\theta \cot\theta \tag{2.4}$$

Figure 2.5 does not account for the Poisson ratio effect included in Equation 2.4. Accounting for this additional effect, a plot of peak splitting as a function of lattice mismatch can be produced as in Figure 2.7.

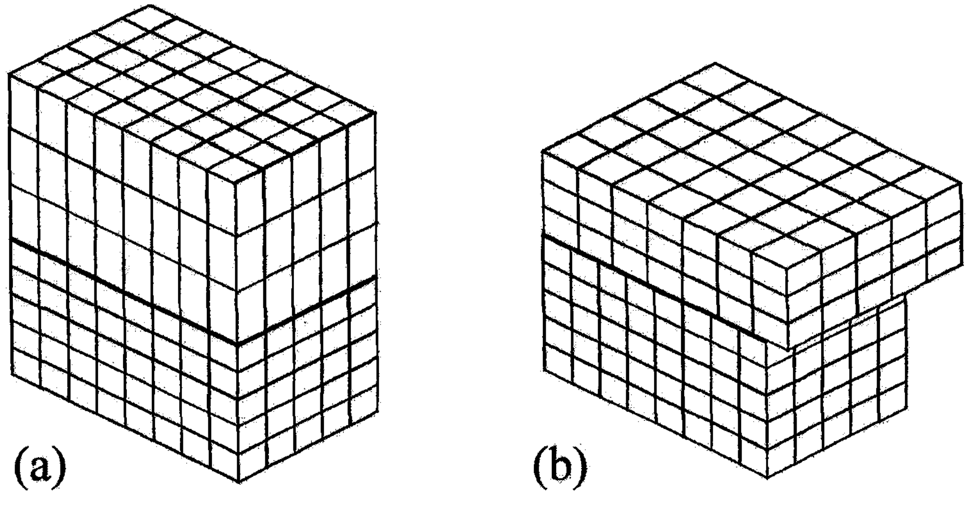

Figure 2.6. Tetragonal distortion of a mismatched epitaxial layer. (a) Strained layer conforms to the lattice of the substrate; (b) Layer is fully relaxed. Adapted from Bowen and Tanner [2.5].

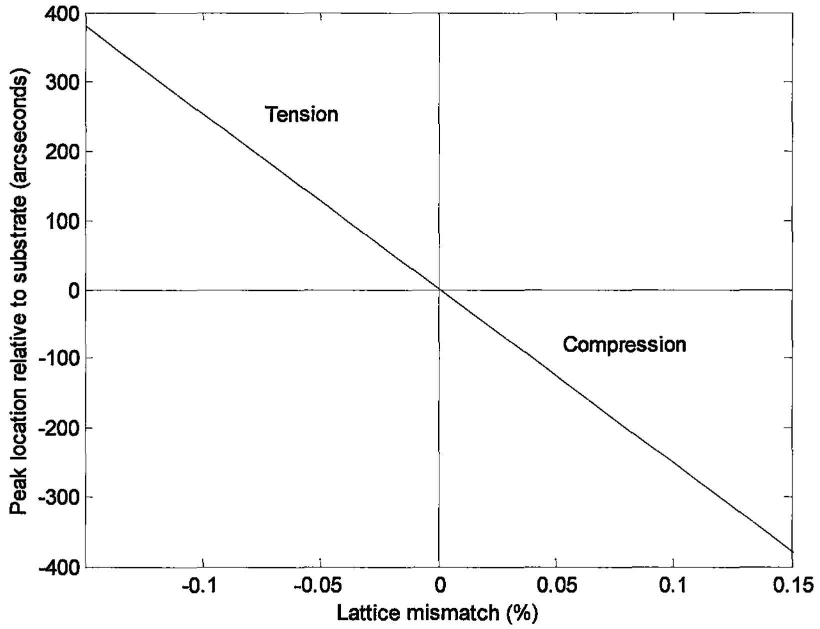

Figure 2.7. XRD peak splitting as a function of lattice mismatch for InGaAs on InP.

In the study of superlattices (SLs), analysis of the rocking curves becomes more complex. Instead of the single peak corresponding to the film there are a number of satellite peaks. The satellite peaks are spaced symmetrically about a central superlattice peak, which represents the average strain in the entire structure relative to the substrate. The angular separation between the satellite peaks is given by:

$$2\Lambda(\sin\theta_n - \sin\theta_0) = \pm n\lambda \qquad (2.5)$$

where Λ is the period of the SL (equal to the combined thickness of one InP and one InGaAs layer), θ_n is the diffraction angle for the satellite peak of order n, θ_o is the angle for the zero-order ($n = 0$) satellite peak, and λ is the Cu Kα_1 x-ray wavelength of 1.541 Å [2.6]. Note that the definition of n in Equation 2.5 is different than that of Equation 2.1, in that n now refers to the satellite peak order.

The inability to effectively measure x-ray phase information makes it impossible to reconstruct the lattice from measured x-ray rocking curves [2.7]. Instead, specialized software can be used to create simulated curves based on variable input parameters. These simulated curves can be compared to the experimental curves and fine-tuned by adjustment of the input parameters to find the best-fit to the data.

2.3 HRXRD Experimental Details

Rocking curves of the (004) reflection were produced using the Bede D1 system with the channel cut crystal (CCC) beam conditioner in the four-bounce arrangement (Figure 2.4a) to optimize scanning resolution. A sample of the InGaAs/InP SL was placed on the sample stage and fixed in place with small metal clips and blocks. The stage was then fastened to the sample stage mechanism with a setscrew. The system was run through a calibration routine to optimize the signal strength at the detector by finding an ideal translational location for the sample stage. After achieving an acceptable stage location, the detector and sample angles were moved to the appropriate positions to collect data from the (004) Bragg peak of the substrate (InP). With the detector slit removed, manual adjustments were made to the detector angle θ, the sample rocking angle ω, the sample tilt angle χ, and the sample rotation angle φ, to optimize the signal strength. The detector slit was then replaced and the manual optimization was repeated.

Beam and detector slits were chosen to maximize the number of x-rays incident upon the sample and to ensure minimal background signal at the detector. Four different slits were used to manipulate the x-ray beam: the *initial beam definition slit*, located between the x-ray source and the first CCC; the *primary beam definition slit*, located after the second CCC; the *secondary beam definition slit*, located immediately after the *primary beam definition slit*; and the *detector slit* at the detector opening. These 4 slits are illustrated in Figure 2.2 and labeled 1-4 in the order listed below. Shapes and size choices for these slits were as follows:

- Initial beam definition slit: 5 or 10 mm diameter circle (depending on size of sample)
- Primary beam definition slit: 5 or 10 mm diameter circle (depending on size of sample)
- Secondary beam definition slit: 0.5 mm vertical slit
- Detector slit: 0.5 mm vertical slit

To include the satellite peaks of the superlattices it was necessary to scan over much larger angles than is required in the case of a single epitaxial layer. For this reason, scans were performed in the ω-2θ mode, meaning that the detector angle (θ) changed at twice the rate of the sample angle (ω) to stay in line with the diffracted beam from the sample. Measurement step sizes were chosen around 10 seconds of arc and measurement times ranged from 10 to 35 seconds depending on the angular breadth of the diffraction pattern. Scanning in this fashion, individual scans took ~10 – 18 hours to complete.

2.4 Photoluminescence Instrument and Measurement Theory

Luminescence in semiconductor materials occurs as electron-hole pairs recombine, causing the emission of a photon. The emission of photons by this process creates a spectrum that can be collected and analyzed to characterize the excited material. The electron-hole pairs can be created through a number of excitations, including inelastic collisions with high-energy electrons (cathodoluminescence), application of a strong electric field (electroluminescence), or the absorption of photons (photoluminescence). Photoluminescence spectroscopy (PL) is a simple, non-destructive technique, in which the electron-hole pairs are produced through the absorption of laser light and the luminescence spectrum is analyzed to characterize the irradiated sample.

PL measurements are often used in the characterization of semiconductors. The emitted photon has energy equal to the difference between the energy levels of the electron and hole. Thus, luminescence occurring due to recombination of electrons from the bottom of the conduction band and holes from the top of the valence band can be measured to determine the material bandgap. In addition to direct band-to-band transitions, luminescence spectroscopy can provide information about impurities (ie. donor and acceptor levels) and energy shifts due to temperature changes and quantum confinement. Analyzing the combined effect of these variables can provide insight into the structural and compositional characteristics of a specimen.

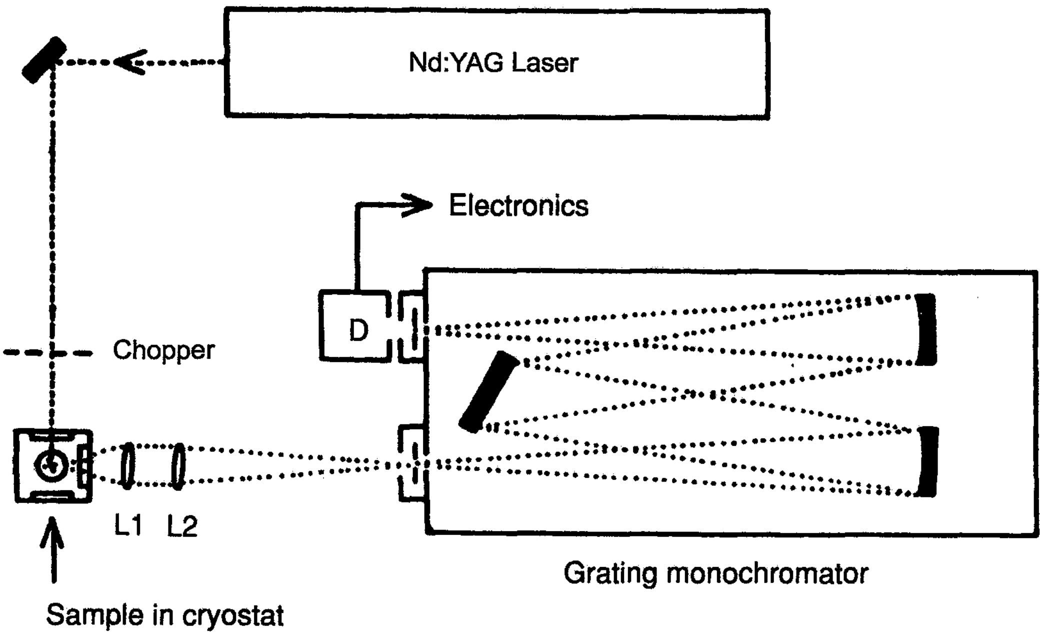

Figure 2.8. Basic PL system schematic. The sample is excited with the Nd:YAG laser and the luminescence is collected by lenses L1 and L2. The monochromator permits analysis of specific wavelengths at the detector (D). Adapted from Perkowitz [2.8].

A schematic of the PL setup is shown in Figure 2.8. The cryostat is used to cool the sample to increase resolution by reducing thermal broadening, which is roughly equal to k_bT, where k_b is the Boltzmann constant and T is the sample temperature. Cooling also helps to reduce the probability of non-radiative recombination, increasing the efficiency of the luminescence, and prevents the ionization of impurities [2.8]. The sample is excited by a Nd:YAG laser which produces light of wavelength 532 nm to excite the InGaAs/InP SL structures ($E_g \approx 1500$ nm). The luminescence from the sample is then collected by a pair of lenses and focused into the opening of a monochromator. The monochromator is used to select a narrow band of wavelengths to send to the detector (marked D in the figure), which detects the intensity of the luminescence. The monochromator scans through a range of wavelengths and the computer records the intensity profile.

2.5 PL Experimental Details

Small samples of each of the SLs were cleaved and arranged on a rectangular piece of copper ~12 mm x 30 mm and ~1 mm thick. The samples were fixed in place with a small amount of vacuum grease in an arrangement as shown in Figure 2.9. The Cu base-plate was then fixed to the sample stage in the cryo-head of the PL system with heat-sink paste. The purpose of fixing the samples to the Cu plate was to facilitate the ease of placement in, and removal of the samples from, the system with minimal contamination of the sample surfaces during handling.

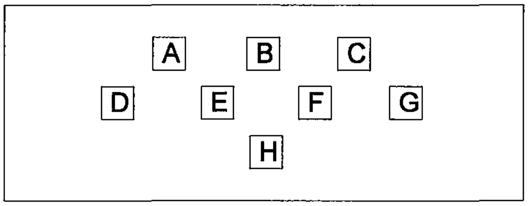

Figure 2.9. SL sample arrangement on Cu base. Sample numbers are: (A) 4297 (B) 4298 (C) 4394 (D) 4395 (E) 4396 (F) 144 (G) 145 (H) 146.

With the samples fixed to the sample stage of the cryo-head, the cover was attached and the system evacuated with a roughing pump while being heated with the stage heater and an external heating tape to expedite the degas process. After the system reached ~10 mTorr the cryo-pump was turned on to cool the samples. This process took ~4 hrs.

Having achieved the lowest possible temperature (~23 K), the Nd:YAG laser and the electronics were turned on. The laser, operating at a wavelength of 532 nm, was focused on the Cu base between samples to get a rough alignment of the optics using the scattered laser light. The laser was then focused on sample A of Figure 2.9 and the monochromator was scanned through wavelengths around the expected peak energy. After finding the main PL emission peak with the monochromator, the signal intensity was optimized by adjustments to the optical alignment and the phase of the lock-in amplifier, with the detector slits open to 500 μm. A reference reading from the detector was taken to facilitate normalization of the curve during analysis, and the system was then set to scan over a range encompassing the details of the peak in 1 nm steps using the *plscan.bas* computer program.

After completion of the scan, the temperature was increased by use of the stage heater, another reference intensity reading was taken, and another scan was collected. This process was repeated for 12 temperatures: 23, 27, 30, 35, 40, 50, 60, 80, 100, 150, 200, and 300 K, with the optical alignment left undisturbed. The cryo-head was re-cooled and the laser was then focused on the next sample and the whole alignment and scanning process was repeated for each sample

2.6 Scanning Electron Microscopy Instrument and Measurement Theory

Imaging with electrons is a very powerful tool in the characterization of semiconductor crystal structures. The advantage of this technique lies in the electron de Broglie wavelength λ, defined by

$$\lambda = h / p \tag{2.6}$$

where h is Planck's constant and p is the particle momentum. Neglecting relativistic effects, the kinetic energy of an electron accelerated through a potential difference V can be written

$$\frac{1}{2} m v^2 = eV \tag{2.7}$$

where m, v, and e are the electron mass, speed, and charge, respectively. Equations 2.6 and 2.7 can be combined to describe the electron wavelength as a function of the accelerating voltage V:

$$\lambda = \frac{h}{\sqrt{2meV}} \tag{2.8}$$

Thus, electrons accelerated through a potential difference of tens of volts can quickly achieve a wavelength on the order of Cu Kα_1 x-ray radiation (1.541 Å). And, when accelerated through 100 kV, wavelengths on the order of a few picometres are possible. The ability to probe materials with such small wavelengths creates the potential for extreme resolving power.

Unlike x-rays, the charge of electrons permits focusing of the beam via magnetic lenses, preserving the phase information that would be lost in HRXRD experiments [2.7].

The charged nature of electrons also causes significant interaction with the sample material. Therefore, electrons are best suited to probing samples thinner than ~1 μm, whereas the penetrating power of x-rays makes them useful in the analysis of thicker samples [2.4]. This short penetration depth makes the electron probe a valuable tool in the characterization of topographical features, and is exploited in the scanning electron microscope (SEM).

As electrons from the energetic electron beam (~20 keV) enter the sample, they participate in elastic and inelastic scattering events. Inelastic scattering events produce secondary electrons, x-ray photons, cathodoluminescence, and Auger electrons, while elastic scattering events produce backscattered electrons. These events limit the penetration depth of the beam and form an interaction region as illustrated in Figure 2.10, which shows the classical teardrop shaped region of x-ray production (region 1), the depth from which backscattered electrons can escape (region 2), the thin film from which secondary and Auger electrons can escape (thin hatched region), and the entire interaction volume (region 3).

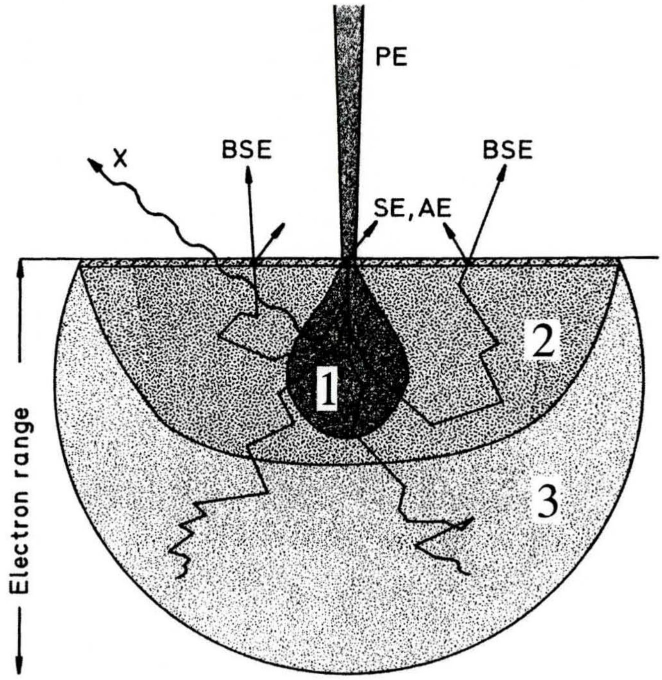

Figure 2.10. Interaction volume of the SEM electron beam. Primary electrons (PE), x-ray photons (X), backscattered electrons (BSE), secondary electrons (SE), and Auger electrons (AE) are identified. Four regions of interest are also identified: (1) teardrop shaped region of x-ray production, (2) escape depth of backscattered electrons, (3) entire volume of interaction, (thin hatched region) escape depth of Auger and secondary electrons. Adapted from Reimer [2.9].

The SEM images produced for this thesis report were created from the collection of either secondary electrons or backscattered electrons. Auger electrons and cathodoluminescence are mentioned above for completeness, while x-rays will be discussed in Section 2.8.2 with regard to EDS measurements.

Secondary electrons are created through inelastic collisions between the incident electrons and atomic electrons in the sample. The incident electrons are energetic enough to impart some of their kinetic energy to atomic electrons in the sample, permitting them to move within the material until they either escape from the surface into the vacuum, or are brought to a halt by inelastic collisions with other atomic electrons in the specimen. These secondary electrons have much less kinetic energy than incident electrons (<100 eV), and so are only able to escape from a small depth (~2 nm) below the surface. This shallow escape depth makes secondary electrons very useful in the characterization of topographical features [2.10].

Images constructed from the collection of backscattered electrons are also useful. Backscattered electrons have a much higher energy than secondary electrons, and are produced through elastic scattering from the positively charged nuclei in the lattice. The large mass of the nuclei compared to the incident electrons causes a negligible loss in electron kinetic energy after the collision. Thus, these collisions simply redirect the incident electrons. This higher energy allows for a longer escape depth and makes backscattered electrons less capable of resolving fine topographical details than secondaries. However, the scattering probability of backscattered electrons increases with increasing atomic number (Z), making backscattered electron imaging useful in creating contrast between materials of different atomic number (high z-contrast) [2.11].

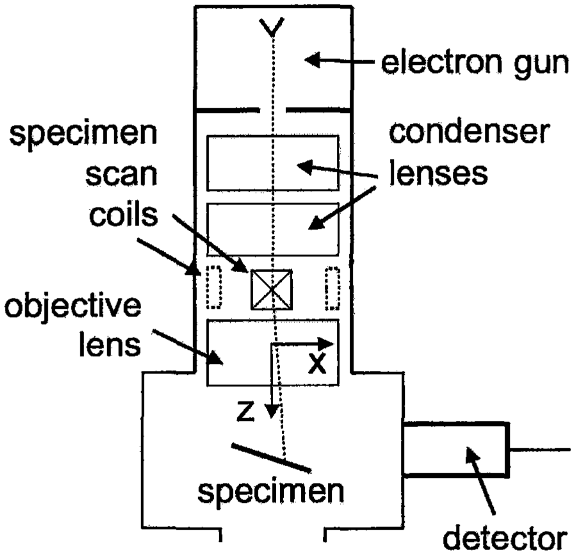

Figure 2.11. Basic SEM instrument schematic. Adapted from Egerton [2.12].

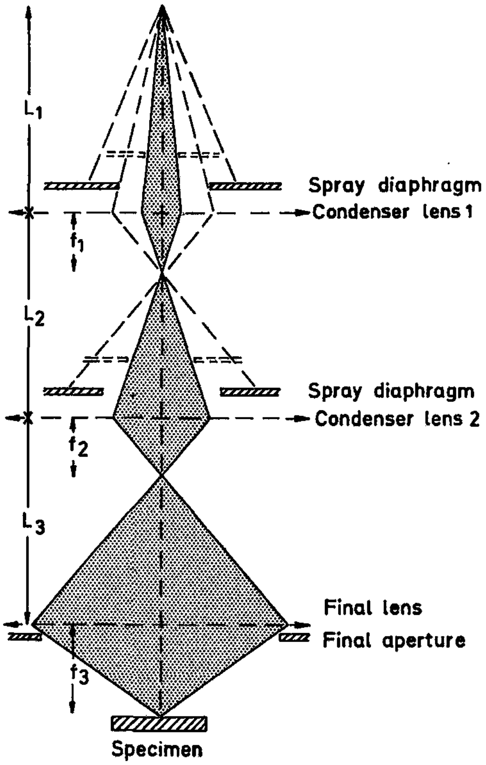

Figure 2.12. SEM electron beam diagram showing the lens focal lengths (f) and the lens spacings (L). Adapted from Reimer [2.13].

The basic SEM set-up is shown in Figure 2.11. Incident electrons are produced in an electron gun and focused by a set of magnetic condenser lenses. The beam is focused to a fine point on the sample surface by a final lens called the objective lens [2.12]. A more detailed diagram of the electron lens system is shown in Figure 2.12, which shows the effects of the lenses and apertures on the beam. The beam interacts with the sample, ejecting secondary and backscattered electrons. These escaping electrons are then collected by a detector, positioned to collect either secondary or backscattered electrons. The beam is then scanned across a small rectangular area of the sample surface, while the detector records the number of electrons captured at each point on the surface. Contrast is created from changes in the number of electrons ejected from the surface (electron yield) as the beam is scanned from point to point on the sample surface. This information is sent to a computer to construct an image of the surface.

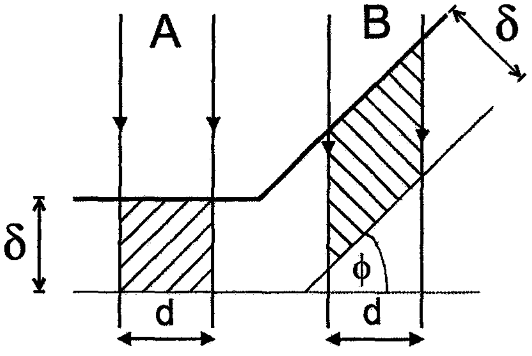

Figure 2.13. The relationship between topographical features and secondary electron yield. Adapted from Egerton [2.10].

Changes in secondary electron yield are due to topographical variations as illustrated in Figure 2.13. An incident electron beam of diameter *d* will produce a minimum secondary electron yield when incident on a surface that is normal to the beam (region A in Figure 2.13). When incident on an angled surface, secondary electrons are generated in a larger volume within the escape depth δ (region B in Figure 2.13).

To image in secondary electron mode, a scintillator-photomultiplier combination detector, set to the side of the sample chamber (Figure 2.11), collects the escaping electrons as the beam scans the surface, creating contrast according to the number of electrons collected at each point. This detector is called the Everhart-Thornley detector. The detector is biased (~100 V) to exploit the low kinetic energy of secondary electrons and direct them into the detector opening. This bias is too low to redirect the backscattered electrons, making this technique well-suited to secondary electron imaging [2.14]. The electrons are then accelerated through a large potential (~10 kV) to give them sufficient energy to excite the scintillator material. The photomultiplier tube then detects light from the scintillator.

Backscattered electrons are more efficiently collected by a Robinson detector, which is placed directly over the specimen, and is ring-shaped to allow the primary beam to pass through the centre [2.11]. The physics of operation are the same as the Everhart-Thornley detector, except that there is no additional acceleration of the electrons toward the scintillator, making this detector insensitive to secondary electrons.

2.7 SEM Experimental Details

All SEM images produced for this thesis report were made with a JEOL JSM-7000F SEM equipped with a field-emission electron gun. Small samples were cleaved from each NW growth and marked for orientation. Marking was accomplished by scoring each sample with a small chevron pointing in the direction of the major flat ([0-11] direction of a (111)B-oriented wafer). Samples were fixed to steel stubs using silver paint or carbon adhesive tape to ensure a good electrical contact. Stubs were fixed to the sample stage with a setscrew and placed into the load-lock, which was then pumped to a pressure of ~10^{-3} Pa. The stage was then transferred into the main chamber and onto a movable stage via a transfer arm. After reaching a pressure of ~10^{-4} Pa the valve to the field emission electron gun was opened. With the secondary electron detector selected, the stage was raised to the smallest working distance possible with the coarse focus knob and an image was formed at the lowest magnification (30x).

Before increasing the magnification or making fine adjustments to the focus the sample stage was rotated on the axis of the electron probe so that the chevron marking on the sample surface pointed upward in the image, ensuring that the [0-11] direction of the sample aligned with the vertical of the image. This adjustment ensured uniformity in the orientation of the images when characterizing surface feature orientation, as in the case of NW sidewall facets.

Images were focused by use of the stage height adjustment at low magnification and by adjustments to the objective lens at high magnification. For magnification above ~5,000 times it was necessary to make careful adjustments to the beam stigmators to avoid distortions due to astigmatism. The accelerating voltage ranged from 5 to 15 keV and was adjusted to achieve the best balance between resolution and background noise. Focus and astigmatism adjustments were made using a high scan rate to make fine adjustments easy to see. After optimizing the sharpness of the image, the brightness and contrast were adjusted and the scan rate was reduced to achieve the best signal-to-noise ratio. To image using backscattered electrons a Robinson detector was inserted directly above the sample. All images were exported as 8-bit TIFF files, displaying the magnification, detector type, working distance, and accelerating voltage.

2.8 Transmission Electron Microscopy and Energy Dispersive X-Ray Spectroscopy Instrument and Measurement Theory

2.8.1 Transmission Electron Microscopy

Similar to the operating principle of a light microscope, a transmission electron microscope (TEM) can reconstruct an image from electrons transmitted through a thin portion of the sample. To permit the transmission of electrons it is important to have a thin sample (<200 nm) and an energetic electron beam (>100 keV) [2.15]. Thinning of samples often requires a time-consuming mechanical abrasion process followed by precise ion milling. Fortunately, the nanowires analyzed in this thesis were often thinner than 100 nm, making the sample preparation procedure much simpler.

In contrast to the highly focused incident beam used in SEM, the TEM incident beam is slightly defocused at the specimen by the condenser lenses to create a nearly uniform illumination over the area of interest on the specimen. The electron gun and condenser lenses of the TEM, although larger, are arranged in much the same way as in the case of the SEM [2.12]. However, the objective lens is placed behind the specimen and there are a number of additional lenses and apertures required to form an image from the transmitted electrons. A basic schematic of the TEM imaging system is shown in Figure 2.14. As the electrons are transmitted through the specimen they are redirected as they encounter atomic nuclei (elastic scattering) and atomic electrons (inelastic scattering). The dashed line in the figure illustrates the path of a scattered electron. These scattering events, especially elastic scattering events, are the key to the formation of a TEM image. The emerging electrons are then collected by the objective lens, providing the initial magnification of the specimen image. Fine adjustments to the current in the objective lens allow the operator to tune the focus of the image. Since the objective lens provides the first 20-30 times magnification the quality of this lens (low spherical and chromatic aberrations) is critical to the quality of the final image [2.16].

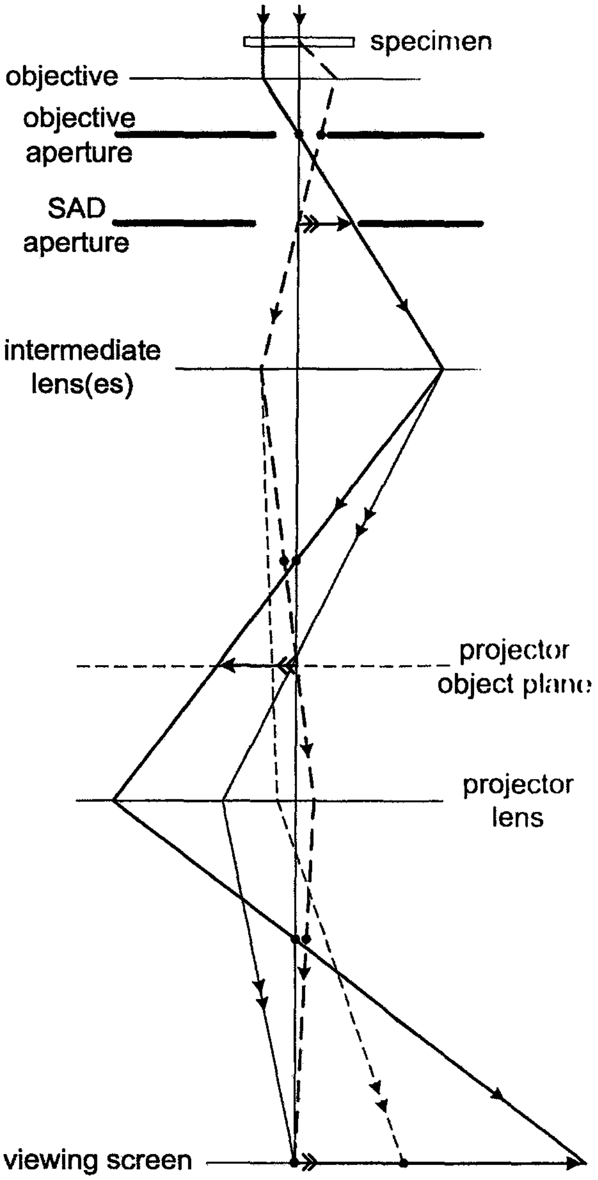

Figure 2.14. Basic schematic of the TEM imaging system. The dotted line follows the path of electrons scattered at a small angle to the incident beam and the solid line follows the path of an electron traveling parallel to the incident beam. The single arrows show the electron path with the intermediate lens set to form an image on the viewing screen; the double arrows show the electron path with the intermediate lens set to form a diffraction pattern on the viewing screen [2.17].

The objective lens is followed by two apertures: the objective aperture, which is located at the back focal plane of the objective lens; and the selected-area diffraction (SAD) aperture, located at the plane of the specimen image created by the objective lens. The objective aperture enhances the contrast of the image by absorbing electrons scattered through large angles, causing regions of high scattering probability to appear darker at the viewing screen [2.18]. As the name suggests, the SAD aperture allows the user to select a small area of the specimen for diffraction, eliminating contributions from the surrounding material. The diameter of this aperture corresponds to a magnified region of the specimen.

The intermediate lens serves two purposes. First, the current in the lens can be adjusted by the user to alter the magnification of the image at the viewing screen. Second, the intermediate lens can be toggled to display either the magnified image or the diffraction pattern of the specimen on the viewing screen. The final image is then expanded to fill the viewing screen by the projector lens.

2.8.2 Energy Dispersive X-Ray Spectroscopy

It has already been demonstrated that an energetic electron beam can eject electrons from the sample (Section 2.6). The energy of the incident electrons is often high enough that K- and L-shell electrons can be liberated from the specimen (Figure 2.10), which is especially true in the TEM due to the high energy (>100 keV) of the electron beam. The emission of x-ray photons can occur as the upper-level electrons loose energy to fill the vacancies. The energies of these x-rays are specific to the atom and energy transition from which they originate [2.19], making it possible to identify the chemical elements illuminated by the beam. Detailed analysis of the x-ray spectrum forms the basis of energy dispersive x-ray spectroscopy (EDS). Through this technique, one can identify different atomic species present in the sample and make local compositional measurements.

To make characteristic x-ray measurements with high spatial resolution it is necessary to adjust the incident beam so that it forms a small point to scan across the specimen, much like the case of the SEM. Use of the TEM in this arrangement is called scanning transmission electron microscopy (STEM). The x-ray spectrum collected at the EDS detector can be directly related to a small region under the electron beam. Since TEM samples are much thinner than those prepared for SEM, and the electron energy is much higher, the interaction volume becomes significantly reduced. This gives x-ray analysis higher resolution capabilities in the TEM than in the SEM.

To extract compositional information from the spectrum, beyond simply identifying which elements are present, it is important to understand the origin of the x-rays. The probability that a K- or L-shell electron will be ejected (the ionization cross-section) and the probability that the ionized atom will emit an x-ray photon instead of an Auger electron (the fluorescence yield) are strongly dependent on the excited element. The ionization cross-section is also dependent on the energy of the electron beam, having an optimum value for ionization of each shell of each element [2.20, 21]. With an understanding of these dependencies, and utilizing specialized computer software [2.22], specific concentrations of different elements in the specimen can be mapped.

2.9 TEM and EDS Experimental Details

After sample preparation the specimen was loaded into the double-tilt TEM stage with vacuum tweezers. The stage was then inserted into a Gatan Model 950 Advanced Plasma System and submitted to a 2 min plasma treatment to remove hydrocarbon contaminants that would otherwise cause blackening of the sample surface under the electron beam. After the plasma cleaning treatment, the tip of the stage was inserted into the microscope column through the load-lock of the JEOL 2010F high-resolution TEM. A beam alignment procedure was then performed to optimize the instrument resolution.

To obtain images capable of resolving individual columns of atoms in the lattice it was necessary to carefully adjust the tilt of the specimen to align these columns with the electron beam (zone axis alignment). This orientation was achieved by carefully tilting the specimen while watching the diffraction pattern. After achieving the zone-axis orientation high-resolution images were recorded using a CCD camera and saved into the Digital Micrograph [2.23] proprietary file format.

The microscope was switched into STEM mode to perform EDS measurements. The image was adjusted in the CRT display to optimize the orientation and magnification for the desired measurement. Points or lines of interest were selected in the INCA EDS software [2.22] and the x-ray detector was opened to begin collection of the spectra. The INCA software was also used in the analysis of the x-ray spectra to gather the element concentrations in samples.

Note: all of the TEM images and EDS spectra were produced with by, or under the supervision of, Fred Pearson.

3 High-Resolution X-Ray Diffraction and Photoluminescence Analysis of $In_{0.53}Ga_{0.47}As/InP$ Superlattices

3.1 Introduction

Superlattices (SLs) consist of multiple layers of materials of various compositions and/or doping. These structures often have a periodic structure that can be analyzed by high-resolution x-ray diffraction (HRXRD) measurements. With the aid of computer simulations these measurements allow for very detailed determination of material composition, and are utilized in the characterization of the interfaces between the SL layers. Photoluminescence (PL) measurements were made at a range of temperatures for each SL to provide some additional support to the HRXRD results. These characteristics were used as a baseline in the explanation of the InGaAs/InP heterostructure NWs analyzed by TEM measurements in Chapter 5.

InGaAs/InP multiple quantum wells and superlattices have numerous optoelectronic applications including semiconductor photodiodes, light sources, and modulators [3.1-6]. InGaAs/InP heterostructures are also a model system for understanding semiconductor growth processes where mixed group-III and group-V interfaces are involved. The growth of nominally lattice-matched InGaAs/InP heterostructures and SLs grown by chemical beam epitaxy (CBE), metalorganic vapor phase epitaxy (MOVPE), or molecular beam epitaxy (MBE) has therefore been investigated by numerous authors [3.7-16] and a number of widely varying growth models have been developed.

During the gas-switching phase of InGaAs/InP heterostructure growth, there is an exchange of group-V atoms across the interface. This exchange results in changes to the structural properties of SLs or multiple quantum well structures. Benzaquen *et al.* [3.7], for example, developed a CBE growth model with three monolayers (MLs) of $InAs_{0.75}P_{0.25}$ at the InGaAs-on-InP interface and 2 MLs of $In_{0.52}Ga_{0.48}As_{0.21}P_{0.79}$ at the InP-on-InGaAs interface. In another CBE study, McKay *et al.* [3.10] arrived at a similar result, with a 5 Å $InAs_{0.65}P_{0.35}$ layer at the InGaAs-on-InP interface and a 5 Å $In_{0.532}Ga_{0.468}As_{0.2}P_{0.8}$ layer at the InP-on-InGaAs interface. Through an XRD study Leys *et al.* [3.17] reported a model consisting of one ML of InAs and one underlying ML of $InAs_{0.8}P_{0.2}$ at the InGaAs-on-InP interface but provide no composition for the other interface, which is noted to be a compressively strained quaternary layer. Finally, a larger interfacial effect has been proposed by Sherwin *et al.* [3.11], which involves an interfacial region of ~5 ML of $In_{0.75}Ga_{0.25}As_{0.5}P_{0.5}$.

InGaAs/InP SLs grown by MOVPE have also been reported with 2-3 MLs of InGaAsP at the InP-on-InGaAs interface and 2-4 ML of InAsP at the InGaAs-on-InP interface due to As/P exchange [3.12, 13] Krost *et al.*[3.9], suggested that only a fraction of a monolayer of InAs is created during the gas switching from PH_3 to AsH_3 after completion of the InP layer and that a fraction of a monolayer of $In_{0.4}Ga_{0.6}As_{0.704}P_{0.296}$ is created at the inverted interface to create the strain balance necessary to fit their XRD rocking curves.

In SLs grown by MBE, Vandenberg *et al.* [3.14] performed an analysis using a kinematical diffraction step model which suggested that interfacial compositional deviations occur over less than one ML. As will be shown, this is not believed to be the case in the structures studied in this article. In another article by the same authors [3.15], the presence of a 9 Å thick layer of $In_{0.53}Ga_{0.47}As_{0.985}P_{0.015}$ at the InP-on-InGaAs interface is reported due to substitution of P for As in the $In_{0.53}Ga_{0.47}As$ layer during growth interruption. This larger interfacial region is reinforced by Shiau *et al.* [3.16] who suggested the presence of 4 ML of compositionally graded InAsP at the InGaAs-on-InP interface.

This chapter describes a comprehensive HRXRD study in which an alternative interface model is proposed for InGaAs/InP SLs prepared by gas source MBE (GS-MBE). This model accounts for grading in the interfacial layers and is shown to be valid over a range of superlattice periods.

3.2 Superlattice Growth Procedure

The samples studied in this work were lattice-matched $In_{0.532}Ga_{0.468}As$/InP SL structures grown by GS-MBE in which the InP barrier and InGaAs well layers were of equal thickness. Samples were grown with nominal SL periods ranging from 36 to 400 Å, corresponding to a range of 12 to 136 monolayers (MLs), with one ML defined as one layer of group-III atoms and one layer of group-V atoms. The structures were all grown with 30 periods of InGaAs/InP with the exception of the 400 Å samples, which were grown with 20 periods. One of the 400 Å samples (sample 4394) was terminated with a 500 Å InP cap layer, grown at low-temperature (300 °C). This cap layer made it possible to perform a detailed annealing study of the interface smearing, not reported in this thesis. Three of the samples (4297, 4298, and 4394) were grown on *n*-type (100) substrates with the remaining five grown on semi-insulating (100) InP substrates to allow for characterization by magnetoresistance measurements (not presented in this thesis). These growths were performed during an equipment upgrade period, in which the GS-MBE system was replaced. Thus, some of the samples were grown in a custom-built MBE system ("old" MBE system) and some were grown in a commercial system designed by SVT Associates, Inc., ("new" MBE system). As will be discussed below, there are some observed differences in the results based on this distinction. Table 3.1 shows the nominal period, substrate doping, and system on which each of the samples was grown.

SL Sample Number	**Nominal Period (Å)**	**InP Substrate Doping**	**MBE System**
4297	60	*n*-type	Old
4298	42	*n-type*	Old
4394	400*	*n*-type	Old
4395	36	semi-insulating	Old
4396	90	semi-insulating	Old
144	60	semi-insulating	New
145	42	semi-insulating	New
146	400	semi-insulating	New

Table 3.1. Tabulated InGaAs/InP superlattice sample parameters. *Sample 4394 was grown with a low-temperature, 500 Å InP cap layer.

All samples were grown with a substrate temperature of 465 °C. The growth times required to achieve each nominal layer thickness were determined by stylus profilometry measurements on previous thick-layer (3000 - 4000 Å) calibration samples. The In/Ga flux ratios required for lattice-matching of the InGaAs layers to InP were established by (400) double-crystal high-resolution x-ray diffraction (HRXRD) rocking curves on the same thick-layer calibration samples. Based on these measurements, the mismatch of the InGaAs layers to the InP lattice is expected to be less than 0.02%.

In GS-MBE, the group-V constituents are supplied primarily in the form of As_2 and P_2 from the pyrolysis of AsH_3 and PH_3 in a dual filament cracker operating at 950 to 1000 °C. Throughout growth, the In flux rate remained constant corresponding to an InP growth rate of 0.532 μm/hr and a V/III flux ratio of 2.0. Growth of the InGaAs layer occurred at a total growth rate of 1.0 μm/hr and a V/III flux ratio of 1.5. Switching of the molecular beams at the InGaAs-on-InP interface occurred by first shuttering the In beam to terminate growth of the InP layer, initiating AsH_3 flow, terminating PH_3 flow, waiting 30 seconds, and then opening the In and Ga shutters to initiate growth of the InGaAs layer. Similarly, molecular beam switching at the InP-on-InGaAs interface occurred by first shuttering the In and Ga beams to terminate growth of the InGaAs layer, initiating the PH_3 flow, terminating the AsH_3 flow, waiting 30 seconds, then reopening the In shutter. This sequence is illustrated schematically in Figure 3.1.

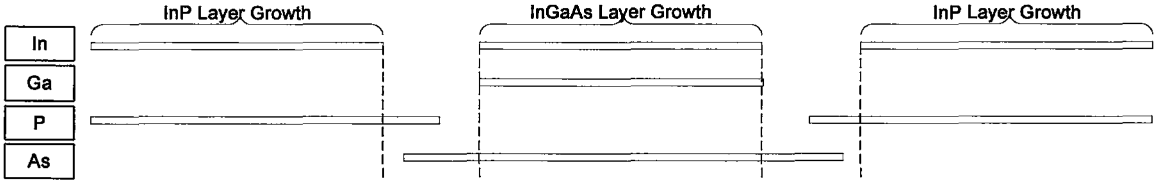

Figure 3.1. MBE gas switching sequence for InGaAs/InP SL growth.

3.3 *HRXRD Results*

The structure of each SL sample was determined by comparing the measured rocking curves to simulated curves based on the interface model explained below. The simulated curves were obtained by using the Bede RADS Mercury (version 3.88) x-ray rocking curve simulation software [3.18] based on the Takagi-Taupin equations of dynamical diffraction theory. Using this software the parameters of the model were varied to optimize agreement between the simulated and the measured rocking curves. Parameter values were optimized by minimization of an error function based on the mean-absolute error of the log-transformed data, instead of a typical mean-square error function. This choice of error function is particularly well suited to x-ray diffraction studies since the relevant features of the experimental data span many orders of magnitude [3.19].

The measured HRXRD rocking curves are shown in Figure 3.2, which exhibit the expected satellite peaks (order n = ±1, ±2, ...) centered around the average composition peak (order n = 0). The SL periods determined from Equation 2.5 are summarized in Table 3.2 (see page 56) and shown on the left side of each curve in Figure 3.2. As expected from Equation 2.5, the satellite separation increases as the superlattice period is decreased.

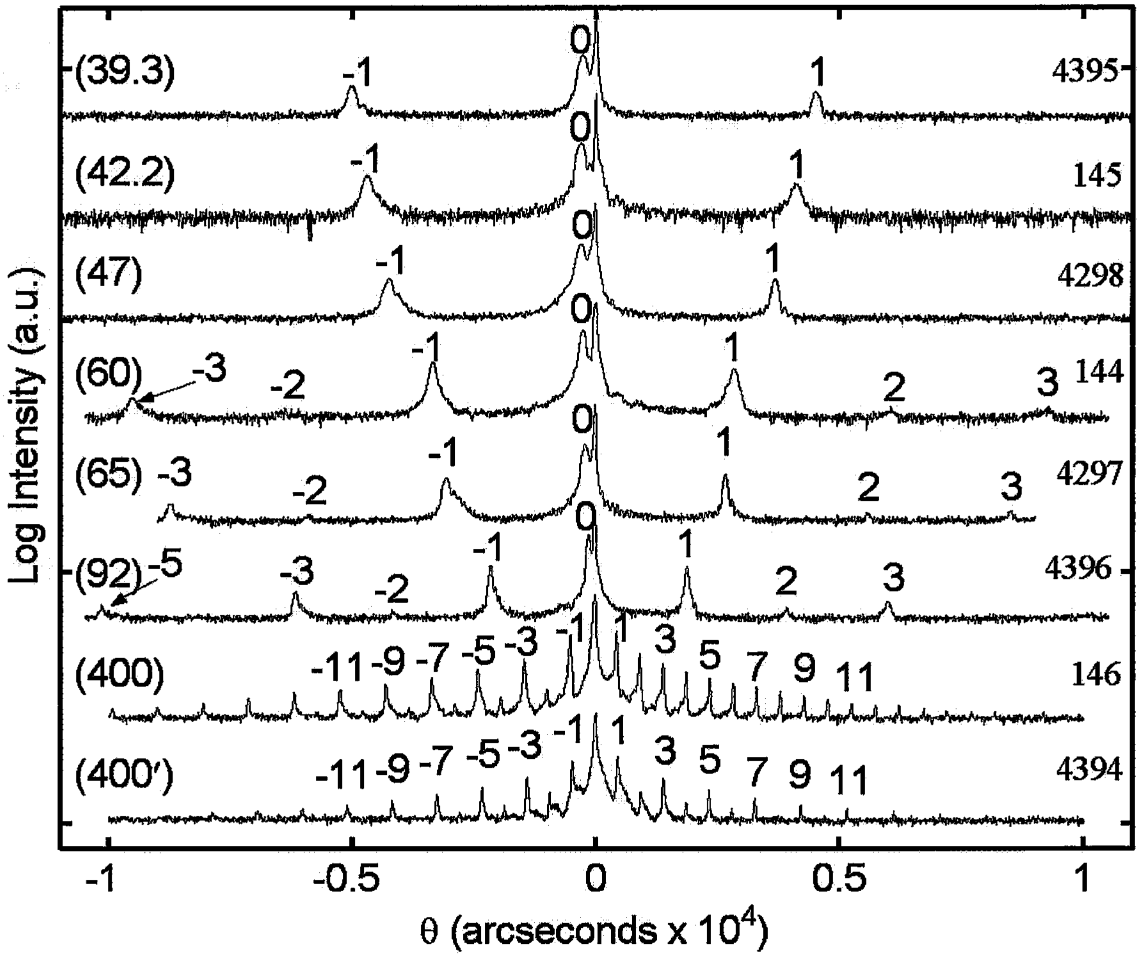

Figure 3.2. Measured HRXRD (400) rocking curves. The measured SL period is indicated on the left of each rocking curve in units of Ångstroms and the sample numbers are shown on the right. Satellite orders are labeled and the curves are offset for visual clarity. The prime indicates the sample with the cap layer.

In the samples with Λ = 400 Å, the average composition peak can just be resolved from the substrate layer peak in Figure 3.2, indicating a slight compressive strain of 0.012% as calculated from Equation 2.4. This splitting is emphasized in Figure 3.3. The splitting of the zero-order satellite peak from the substrate peak increases with decreasing SL period as illustrated in Figure 3.4. The splittings range from ~30 to ~300 arcsec, corresponding to compressive strain ranging from 0.012% to 0.12% as calculated from Equation 2.4. In the case of exact lattice-matching and perfectly abrupt interfaces it is expected that the zero-order peak will not be resolvable from the substrate peak, regardless of SL period. Even if the InGaAs composition was not lattice-matched the peak splitting would remain constant with changes in SL period. A lack of abrupt interfaces can explain the trend demonstrated by the solid line in Figure 3.4, which is a theoretical fit to the data using the structural model (model 2-1) discussed below. Another notable feature in Figure 3.2 is the presence of weak even-order satellite peaks, providing further evidence of non-abrupt interfaces in the SL structure. The intended SLs were to have layers of equal thickness, creating a square wave potential. Thus, for perfectly abrupt interfaces, the even-order satellite peaks are expected to be absent. The presence of even-order peaks in the x-ray diffraction patterns of Figure 3.2 indicates a failure to achieve perfectly abrupt interfaces.

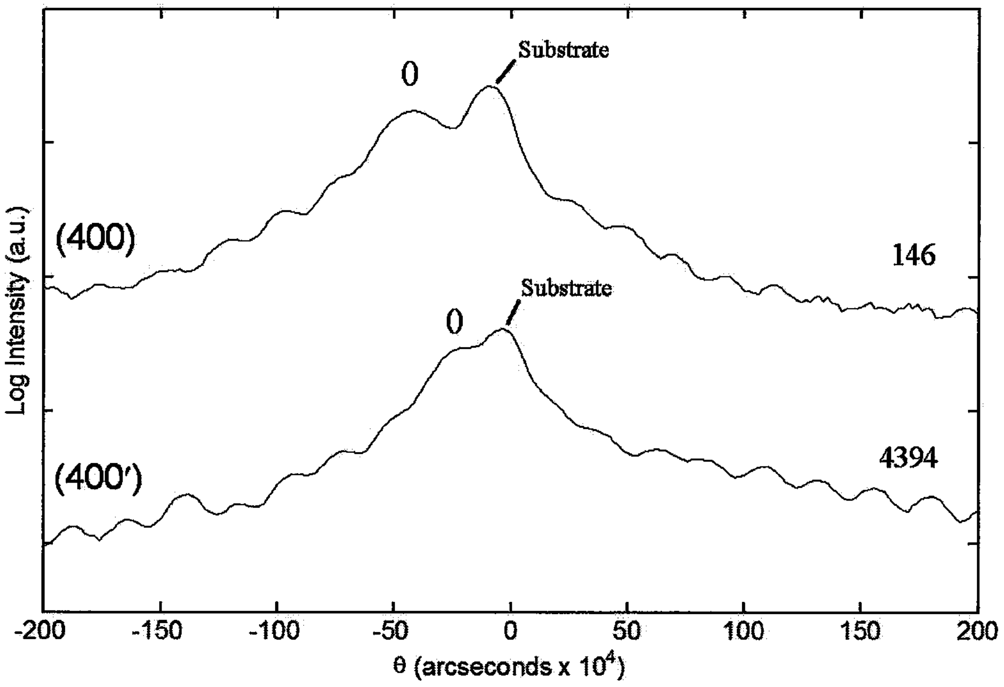

Figure 3.3. Detailed XRD rocking curves of the two samples with Λ = 400 Å. The sample with the cap layer is shown as the lower curve. The zero-order superlattice (labeled 0) peak can just be resolved from the substrate peak.

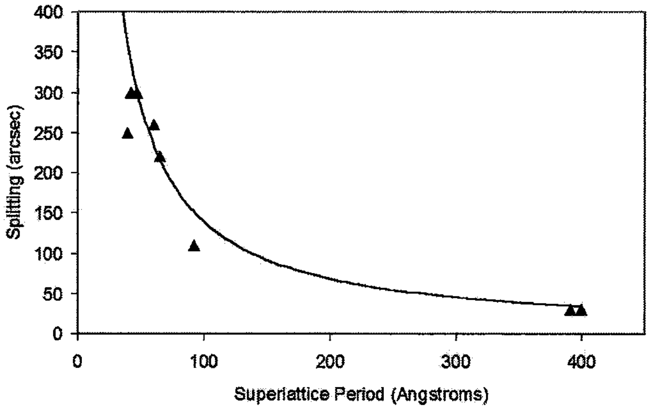

Figure 3.4. Zero-order peak splitting versus superlattice period for measured (triangles) and simulated (solid line) data.

In terms of the consistency in the period of the SLs, the quality is quite good. This is apparent from the small amount of satellite peak broadening that occurs with increasing satellite order. A quantitative analysis of the peak broadening for the $\Lambda = 400$ Å samples shows that the FWHM of the satellite peaks increased by only about 1.5 arcseconds with each consecutive order. Clear broadening with increasing satellite order is a sign of significant variations in the SL period [3.20]. When compared to data from other studies [3.21] the variation in the SL period can be estimated at about 0.3% (~ 0.5 ML).

3.4 *Interface Modeling and Simulation*

To extract more information on the structural details of the interfaces, the HRXRD curves were simulated using different interface models and compared to the measured curves. The general model, shown in Figure 3.5, represents all five of the models considered. Previous work has shown that the P-terminated InP barrier layer in Figure 3.5(a) can have a large portion of its final atomic layer replaced by As during the gas-switching phase of growth [3.22]. The value y_{1a} indicates the fraction of atomic P replaced by As in the top group-V layer of the InP surface at the InGaAs-on-InP interface (interface 1). A second interface layer with As composition given by y_{1b} is introduced to account for the possible deeper penetration of As into an underlying group-V atomic layer. Similarly, y_{2a} and y_{2b} in Figure 3.5(b) indicate the atomic fraction of As at the InP-on-InGaAs interface (interface 2). The resulting interface layer compositions used in the HRXRD simulations are indicated to the right in Figure 3.5(a) and (b). Using this flexible model, various combinations of interface layer compositions were tested and compared to the experimental results.

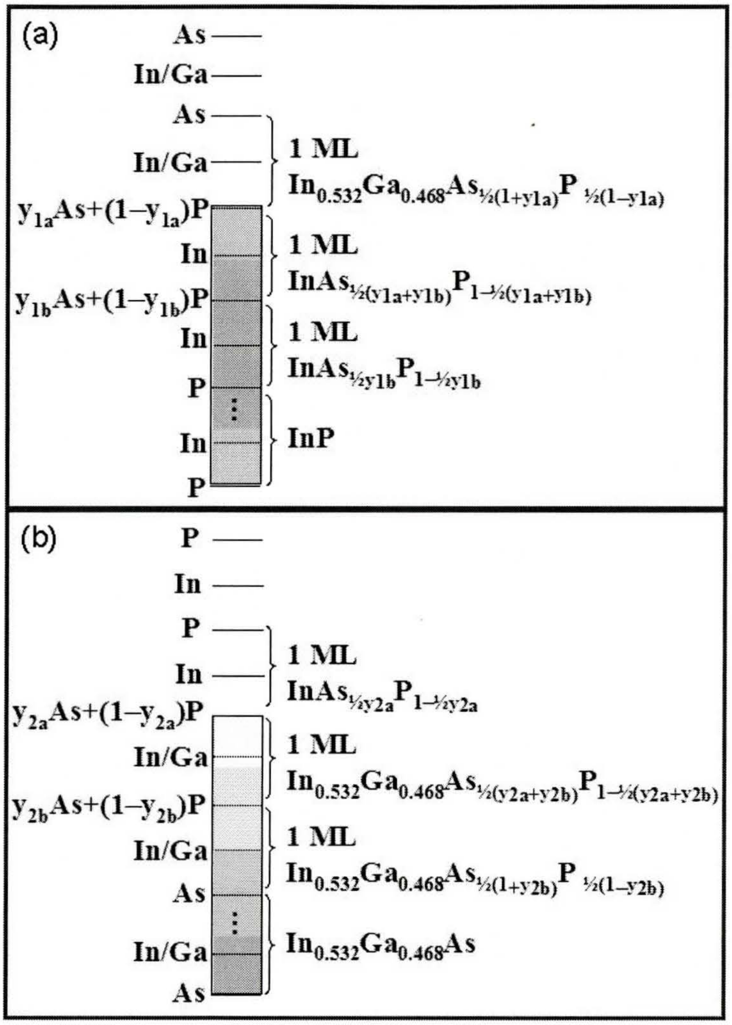

Figure 3.5. Structural model for (a) interface 1 (InGaAs on InP) and (b) interface 2 (InP on InGaAs).

Due to the switching of both the group-III and group-V composition at each interface, an intrinsic strain is present in the structure [3.14]. This strain is present even in the case of perfect lattice matching of the InGaAs wells to the InP barriers, and no group-III or -V atomic exchange across the interfaces ($y_{1a} = 0$, $y_{1b} = 0$, $y_{2a} = 1$, $y_{2b} = 1$), as illustrated in Figure 3.6. Due to the sharing of the group-V atomic layers by the adjacent group-III layers, there exists 1 ML of $In_{0.532}Ga_{0.468}As_{0.5}P_{0.5}$ at interface 1, and 1 ML of $InAs_{0.5}P_{0.5}$ at interface 2. If the structure is grown such that either the group-III or group-V composition remains unchanged across the interfaces, the intrinsic interfacial strain is avoided. This situation is illustrated in Figure 3.7 with an InGaP/InP SL as an example.

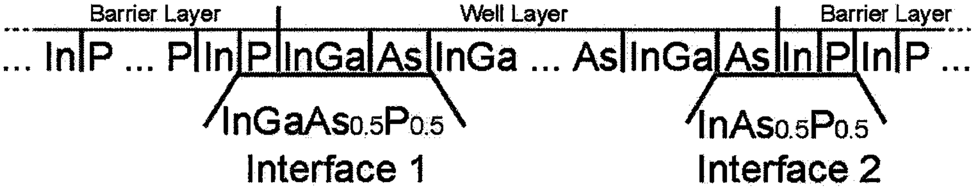

Figure 3.6. Interface layers of a perfect InGaAs/InP SL structure. Transitional material compositions occur at the interfaces due to switching of both the cation and anion species across the interface. These transitional compositions create strain in the structure.

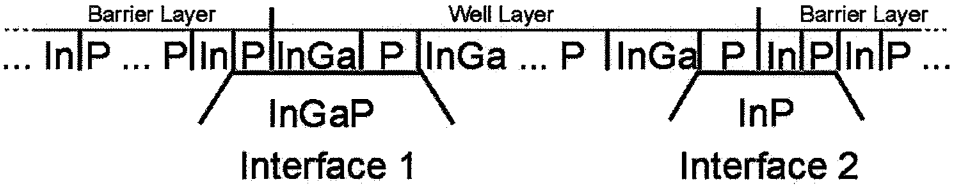

Figure 3.7. Perfect interface model with no group-V change. No intrinsic interfacial strain is present because no transitional material compositions occur.

From a weighted average of the end-member lattice parameters, the lattice parameter of $InAs_{0.5}P_{0.5}$ is 5.9635 Å and the lattice parameter of $In_{0.532}Ga_{0.468}As_{0.5}P_{0.5}$ is 5.7708 Å, resulting in a compressive strain of 1.62% and a tensile strain of 1.67% in these layers, respectively. Thus, a net strain of 0.05% exists for each period of the SL. It is assumed that this strain is confined to the interfaces and not graded through the surrounding layers. The thinnest SLs have a period of 36 Å (12 ML) so the average strain in the structure is at most 0.05%/12 ML = 0.004% and the zero-order SL peak becomes unresolvable from the substrate peak. The primary effect of this intrinsic strain is to increase the intensity of the satellite peaks [3.14]. Thus, for an accurate simulation of the XRD rocking curves of the SLs it is necessary to include this effect.

Simulated HRXRD rocking curves of the structure in Figure 3.6 are shown in Figure 3.8, using the measured period for each sample from Table 3.2. As expected for this model, the satellite peaks spread according to Equation 2.5, and the observed zero-order peak splitting of the measured curves (Figure 3.4) does not appear. Also, the weak even-order satellite peaks in Figure 3.2 are absent in the simulated curves of Figure 3.8. It is therefore necessary to use the more general model of Figure 3.5 to explain the HRXRD measurements.

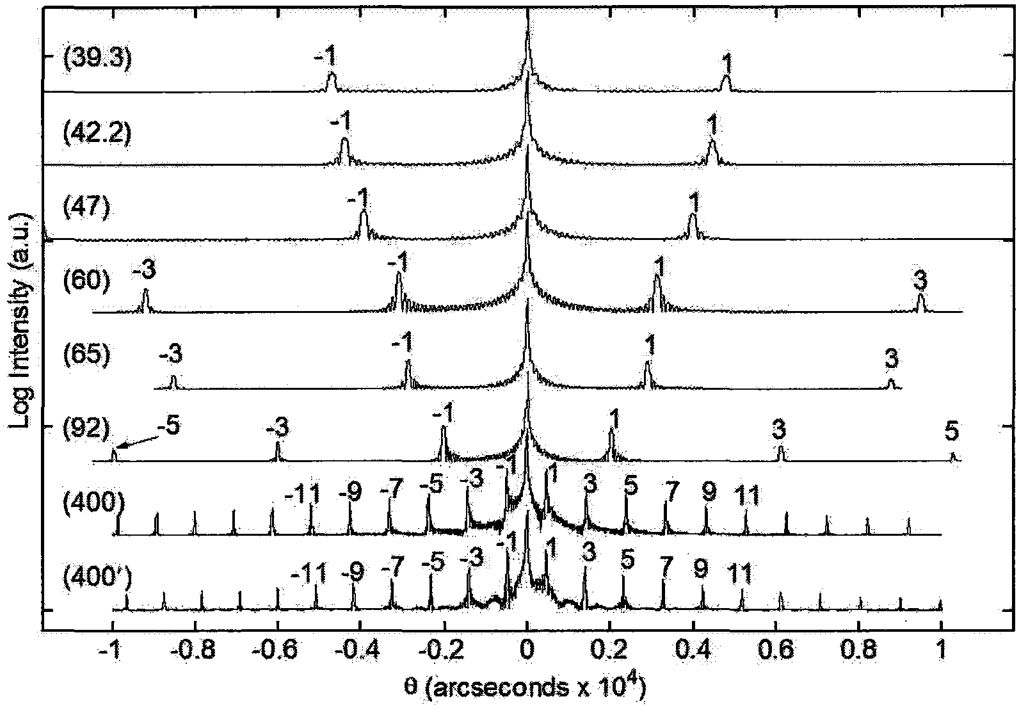

Figure 3.8. Simulated HRXRD rocking curves of the SL structure illustrated in Figure 3.6. The measured SL period is indicated for each rocking curve in units of Ångstroms.

Due to limitations in computing power, and to prevent unphysical results, it was necessary to fix some of the parameter values before commencing the optimization routine. These parameters were: the group-III composition of the InGaAs wells, the individual interfacial monolayer widths, and the superlattice period. Based on previous thick-layer InGaAs calibrations, the In content of each InGaAs well was estimated to deviate by less than 0.3% from the lattice-matched value of 0.532. This was confirmed by the negligible splitting of the average composition peak from the substrate peak in the HRXRD curve for the large period (Λ = 400 Å) SLs in Figure 3.3 and modeling of In-segregation as will be discussed below. This made it reasonable to fix the In content of the wells at 0.532 for the simulations. Negligible exchange of group-III atoms at the interfaces was assumed due to the high sticking coefficients of these elements under the growth conditions used in this work [3.23].

To account for the possibility of residual P present during growth of the InGaAs wells, the P content of the bulk InGaAs in the wells was allowed to vary between 0 and 5%. It was found that the average value of this parameter for all the simulations was 0.9997 ± 0.0005 and thus, by this simulation model, there is insignificant P contamination of the InGaAs wells.

The widths of the interfacial monolayers were estimated from an average of the end member composition lattice parameters. It was found, upon further analysis, that small changes (≤ 0.1 Å) in the thickness of these interfacial layers due to biaxial strain had little effect on the simulated curves, thus confirming the appropriateness of the estimated values. With the InGaAs layer composition and thickness of the interfaces fixed as explained above, an appropriate thickness of the well/barrier layers was found by manual adjustment of the SL period to match the satellite peak spacings in the experimental data. The resulting periods, shown in Table 3.2, are the same as those determined by Equation 2.5. The InP and InGaAs layers were each assumed to constitute half the SL period.

The models were labeled using the notation 1-1, 1-2, 2-1, and 2-2, the first number indicating the number of mixed group-V monolayers in the InP layer at interface 1 and the second number indicating the number of mixed group-V monolayers in the InGaAs layer at interface 2. For the models with only one mixed monolayer at interface 1, y_{1b} was fixed at 0. Likewise, for the models with only one mixed monolayer at interface 2, y_{2b} was fixed at 1. With the appropriate parameters fixed as described above and with parameter value limits set to ensure physical results, the optimization routine was allowed to run. Each simulation took 24 – 48 hours to minimize the error function.

Figure 3.9 shows all 4 simulated curves compared to the experimental data for each of the samples studied. To emphasize the need for group-V atomic exchange at the interfaces, a simulation of the perfect interface structure of Figure 3.6 is also included. Note that the satellite peak positions of the perfect interface model in Figure 3.9 do not match those of the measured rocking curves due to the absence of splitting between the substrate and zero-order peak in the perfect interface model. Also, it can be seen that the 1-1 and 1-2 models have insufficient peak intensities to fit the measured curves, and is particularly prevalent in the samples with period 47 Å, 60 Å, and 92 Å. This observation is clarified in Figure 3.10, in which peak intensities are plotted as a function of peak order for these SLs. It is clear that the solid lines representing the 2-1 and 2-2 models provide an improved fit to the experimental peak intensity data points compared to the dotted lines representing the 1-1 and 1-2 models.

A good fit to the measured peak intensities can be obtained with the 2-1 model, providing evidence of a partial substitution of P with As in the last two monolayers of the InP barrier. Only a slight improvement in fit is observed in the 2-2 model. Based on the fact that As-for-P exchange is preferred to P-for-As exchange [3.23], significant P-for-As exchange in an underlying layer may be unlikely. Therefore, the negligible improvement in fit of the 2-2 simulated curves over the 2-1 curves is not compelling evidence to support a model with a multi-layer P-for-As exchange at interface 2. Thus, it is believed that the 2-1 model best describes the structures.

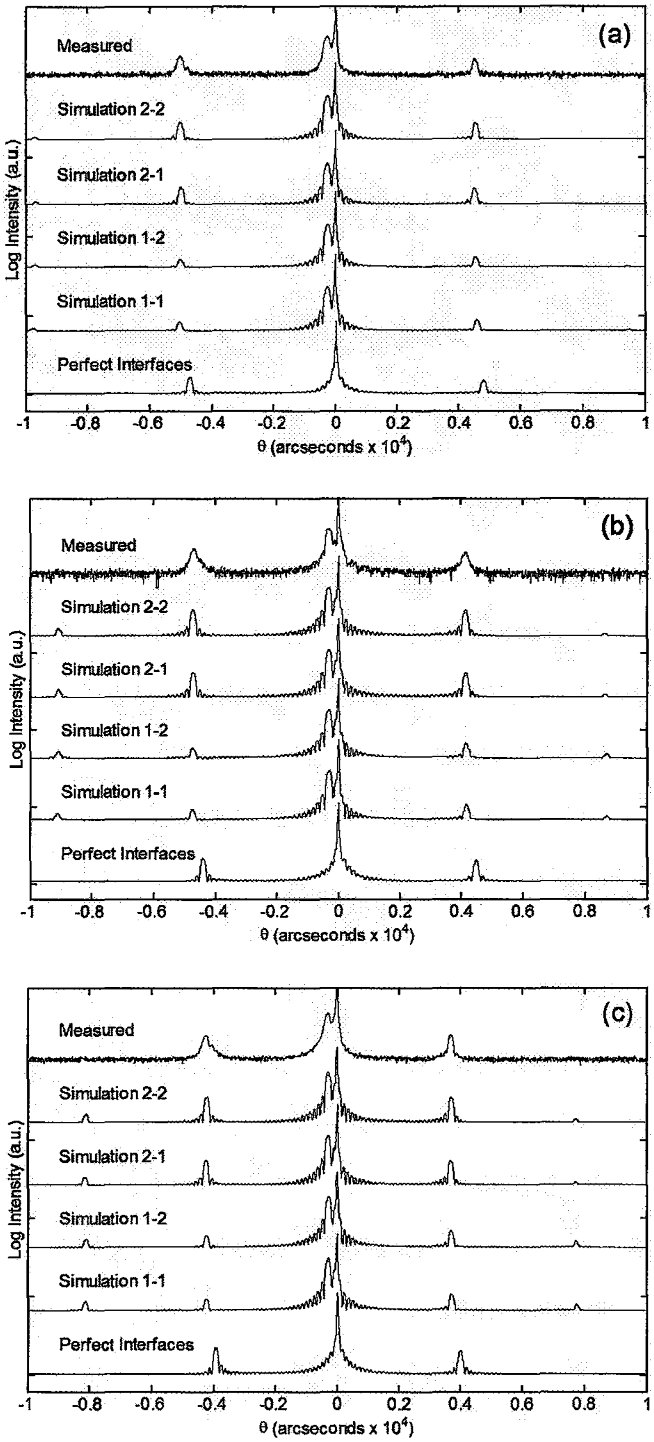

Figure 3.9. Measured and simulated (004) HRXRD rocking curves for each SL sample: (a) Λ = 39.3 Å, (b) Λ = 42.2 Å, (c) Λ = 47 Å, (d) Λ = 60 Å, (e) Λ = 65 Å, (f) Λ = 92 Å, (g) Λ = 400 Å, (h) Λ = 400 Å with cap.

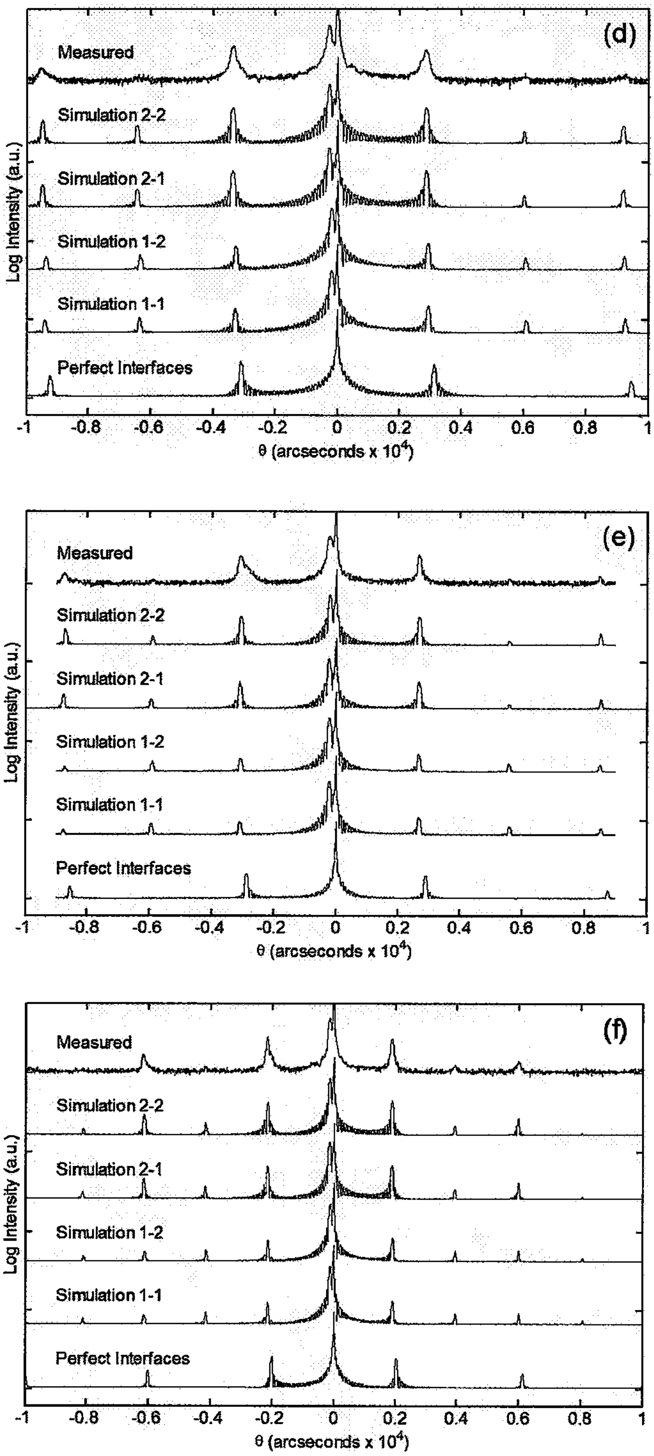

Figure 3.9 (continued)

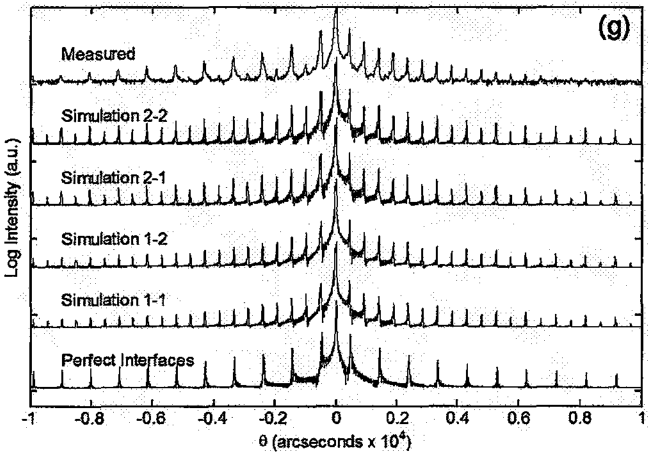

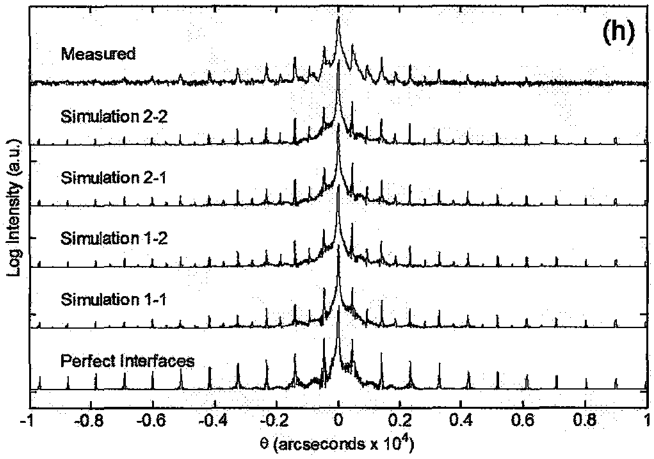

Figure 3.9 (continued)

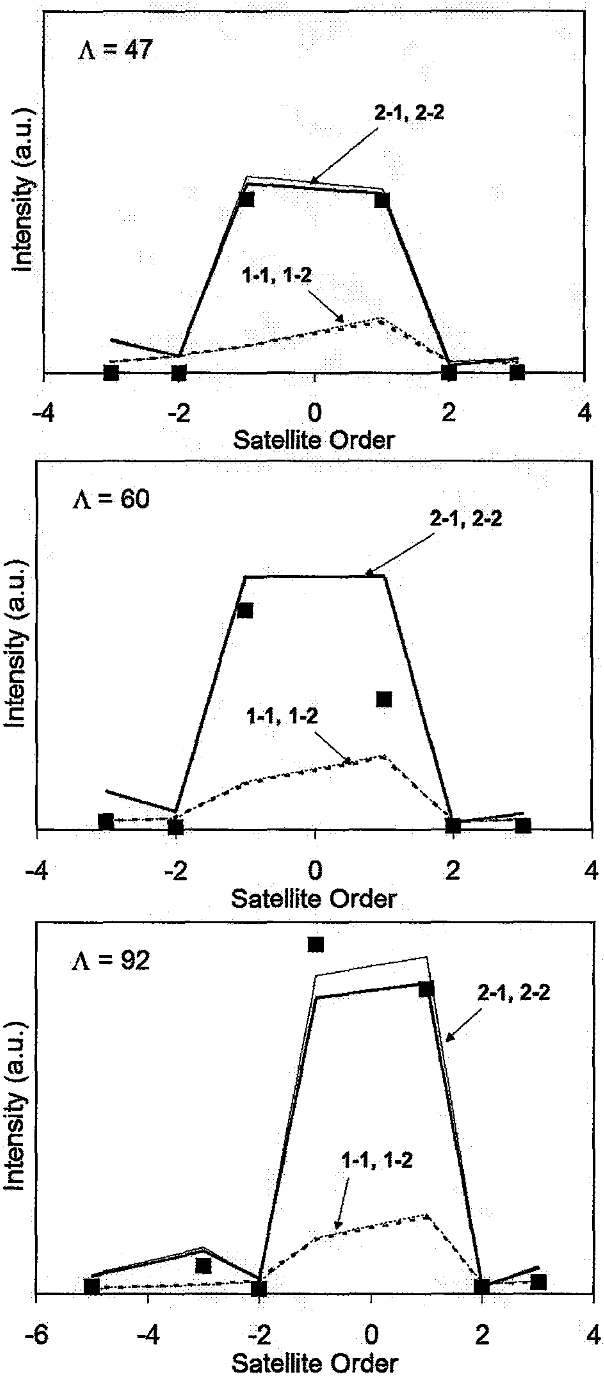

Figure 3.10. Comparison of peak intensities for samples of period 47, 60, and 92 Å for each of the models. The solid lines represent the 2-1 (thick line) and 2-2 (thin line) models, and the dashed lines represent the 1-1 (thick dashed) and 1-2 (thin dashed) models. The experimental peak intensities are shown as square data points.

The compositions of the interface layers, as determined by fitting the 2-1 model to the experimental HRXRD curves, are shown in Table 3.2. For all samples the y_{1a} values are close to unity. This indicates that the top atomic layer of P in each InP barrier is completely replaced by As. The fact that the optimized y_{1b} value is approximately 0.5 on average indicates that about half of the P in the underlying layer is replaced by As. This could be due to the growth of an incomplete monolayer of InP at the time the group-III flux is terminated, allowing the As-flux to cause substitution in a second P-layer. At interface 2 the value of y_{2a} for the 2-1 model was found to be about 0.1 on average indicating that almost all (~90%) of the As at the top interfacial layer is replaced by P.

The sensitivity of the model parameters (y_{1a}, y_{1b}, and y_{2a}) on the "goodness of fit" was estimated by consecutively varying each parameter until the shift in the average composition peak exceeded the full width at half maximum (FWHM) of the substrate peak. This provided a range of interface compositions, shown in Table 3.2, within which a "good fit" of the model to the experimental rocking curves was still obtained. Note that for the 2-1 model the value of y_{2b} was fixed at 1. The relative insensitivity displayed by the $\Lambda = 400$ Å sample may be attributed to the almost negligible thickness of the interface layers in comparison to the SL period in this sample.

Sample Number	Measured Period (Å)	Interface 1 (InGaAs on InP)				Interface 2 (InP on InGaAs)	
		y_{1a} Best Fit	y_{1a} Range	y_{1b} Best Fit	y_{1b} Range	y_{2a} Best Fit	y_{2a} Range
4395	39.3	0.98	0.96-1	0.43	0.39-0.47	0.04	0.02-0.06
145	42.2	1.00	0.98-1	0.53	0.51-0.55	0.02	0-0.04
4298	47	1.00	0.95-1	0.44	0.40-0.48	0.14	0.09-0.19
144	60	1.00	0.83-1	0.56	0.41-0.71	0.08	0-0.23
4297	65	0.97	0.91-1	0.58	0.52-0.64	0.05	0-0.20
4396	92	1.00	0.87-1	0.54	0.41-0.67	0.00	0-0.12
4394	400’	0.86	0.16-1	0	0-0.7	0.32	0-0.87
146	400	1.00	0.65-1	0.26	0-0.61	0.30	0-0.65

Table 3.2. Simulation results for the 2-1 model. Note that y_{2b} was fixed at 1.

From the interface compositions in Table 3.2, parameter values were chosen ($y_{1a} = 1$, $y_{1b} = 0.5$, $y_{2a} = 0.1$, and $y_{2b} = 1$) and substituted into the Figure 3.5 model, resulting in interfacial layer compositions as shown in Figure 3.11. This model was then entered into the software for each SL period to create simulated HRXRD curves using consistent interface compositions for all of the samples. These simulations are shown in Figure 3.12 compared to the measured curves for each sample.

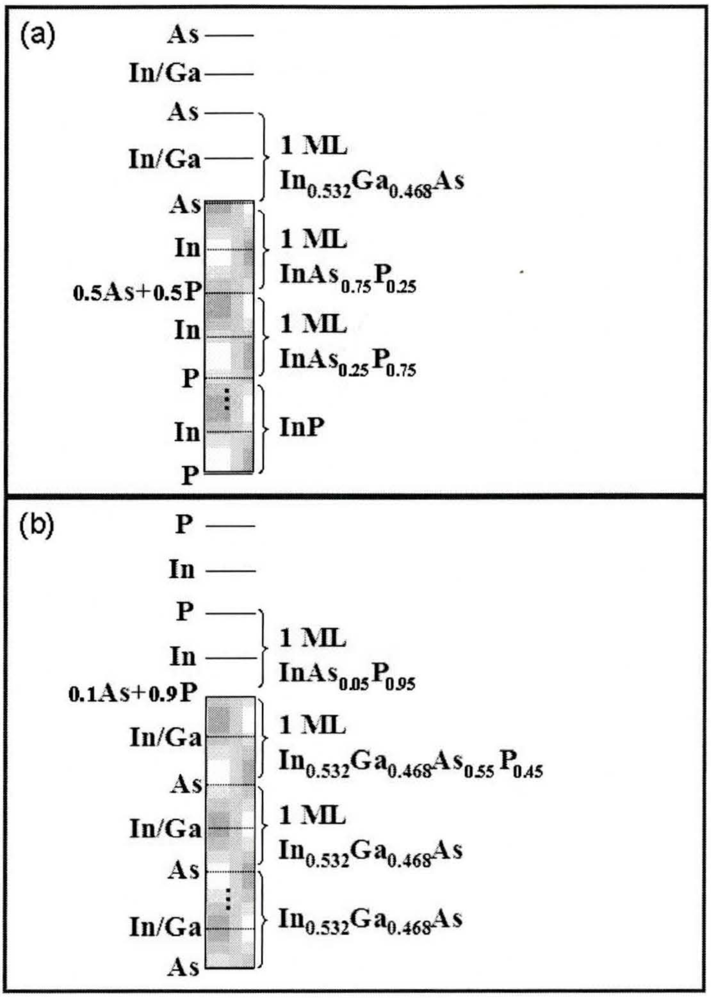

Figure 3.11. Interface 2-1 model from Figure 3.5 with consistent best-fit values derived from computer simulations: $y_{1a} = 1$, $y_{1b} = 0.5$, $y_{2a} = 0.1$, and $y_{2b} = 1$.

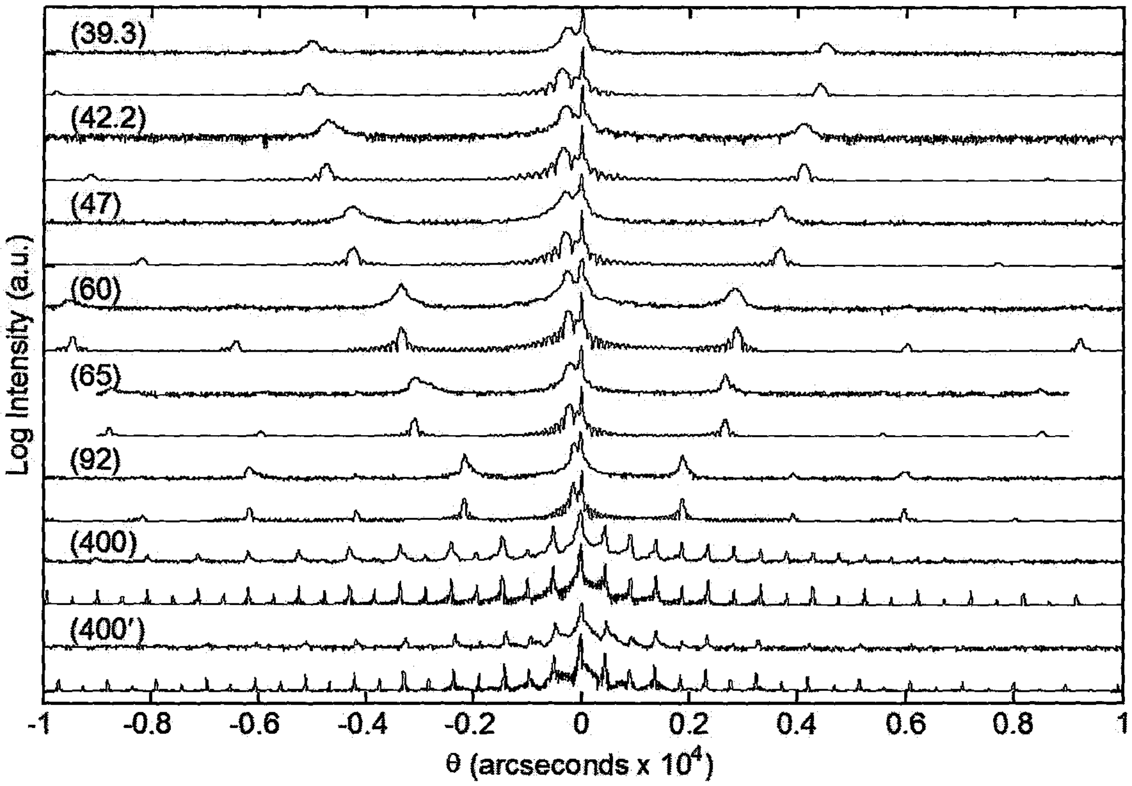

Figure 3.12. Experimental and simulated rocking curves using the same model (model 2-1) and interface layer compositions ($y_{1a} = 1$, $y_{1b} = 0.5$, $y_{2a} = 0.1$, and $y_{2b} = 1$) for each sample. The curves are shown offset for visual clarity with the experimental curve above the simulated curve for each sample. The measured SL period is indicated for each sample in units of Ångstroms.

Figure 3.12 shows excellent agreement between the measured and simulated curves. The shifting of the zero-order peak as a function of SL period as in Figure 3.4 is reproduced. This feature is due to the effect of the additional As in the InP interfacial layers (interface 1) causing the average composition peak to shift further into compressive strain for the shorter period SLs where the interfacial layers constitute a larger fraction of the total structure. Also, the intensities of the measured and simulated SL peaks are in excellent agreement, including the weak even-order peaks. In terms of discrepancies, the simulations were unable to reproduce the second-order peaks of the Λ = 400 Å (sample 146). This sample shows even-order peaks on the positive-angle side of the curve that match the odd-order peaks in intensity. But, as will be discussed below, the fit can be improved upon with the addition of an As tail in the InP barriers. Also, none of the models were able to fit the asymmetry in the satellite peaks. This asymmetry is most obvious in the thinner samples. Figure 3.13 shows the peak asymmetry for the sample with a measured SL period of 47 Å. It is clear from the figure that the asymmetry is not reproduced in the simulation. Furthermore, as can be seen in Figure 3.2, the asymmetry is more pronounced on the negative-order peaks for samples grown on the old MBE system, and roughly symmetric about the zero-order peak for samples grown on the new MBE system. The reasons for this remain unclear. None of the simulations were able to reproduce this effect.

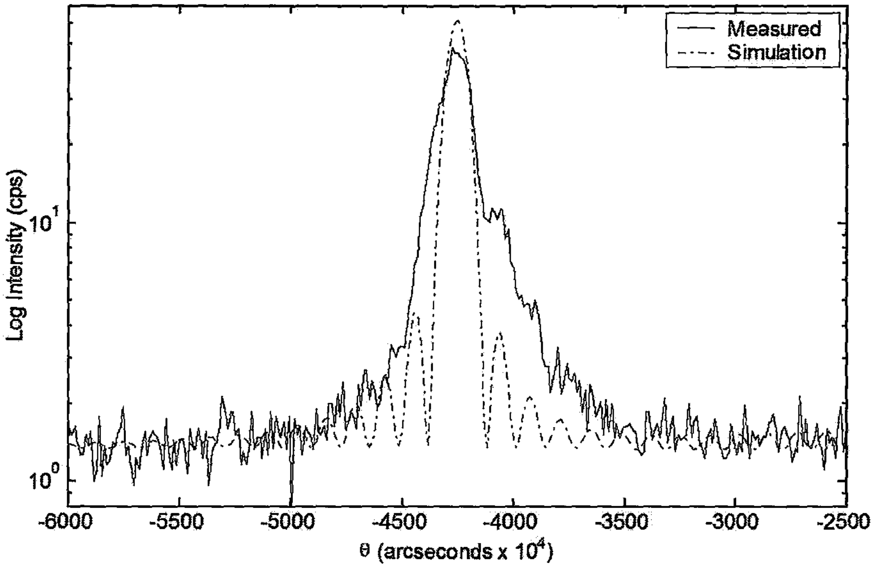

Figure 3.13. Satellite peak asymmetry (n = -1) in the Λ = 47 Å sample.

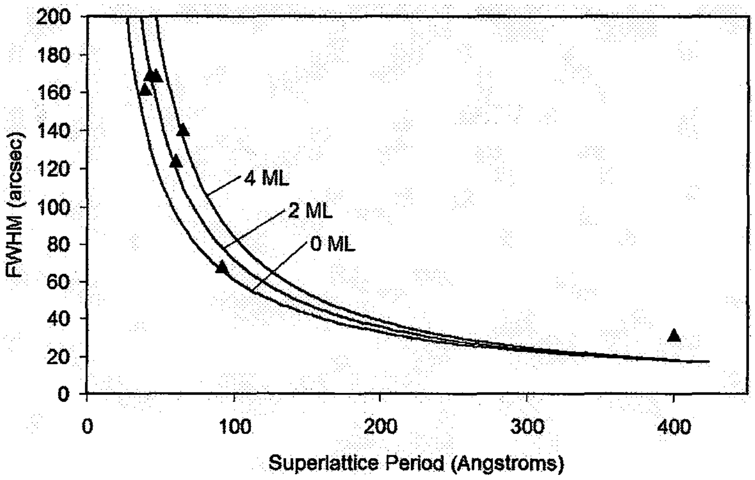

Figure 3.14. Measured (triangles) and simulated (solid lines) FWHM of the n = -1 satellite peak for each sample. Simulated lines based on 0, 2, and 4 ML of interface roughness are shown.

Figure 3.14 compares the measured and simulated FWHM versus SL period for each of the samples studied. The simulated curve labeled 0 ML indicates the FWHM obtained from the 2-1 model results of Figure 3.12. A deviation between the simulated FWHM (0 ML curve) and the measured data is evident for the small period SLs where no interface roughness effects are considered. The influence of interface roughness on the FWHM was estimated by simulating the angular shift in the n = –1 satellite peak due to changes in SL period of 2 ML and 4 ML, as indicated in Figure 3.14. The 2 ML interface roughness line provides the best fit to the experimental data. The origin of this roughness may be partially attributed to the y_{1b} and y_{2a} layers of the 2-1 interface model. The y_{1a} and y_{2b} layers of the 2-1 model, both with full As coverage on average, are unmixed and would therefore not contribute to the roughness. Further evidence of interface roughness has been provided by Raman spectroscopy measurements on these samples as reported elsewhere [3.24, 25].

Our analysis thus far has assumed no As carry-over into the InP barriers after growth of each InGaAs well. However, the presence of graded $InAs_yP_{1-y}$ layers has been suggested by a number of authors [3.26-28]. To determine the influence of this effect, we replaced the single interface layer of $InAs_{½y2a}P_{1-½y2a}$ and the subsequent InP monolayers of each barrier layer in our previous model with an exponential As tail along the growth direction as described by:

$$y_m = y_0 e^{-\beta(m-1)} \tag{3.1}$$

where y_m is the fractional As content of monolayer m (m = 1, 2, ...), y_0 describes the initial As content, and β is a constant describing the composition gradient in the growth direction. A y_0 value of 0.06 and a β value of 0.077 provided some improvement to the fit of the experimental data. The advantages of including the As carry-over effect in the 2-1 model can be seen in the improved fit of the even-order peaks in Figure 3.15, which shows the two samples (144 and 146) for which this improvement was the most noticeable. In particular, this model better characterizes the positive even-order peaks of sample 146 than the 2-1 model. Thus, the composition of the first InAsP monolayer (m=1) in this new model was 0.06, as compared to 0.05 (=$½y_{2a}$) on average for the previous model. The small β value indicates that this As tail can be spread across many monolayers, reducing the barrier potential. The presence of As in the InP barriers will be further supported by the photoluminescence results in the following section.

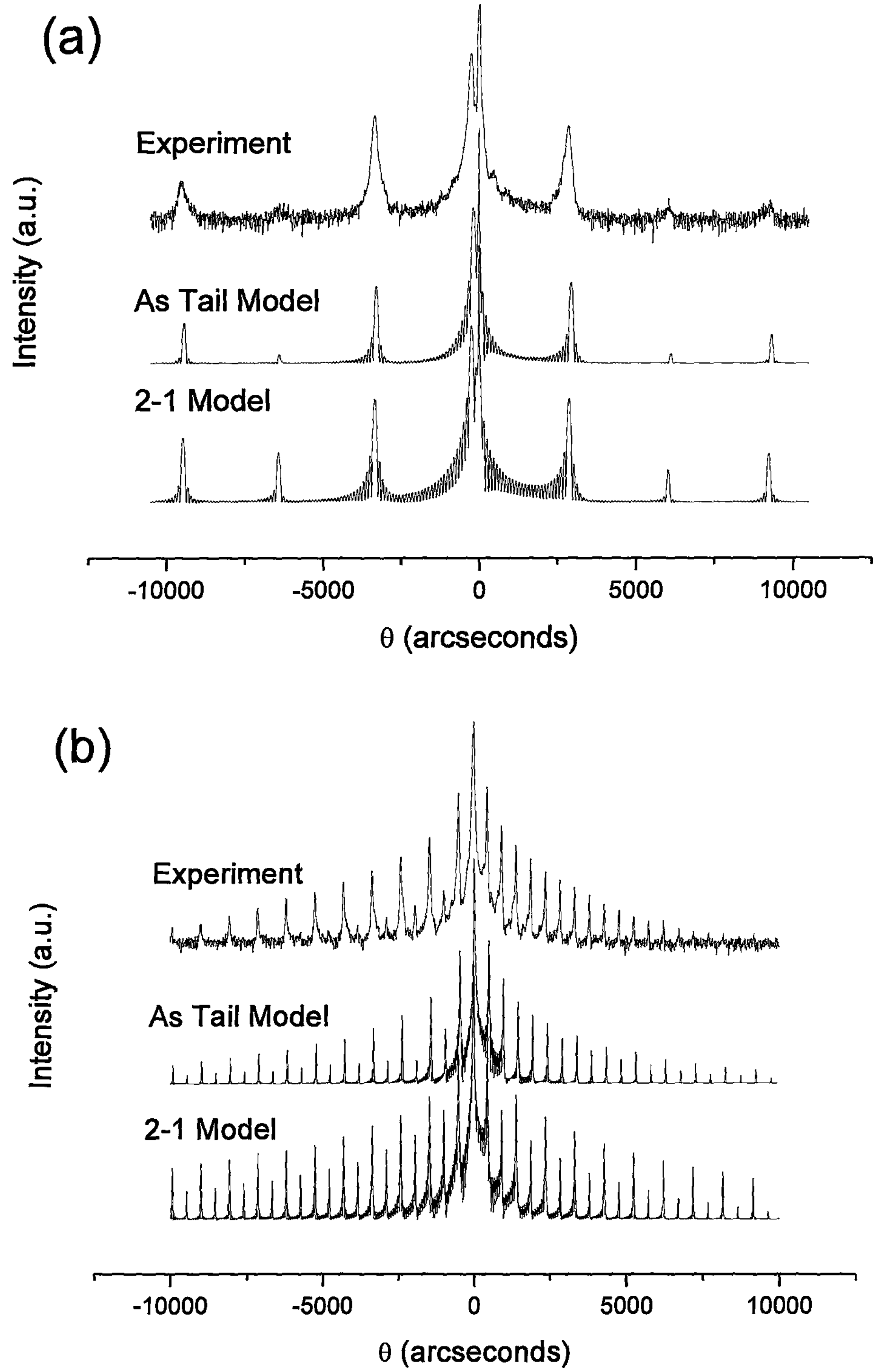

Figure 3.15. As carry-over simulations as compared to experiment and 2-1 models for (a) sample 144 and (b) sample 146.

Previous studies have shown that, during growth of the InGaAs well, a fraction of the available In can segregate to the growth front [3.29]. To model this effect, the indium content (x_m) of each monolayer m (m = 1, 2, ...) of InGaAs in the previous model was allowed to vary according to:

$$x_m = 0.532(1 - R^m) \tag{3.2}$$

where R is a constant describing the composition profile [3.29]. The best results were achieved with an R value of 0.0078. Thus, simulations allowing for this effect suggested that there was no significant In-segregation in the samples investigated in this study.

3.5 Photoluminescence Results

Photoluminescence spectra of each of the SL samples were gathered at temperatures ranging from 23 K to 300 K (room temperature). The spectra of one of the SLs is shown in Figure 3.16, showing a low-temperature main emission peak at 0.927 eV and lower energy transitions around 0.90 eV which are probably due to unresolved donor- and acceptor-related transitions as observed by other authors [3.30].

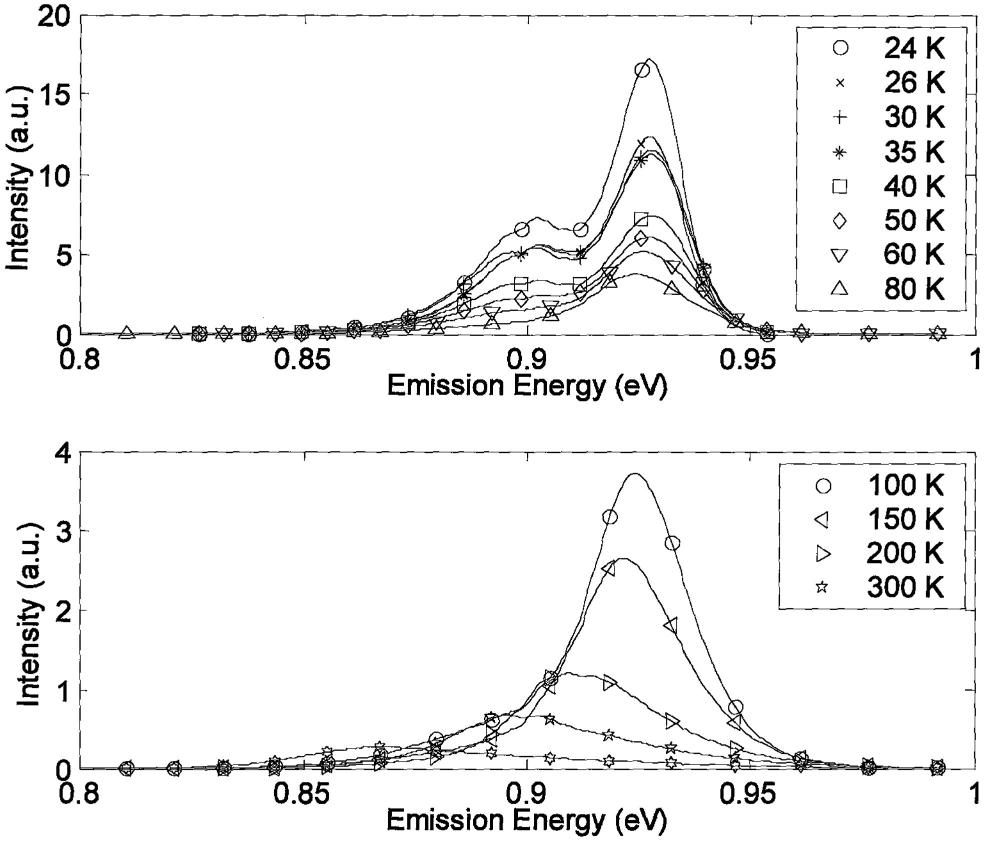

Figure 3.16. PL spectra measured at various temperatures for sample 4297 (Λ = 65 Å). The spectra are divided into two temperture brackets to aid visual clarity.

With rising temperature the spectrum intensity decreases due to competitive non-radiative transitions [3.31] and the main emission peak shifts to lower energies. This red-shift occurs due to the combined effect of the electron-phonon interaction and thermal expansion of the lattice [3.32, 33], and can be described by the Varshni equation:

$$E_g(T) = E_g(0) - \frac{\alpha T^2}{T + \beta} \tag{3.3}$$

where E_g and T represent the material bandgap and temperature, respectively. α and β are material dependant, empirically determined parameters. To summarize the temperature-dependence of the peak emission observed in the present study, Figure 3.17 displays the main emission peak location for all samples as a function of temperature. As the SL period decreases the energy of the emission increases. This effect is due to the strengthening of the quantum confinement as the wells become thin.

An interesting feature of the data is the subtle blue-shift as the temperature rises from 23 to 45 K. This peak is present in only the thinnest SLs (Λ < 60 Å). One possible suggestion as to the origin of this peak is that it is caused by phase separation of the InGaAs into small InAs- and GaAs-rich regions. This effect is explored further in Section 3.6.2.

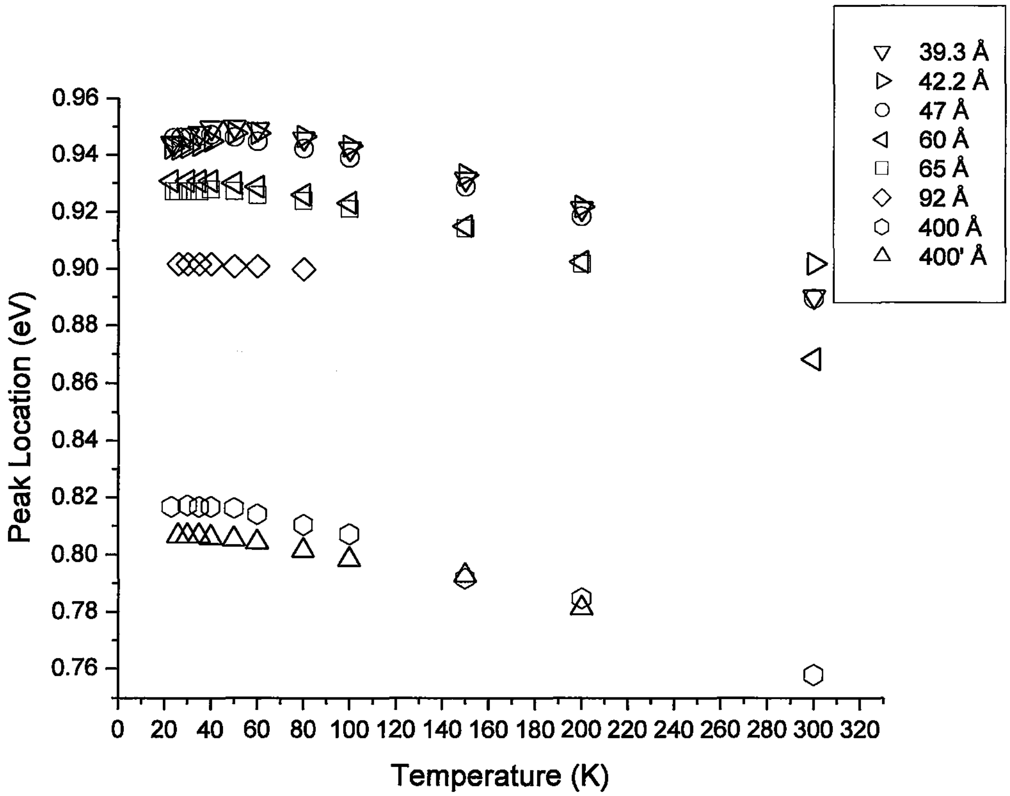

Figure 3.17. Temperature dependence of PL emission energy for all measured spectra.

In support of the interface model derived from the HRXRD experiment, the FWHM of the PL spectra show, in general, an increase in peak broadening as the SL period is decreased. These results are shown in Figure 3.18. The increase in PL peak width with decreasing SL period is further evidence of the presence of the interfacial layers described by Figure 3.5 and phase separation [3.34-36] discussed in Section 3.6.2. As an inconsistency in these results (not shown), the FWHM of sample 146 is widest at almost all temperatures even though it has a large SL period of 400 Å for which the effects of small potential variations should not be noticeable. This sample also showed the highest emission intensity.

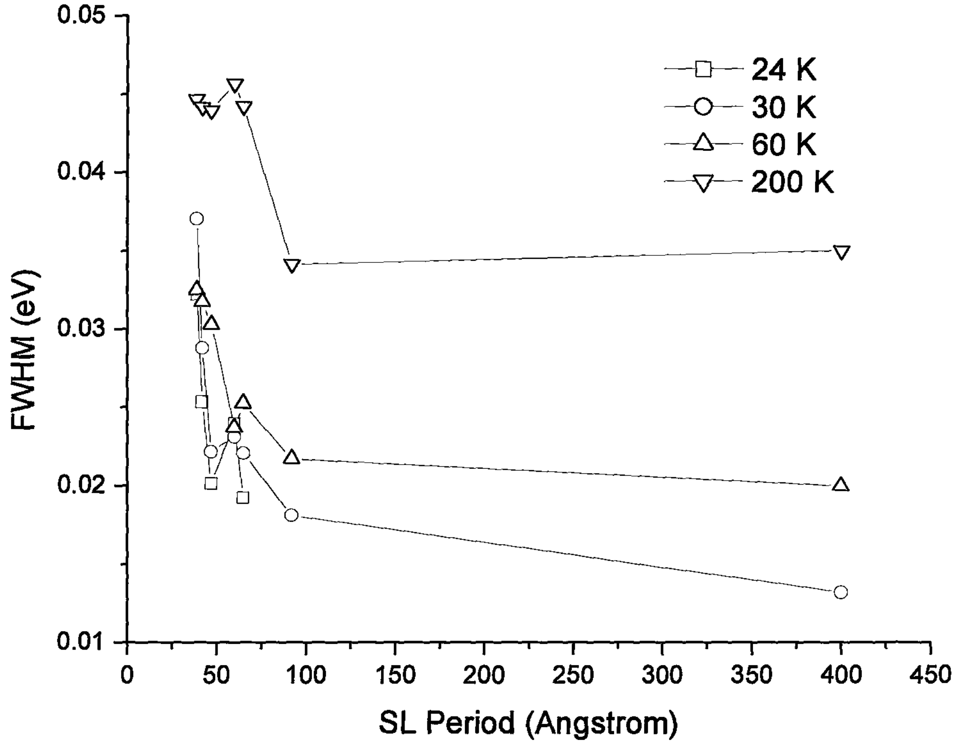

Figure 3.18. FWHM of SL PL spectra as a function of SL period for a number of temperatures.

3.6 Photoluminescence Modeling and Discussion

To better understand the observed trends, simulated curves were produced to estimate the expected peak energies for each SL at each temperature. To simplify the simulation process, the potential profile of the $In_{0.53}Ga_{0.47}As$ regions were approximated by single finite square wells (FSWs). It is important to note that this simplification neglects the effects of carrier wavefunction interactions from tunneling between adjacent wells in the superlattices [3.37]. However, the model suffices as a starting point from which the contribution of many additional effects can be discussed. With this simplification of the problem, the InP and $In_{0.53}Ga_{0.47}As$ band parameters were gathered from the work of Vurgaftman et al. [3.38], and a temperature-dependent model of the quantum well was constructed. This model took into account the temperature-dependence of both the energy bandgap, according to Equation 3.3, and the band offset, according to empirical studies. A schematic of the model used for these simulation calculations is shown in Figure 3.19.

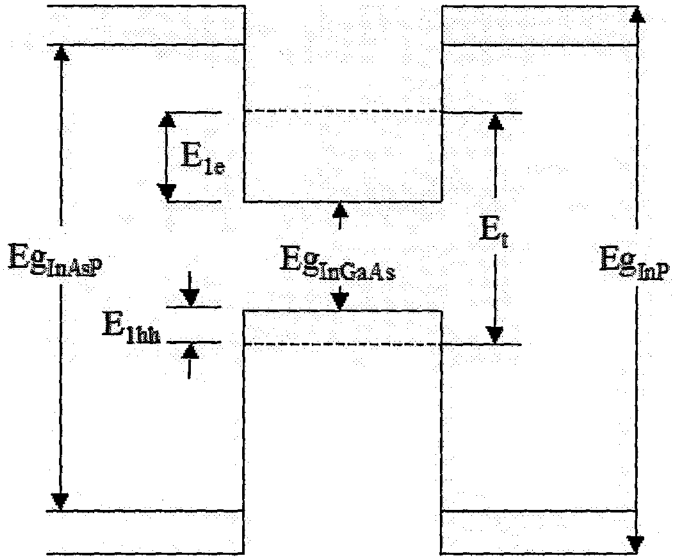

Figure 3.19. Finite square-well model of $In_{0.53}Ga_{0.47}As/InP$ quantum well (not to scale). The model shows the transition (E_t) from the ground-state electron level to the ground-state heavy-hole energy level. The decreased barrier height caused by the slowly decaying As tail in the barriers is also illustrated.

Using this model, the FSW potential problem can be solved for the energy levels by a simple iterative process, as demonstrated by Murphy and Phillips [3.39]. For a potential well of depth V_0, defined by the bandgap and valence band offset of the InGaAs and InP, and of width $2a$, the bound states can be described by the following transcendental equations:

$$y = \eta|\cos y| \tag{3.4}$$

for even-parity solutions, and

$$y = \eta|\sin y| \tag{3.5}$$

for odd-parity solutions, where

$$y = qa \tag{3.6}$$

and

$$\eta^2 = \left(2mV_0a^2\right)/\hbar^2 \tag{3.7}$$

where *m* is the effective mass of the particle (electron or hole). Equations 3.6 and 3.7 arise out of a need to arrive at equations in the form *y* = *f(y)* so that the method of direct iteration can be used to find numerical solutions for *y* [3.39]. Having obtained *y*, the confinement energy for a particle in such a potential well can be extracted from the equation,

$$E = \frac{y^2}{a^2}\frac{\hbar^2}{2m} - V_0 \tag{3.8}$$

These calculations were carried out for temperatures ranging from 20-300 K and well widths ranging from 30-400 Å, with the potential barriers adjusted accordingly to account for changes in temperature [3.38]. Transition energies were calculated based on a transition from the ground-state electron level in the $In_{0.53}Ga_{0.47}As$ well conduction band to the ground-state heavy-hole level in the $In_{0.53}Ga_{0.47}As$ well valence band. Due to the much lower effective mass of the light-hole as compared to the heavy-hole, the transition probability to the light-hole band is significantly lower [3.40]. Through these calculations the energies of the electron and hole in their respective quantum wells can be calculated separately and added to the $In_{0.53}Ga_{0.47}As$ bandgap to arrive at the theoretical energy transition.

As stated above, the simulated curves are based on a FSW model, and so are expected to overestimate the peak transition energy. This overestimation results from the failure of this model to account for the interaction effects between carrier wavefunctions as they tunnel through the thin barriers of the quantum wells in the SLs. This effect increases as the barrier layer thickness decreases (shorter SL period) since the thinner barriers permit a higher tunneling probability. Figure 3.20 shows the simulated curves as compared to the experimental results from Figure 3.17, with Simulation 1 resulting from the calculation as described above. As expected, this simulation shows a large overestimation of the emitted photon energy in the case of the shorter SL period and a much better agreement as the period increases, especially at higher temperatures. In the case of Figure 3.20g and Figure 3.20h the well width is large enough that the confinement effects can be ignored and the analysis becomes similar to the analysis of bulk $In_{0.53}Ga_{0.47}As$. Note that the model also fails to reproduce the small blue-shift in the thin SLs ($\Lambda < 60$ Å).

In addition to the neglected SL effects, there are a number of other physical effects that can cause the observed problems with Simulation 1. Improvements to the model can be made by including the As tail in the barriers, as described by Equation 3.1 (Simulation 2), and the effect of 2 MLs interface roughness shown in Figure 3.14 (Simulation 3). Also, the effect of phase separation in the InGaAs wells on the line shape must be considered. These effects are described below.

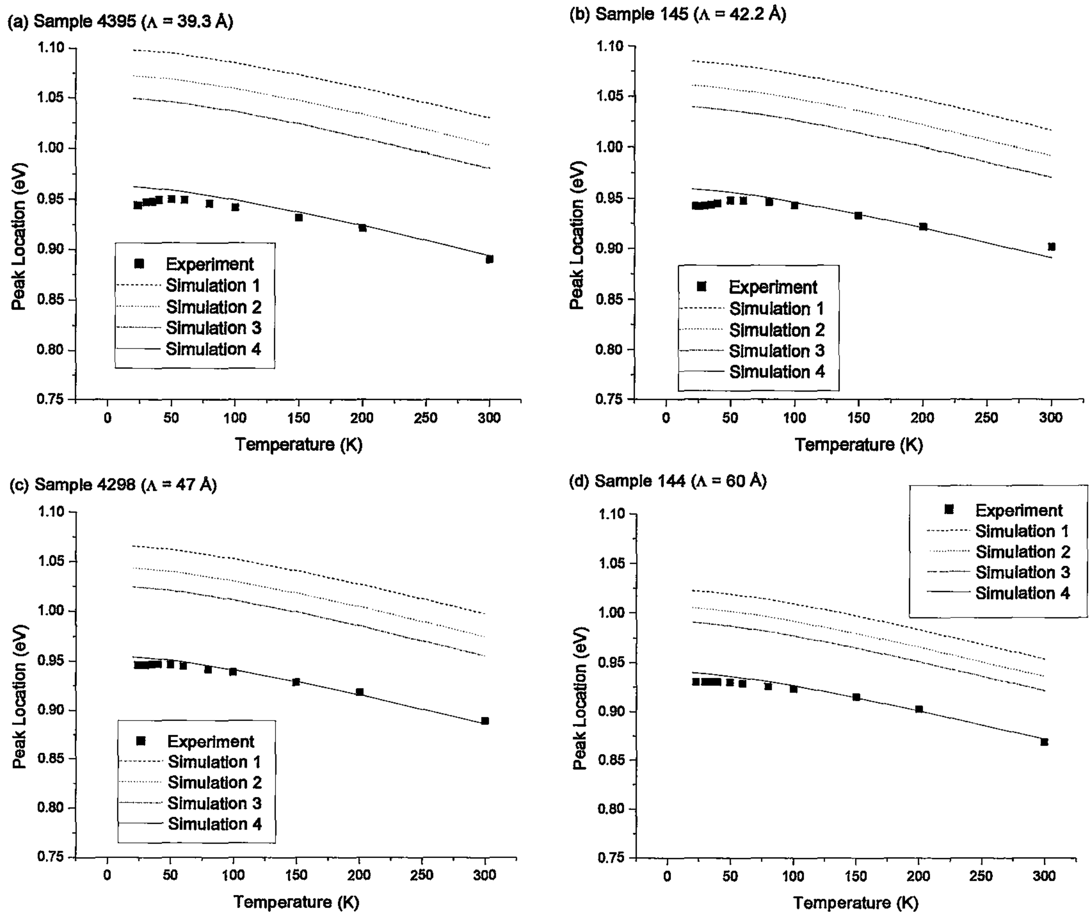

Figure 3.20. Simulated and experimental photoluminescence emission peak location as a function of temperature for all SL samples. Simulation 1 is a FSW model with pure InP barriers. Simulation 2 accounts for a 5% As content in the barriers. Simulation 3 adds to Simulation 2 an estimate of the effect of the interface roughening from Figure 3.14. Simulation 4 accounts for all of the above effects and also includes the interaction of the carrier wavefunctions across the SL barriers.

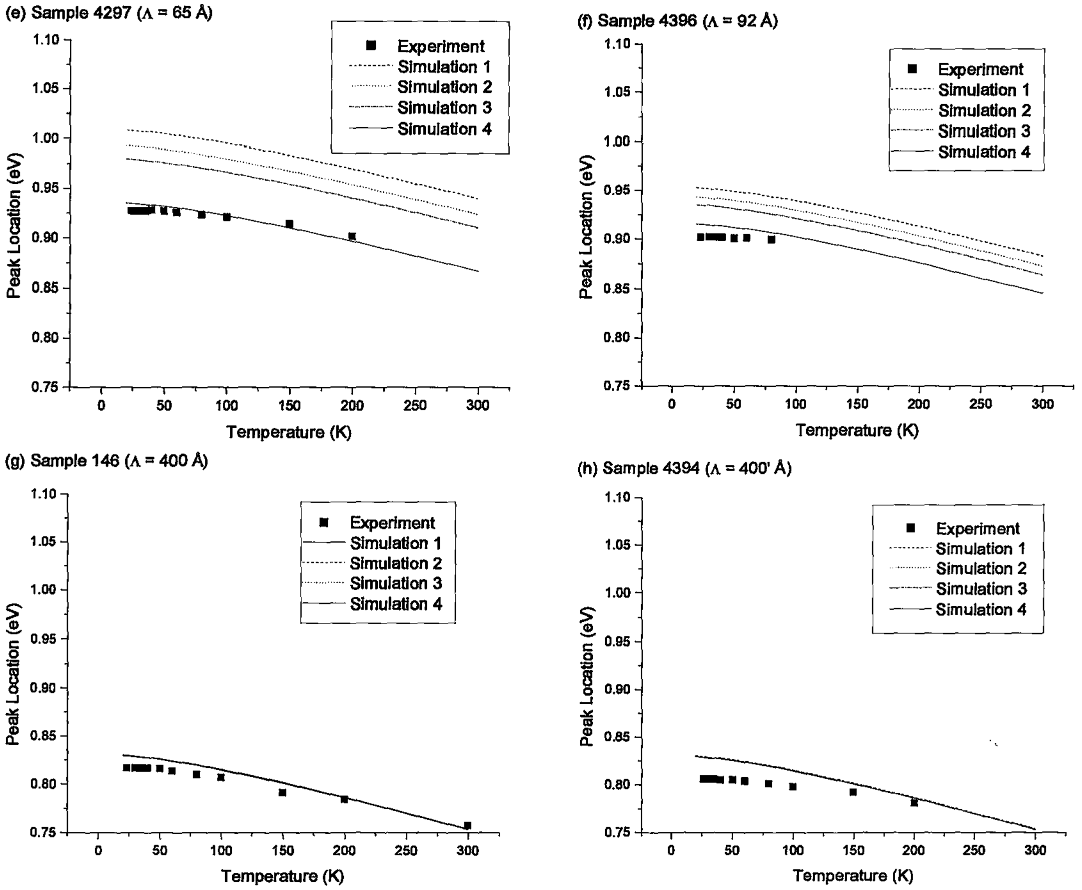

Figure 3.20 (continued)

3.6.1 Exciton Binding Energy

The formation of excitons can reduce the PL emission energy due to the amount of energy contained in the exciton bond. Excitons occur as an interaction between an electron and a hole, forming a quasi-particle similar to a hydrogen atom, with the electron and hole orbiting each other. The energy of the photon emitted from recombination of these carriers is reduced by the binding energy of the exciton. In $In_{0.53}Ga_{0.47}As$ this binding energy has been measured as 2.5 meV [3.41]. Excitons can also be bound to impurities such as donor or acceptor atoms, in which case they cause a milder reduction in the recombination energy of ~0.1 meV. Since the InGaAs wells were grown with no doping they are expected to be quite pure. Thus, the presence of free excitons can then account for a small part of the discrepancy between the simulated and experimental data shown in Figure 3.20.

3.6.2 Phase Separation

As has been observed in previous studies on ternary InGaAs and quaternary InGaAsP alloys, phase separation of the material into In- and Ga-rich regions is possible and depends on the growth temperature [3.34-36]. At our growth temperature of 460 °C, growth takes place just on the borderline of the miscibility gap. Therefore, this effect cannot be ruled out. The phase separation of InGaAs into regions of InAs- and GaAs-rich material has the effect of creating pockets of small wells in which the lower bandgap material (InAs-rich) acts as a collector for the carriers, catching them in a potential well with a slightly deeper profile than the pure InGaAs wells (Figure 3.21). A relationship between these potential variations and the subtle low-temperature shift observed in Figure 3.17 has been suggested in other InAlAs/InGaAs/InP SL studies [3.42, 43]. The shifts created in these other studies are on the order of 0.1 meV, whereas in the current study we observe shifts on the order of 4 meV. This discrepancy is due to the fact that the potential wells in which this effect is observed in the present study are deeper and narrower than the InAlAs/InGaAs wells studied by Pocas et al. [3.42, 43]. Thus, potential variations in these deep, narrow wells create a greater shift in the carrier energy as they are localized to the InAs-rich regions.

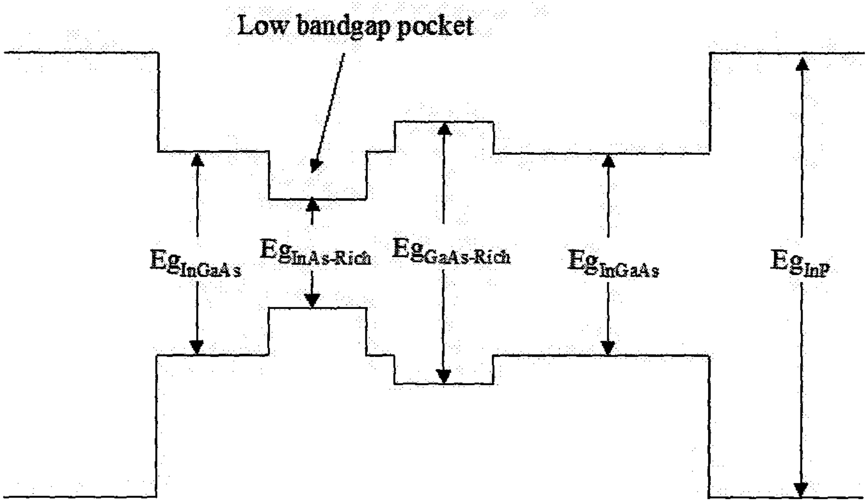

Figure 3.21. Schematic depiction of the effect of phase separation on InGaAs quantum wells.

3.6.3 Arsenic Carry-Over into the InP Barriers

As mentioned in section 3.4, the XRD results indicate that the presence of a significant As content in the InP barriers (Figure 3.15) is probable [3.26-28]. In terms of PL, this As tail has the effect of shifting the barrier composition to ~$InAs_{0.05}P_{0.95}$, a composition with a larger lattice constant and a smaller bandgap (Figure 3.19). The low β value from Equation 3.1 means that this barrier height reduction is almost completely flat as illustrated in the schematic. Thus, the result is a lower barrier, less confinement, and a lower transition energy. Simulated curves were produced from this modified model and are identified in Figure 3.20 as Simulation 2. These curves provide some improvement to the model, bringing the simulated curve closer to the experimental data at low Λ values, but having no effect at high Λ values.

3.6.4 Interfacial Layers

The presence of interfacial layers, as described by Figure 3.5 is another possible cause for the increasing overestimation of the expected emission energy at shorter SL period. These interfaces cause a warping of the edges of the quantum well, reducing carrier confinement, and permitting a lower ground-state energy. The curves labeled as Simulation 3 in Figure 3.20 show the combined effect of the As tail in the barriers and an approximation of the interface layer effects of Figure 3.11. For simplicity, this effect is modeled as a simple widening of the barriers by 2 ML as estimated from Figure 3.14. This simulation provides additional improvement to the fit of the simulated curves to the experiment.

3.6.5 Superlattice Mini-Band Effects

The significance of the superlattice effects is made clear in Figure 3.20, in which the combined effects of the As carry-over and interfacial effects as part of the FSW model are unable to fit the experimental data (Simulation 3). To quantify this effect the Kronig-Penney model was employed, along with the calculated band parameters at 30 K [3.38]. This model is particularly applicable to the SL structures since its prime use is a simplified square-well potential model of a one-dimensional lattice of atoms. As the SL period becomes thinner, the tunneling between the wells becomes more significant, and just as the effect in a lattice of atoms is to create energy bands, the discrete energy levels of the FSW model split into mini-bands [3.37]. Using the mathematical treatment described by Pierret [3.44] and solving graphically, the energy difference between the lowest edge of the electron mini-band and the highest edge of the heavy-hole mini-band was calculated at 30 K for each SL period. This effect, coupled with the As tail and interfacial layer effects, is shown in Figure 3.20 as Simulation 4. The fit to the experimental data is excellent, with some deviation due to the phase separation effects described in 3.6.2.

3.7 Chapter Summary

HRXRD studies of InGaAs/InP SLs have suggested an interface model in which complete exchange of P with As in the top monolayer, and partial (~50%) exchange in the second monolayer, occurs in the InP layer for growth of InGaAs on InP. In the case of InP on InGaAs, about 90% exchange of As with P occurs in the top monolayer of InGaAs with no exchange in the underlying monolayers. Surface roughness was estimated to be ~2 ML. HRXRD simulations also support the presence of ~5% As content in the InP barriers due to residual As in the growth chamber. Asymmetry in the satellite peaks was not reproducible in the simulated curves. The presence of interfacial layers and As carry-over into the InP barriers are supported by temperature-dependent PL measurements. This analysis provides a baseline for an understanding of the interface growth mechanism in the InGaAs/InP heterostructure NWs discussed in Chapter 5.

4 InP Nanowires

4.1 Introduction

VLS can be implemented in a variety of growth systems, but InP NWs have been grown predominantly by metal-organic vapor phase epitaxy (MOVPE) [4.1-5]. The growth of InP NWs by GS-MBE provides a starting point in the understanding of ternary InGaAs/InP heterostructure NWs presented in the following chapter. Further to this end, MBE NW growth and the Au particle self-assembly process in the InP material system is compared to the GaAs system in order to develop an understanding of how the VLS process changes with changes to the source material.

Also, this study of InP NWs grown by GS-MBE showed an important connection between NW length and rotational twinning (stacking faults). Semiconductor NWs grow almost exclusively along the low-energy (111)B direction where they often exhibit stacking faults consisting of zincblende (ZB) and wurtzite (W) polytypism [4.2, 4, 6]. Since crystal structure can influence optical and electrical properties, it is important to control and possibly eliminate stacking faults in NWs [4.3]. This chapter presents, NWs grown by GS-MBE along the (111)B direction that are free of stacking faults below a certain critical length.

4.2 InP Nanowire Growth and Sample Preparation

The NWs in this study were grown by the VLS process on an *n*-type InP (111)B substrate using self-assembled Au nanoparticles as catalysts. The substrate was exposed to a 20 minute UV-ozone treatment, etched for 30 seconds in a 10% buffered HF solution, and rinsed in de-ionized water. The substrate was then transferred to an electron-beam evaporation system in which 4 nm of Au was deposited, as measured by a quartz crystal thickness monitor. The substrate was then transferred in ambient air to the GS-MBE system for NW growth. In the GS-MBE system, group-III species (In) are supplied from a heated solid elemental effusion source, and the group-V species are supplied as dimers (P_2) from a hydride (PH_3) gas cracker operating at 950 °C. Prior to growth, the substrate was heated to the growth temperature of 465 °C and subjected to a 5-minute hydrogen plasma treatment under P_2 overpressure for oxide removal. Under these conditions, the Au deposit evolves into self-assembled Au nanoparticles suitable for VLS growth as reported previously [4.7]. NW growth was then initiated by opening the shutter to the In effusion cell, which was preheated to give a nominal 2-D growth rate of 1 μm/hr at a V/III flux ratio of 2. After 10 minutes the In shutter was closed, terminating the growth. This growth was labeled growth #219.

After growth, the morphology of the resulting NWs was observed using a JEOL JSM-7000F scanning electron microscope (SEM) in the secondary electron imaging mode. The diameter and height of the NWs were obtained directly from the SEM images. During NW growth, there is a simultaneous 2-D growth on the non-activated surface (i.e. those areas not covered by Au particles). The reported heights represent the portion of the NWs visible above this 2-D layer and include any correction necessary to account for sample tilt during the SEM imaging. SEM samples were prepared by fixing a small piece (~0.5 cm^2) of the as-grown material to a SEM mounting stub with a small amount of silver paint at each corner.

A Philips CM-12 transmission electron microscope (TEM) in bright field mode was used to observe the defect structure of the NWs. NW samples for TEM analysis were prepared by sonicating small pieces of the as-grown material in methanol solution for 1 to 2 minutes to break the NWs near their base. A small volume (~50 μL) of the methanol solution was placed onto a holey carbon TEM support grid and allowed to evaporate. After methanol evaporation the NWs remained fixed to the grid.

4.3 InP Nanowire Morphology

4.3.1 SEM Analysis of InP Nanowires

Plan-view (Figure 4.1a) and 60-degree tilted (Figure 4.1c) SEM images reveal that GS-MBE growth results in rod-shaped NWs oriented in the (111)B direction, orthogonal to the substrate surface. Au is evident at the top of the NWs, confirming that the NWs grew by a catalytic process. The NW diameters, defined by the initial size distribution of the Au nanoparticles, ranged from 20 to 700 nm, consistent with earlier results for GaAs NWs [4.7]. The height of the NWs was measured, and plotted as a function of the catalyst diameter in Figure 4.2. The NW height is inversely proportional to the NW diameter as observed previously for GaAs NWs [4.7]. This well-known dependence of NW height on diameter confirms that growth is driven by diffusion of adatoms from the base to the tip of the NWs according to the VLS process [4.8, 9].

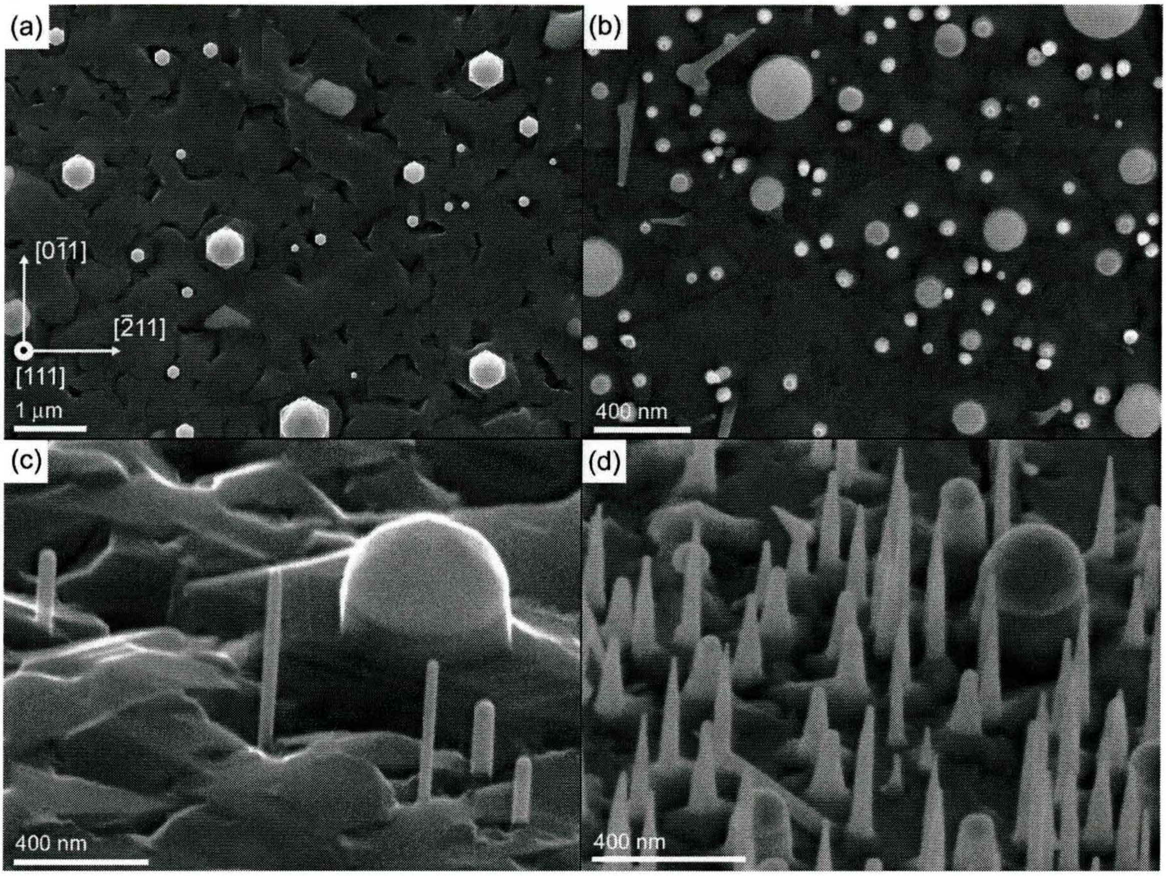

Figure 4.1. SEM images of InP NWs as compared to GaAs NWs: (a) plan-view InP wires, (b) plan-view GaAs wires, (c) 60-degree tilted InP wires, and (d) 45-degree tilted GaAs wires. Note the differences in magnification. The crystal orientation indicated in (a) also applies to (b). InP NWs were grown at 465 °C, and GaAs NWs were grown at 550 °C.

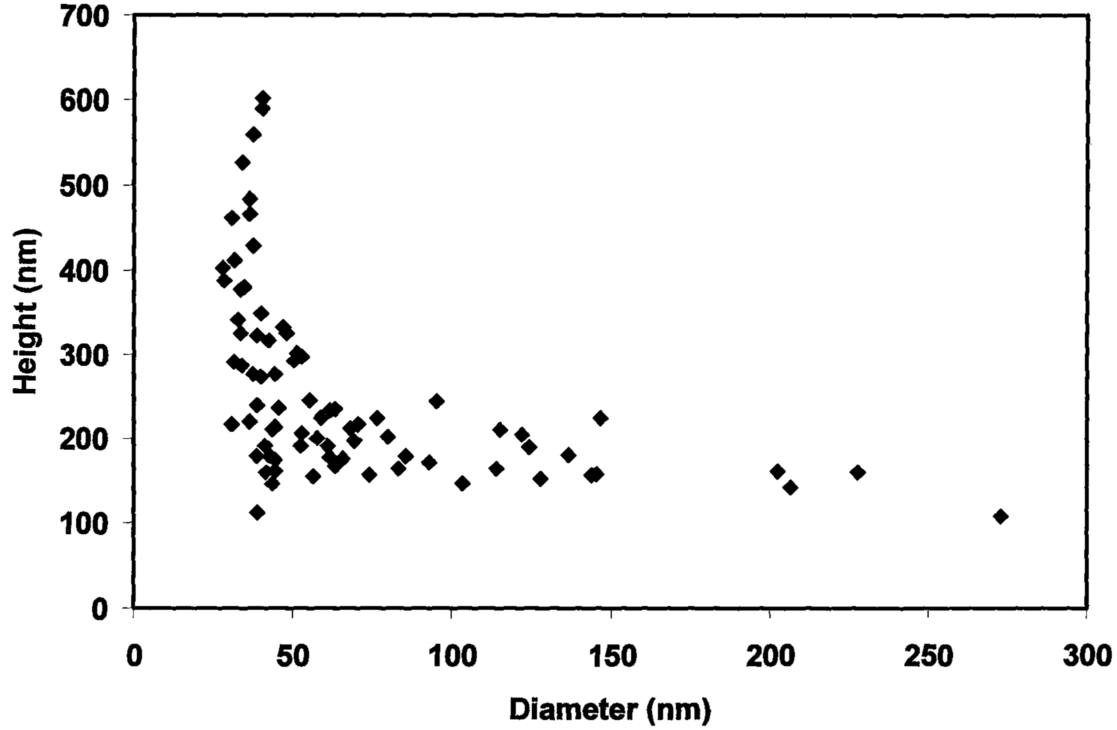

Figure 4.2. InP NW height and diameter data. The characteristic inverse proportionality supports growth by diffusion of adatoms from the base to the tip of the wire.

4.3.2 InP versus GaAs NW Morphology

The InP NWs were compared to GaAs NWs with the same (111)B substrate orientation, surface preparation, and growth conditions. The SEM images shown in Figure 4.1 highlight some of the morphological differences between NW growth in the InP and GaAs material systems: (1) the areal density of the InP NWs is much smaller than that of the GaAs NWs; (2) the number of thin wires is much greater in the GaAs system while the number of thick wires is greater in the InP system; (3) the sidewalls of the InP wires are oriented along the {-211} family of planes for all wire sizes, whereas the GaAs sidewall facets are difficult to identify, resulting in a more rounded cross-section; (4) the shape of the InP wires is rod-like with uniform diameter, whereas the GaAs wires are typically tapered.

To quantify the differences in particle density and size between InP and GaAs NWs (observations 1 and 2 from above), an image analysis program (ImageJ [4.10]) was implemented to measure the area of the particles from a number of plan-view images. Due to the fluctuating contrast caused by the irregularities on the sample surface, and some noise in the image, it was not practical to allow the software to process the images directly. Instead, a mask of each of the images was generated manually in Adobe Photoshop Elements [4.11] to highlight the wire tips and eliminate image noise. The resulting images were then processed in the ImageJ software, which measured the plan-view area of each of the particles, allowing for a calculation of the particle diameter. Since most of the particles analyzed were either round, slightly elliptical, or hexagonal, it was reasonable to assume a circular shape when calculating the diameter of the wires from the area measurement. A histogram was plotted to quantify the NW diameter frequency distribution for each material system (Figure 4.3), including a surface density value calculated by dividing the total wire count by the total area of the images analyzed. Also included in Figure 4.3 are estimates of the integrated volume of all of the Au particles (treated as hemispheres defined by the calculated particle diameter), the volume of the deposited Au film, and the ratio of these two parameters. Figure 4.3 provides quantitative support to statements 1 and 2 above.

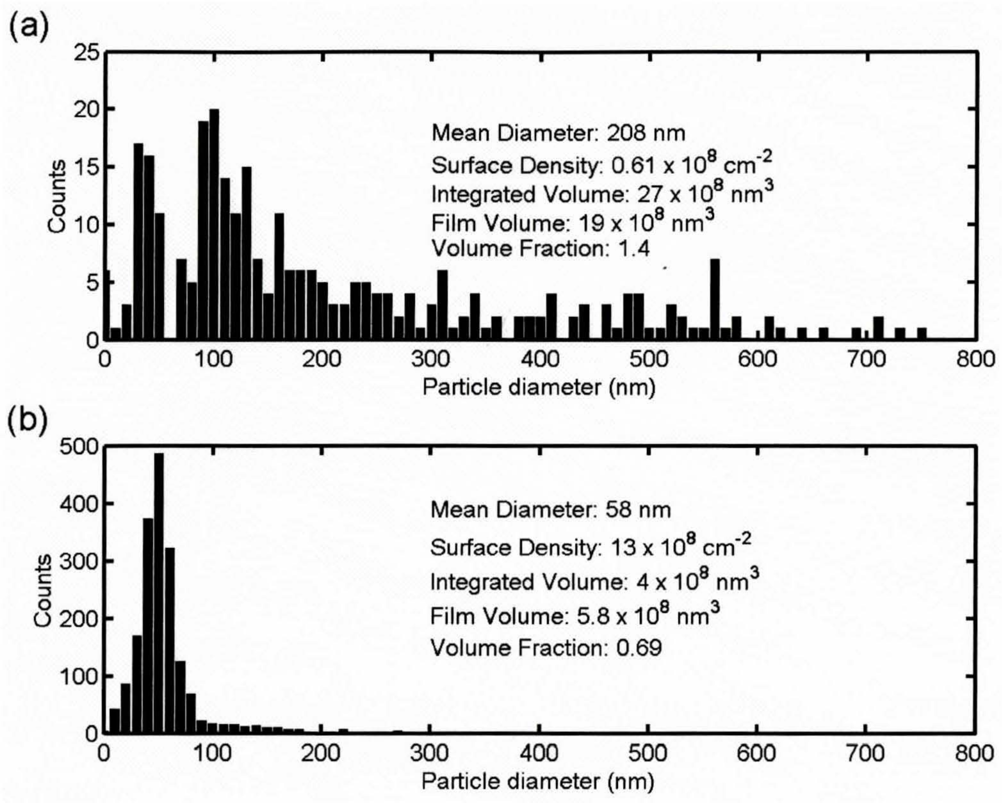

Figure 4.3. Diameter distributions, surface densities, and estimated Au volume data from SEM images at 15,000 times magnification for (a) InP NWs and (b) GaAs wires. Note the differences in the vertical scales. The bin size was chosen as 10 nm.

It is quite clear from Figure 4.3 that the GaAs NWs are much more densely packed than the InP NWs with a diameter centered around 50 nm. The range of sizes available to the InP NWs is much greater, with the highest frequency residing around 100 nm. The distribution gradually trails off to higher diameters, with significant counts for particles as large as 600 nm. As shown in Figure 4.3, the mean diameter of the InP wires is almost 4 times larger than that of the GaAs NWs.

The integrated Au particle volume of the InP NWs is about 40% larger than the initial film volume. This is likely due to the fact that the Au particles are not quite as large as hemispheres defined by their radii, but are better described by a more flattened shape (i.e. the Au-wire contact angle is less than 90°). This will become clear in later discussions (Figure 4.6). The integrated Au volume of the GaAs NWs is ~70 % of the film volume, underestimating the amount of Au on the sample surface. Previous work in the GaAs material system has shown that Au can become embedded in the 2D film growth that takes place on the surface (Figure 4.4). This effect is not well understood, but may be the reason for the underestimation of the Au volume in the GaAs NW analysis.

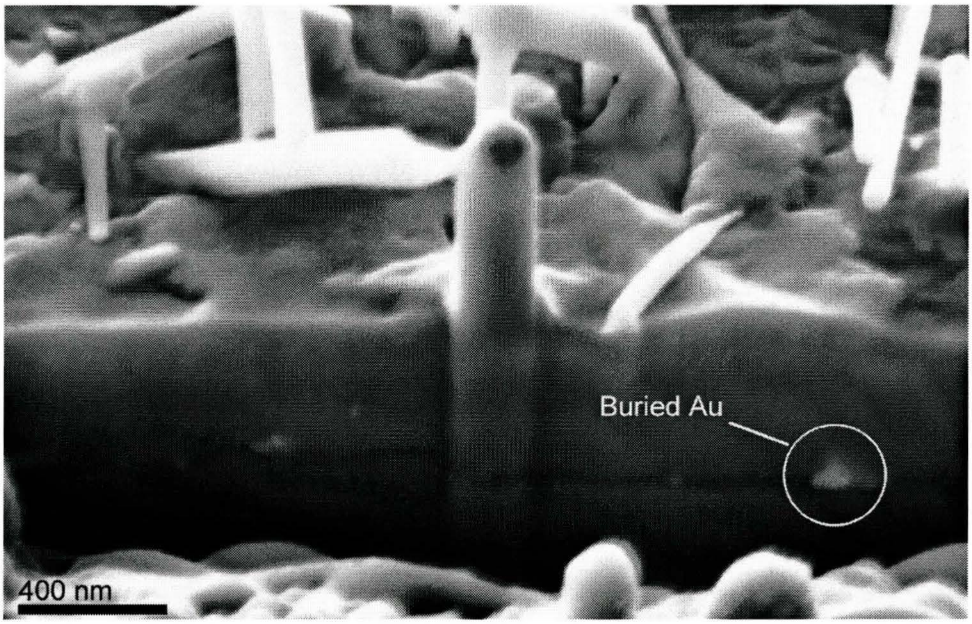

Figure 4.4. SEM image of GaAs NW sample surface cut by focused ion beam. Buried gold is visible as bright spots in the 2D growth that encases the cross-sectioned NW.

We now turn our attention to observations (3) and (4) mentioned above. The alignment of the InP NW sidewall facets with the {-211} family of crystal planes is clearly evident in Figure 4.1a and further magnified in Figure 4.5. In a previous GaAs

NW study [4.7], where the GaAs wires were grown cooler (500 °C) and for a longer (growth time = 30 min), the sidewall facet orientation was noticed to change from {-211}-type to {0-11}-type crystal planes as material was deposited on the sidewalls of the NWs over the 30-minute growth period.

The adatom diffusion length of In in the present growths is known to be greater than that of Ga [4.12, 13]. As a result, In adatoms are expected to diffuse to the top of the NWs with negligible sidewall deposition, even at the temperature of 465 °C used in this work. This is confirmed by the SEM images where rod-shaped NWs with clear {-211} sidewalls are evident. Conversely, the GaAs NWs show a strongly tapered morphology due to sidewall deposition. This difference in the ability of In and Ga adatoms to diffuse to the wire tip influences the composition and morphology of the InGaAs/InP heterostructure NWs as will be further explored in the next chapter.

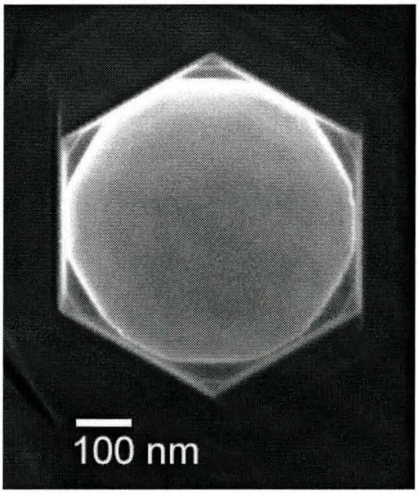

Figure 4.5. Magnified plan-view InP NW. The hexagonal shape of the NW is clear, as well as the inability of the Au particle to conform to the wire cross-section.

As a final interesting point regarding the Au particles on the InP NWs, we note that the Au does not conform to the hexagonal NW cross-section. It appears that the particle pulls away from the edges to take on a more circular shape. This circular shape is a lower energy form than that which would be required to cover the hexagonal shape of the wire tip.

4.4 InP-Au Particles versus GaAs-Au Particles

To further investigate differences in the surface density and catalyst diameter between GaAs and InP NWs an analysis of annealed, Au-covered substrates was conducted. To produce samples for this study, InP and GaAs (111)B substrates were submitted to a 20-minute UV ozone treatment, etched in 10% buffered HF for 30 seconds, metallized with 4 nm of Au, then annealed for 5 minutes in a rapid thermal annealer (RTA) at the InP NW growth temperature of 460 °C. The same procedure was repeated with an annealing temperature of 550 °C, the GaAs NW growth temperature. Samples were capped with the matching substrate material to mitigate the effect of surface degradation due to heating in the absence of a stabilizing group-V flux. The goal of this experiment was to simulate the Au particle self-assembly process on InP and GaAs (111)B surfaces. Images typical of this annealing experiment are shown in Figure 4.6 and Figure 4.7.

These images demonstrate the higher density of particles on the GaAs substrate as compared to the InP substrate. Note also the propensity for larger particles on the InP surface compared to the GaAs surface and that the number of very small particles appears much greater on the GaAs surfaces, consistent with observations (1) and (2) from Figure

4.1. These differences between the Au particle distributions on the two material systems are similar to the measured differences between InP and GaAs NW diameters (Figure 4.3) showing how the Au particle size influences NW size and distribution. Note also that the particles in Figure 4.6a often take on a six-sided form, aligned with the {-211} planes as in the InP NWs of Figure 4.1a. As observed in Figure 4.5, many of the Au particles on the surface of Figure 4.6a seem to have pulled away from the six-sided base to form more rounded shapes. Due to the lack of frequency with which these irregular shapes are observed in the NW growth it is possible that this pulling away occurs during the cooling phase. Further annealing experiments in the GS-MBE chamber can be carried out to explore this possibility.

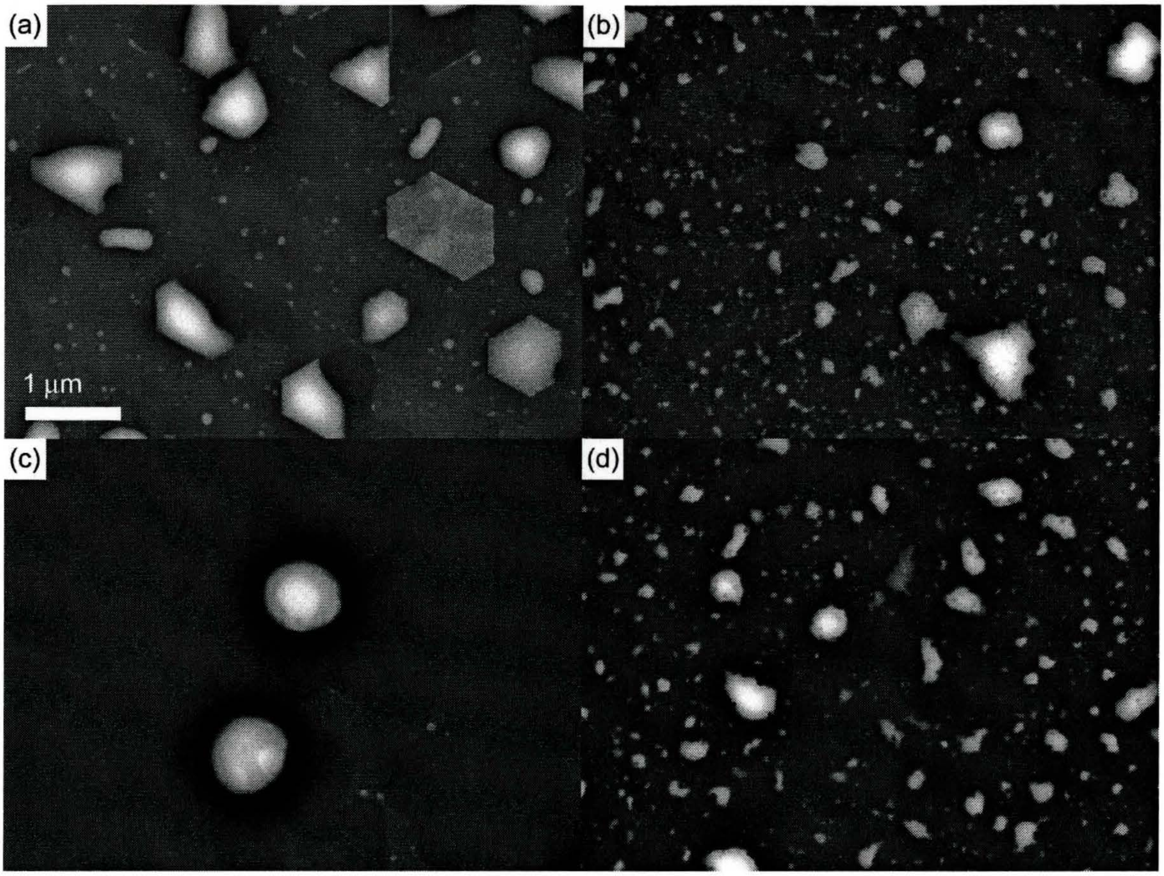

Figure 4.6. SEM backscattered electron images of annealed, Au covered surfaces: (a) InP annealed at 460 °C, (b) GaAs annealed at 460 °C, (c) InP annealed at 550 °C, and (d) GaAs annealed at 550 °C. The 1 μm scale bar from (a) applies to all 4 images.

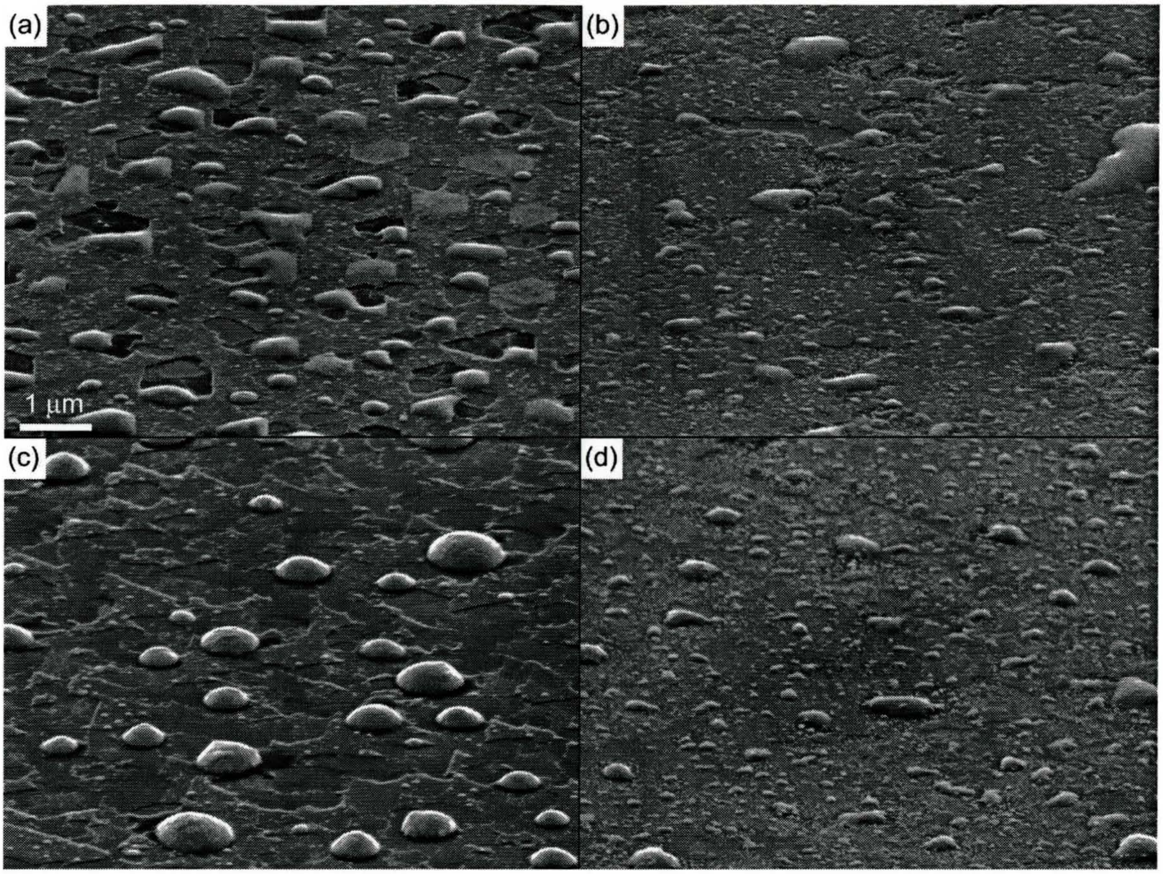

Figure 4.7. 65-degree tilted SEM images of annealed surfaces: (a) InP annealed at 460 °C, (b) GaAs annealed at 460 °C, (c) InP annealed at 550 °C, and (d) GaAs annealed at 550 °C. The 1 μm scale bar from (a) applies to all 4 images.

To further quantify these observations, the size and distribution of the Au particles on the annealed surfaces were analyzed using a process similar to that used to quantify the NW results. However, the plan-view images shown in Figure 4.6 were produced using the backscattered electron imaging mode of the SEM instead of the secondary electron imaging mode. The reason for this change in imaging mode is elucidated in Figure 4.8, which shows a comparison between a secondary electron image and a backscattered electron image from the same sample surface. Analysis of images such as Figure 4.8a in ImageJ is unreliable, even with use of the manual particle selection process used to produce the results in Figure 4.3, since it is difficult to identify contrast due to Au particles. Imaging via backscattered electrons creates greater contrast between different chemical elements (higher z-contrast) than secondary electron imaging [4.14], and produces much cleaner images, suitable for analysis in ImageJ. Images of the four annealed sample surfaces were then analyzed using the Photoshop and ImageJ process described above.

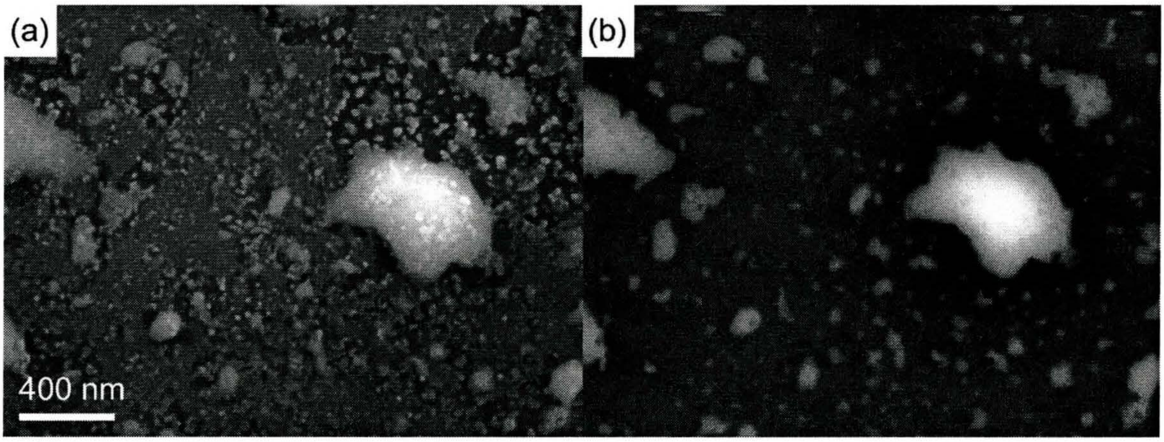

Figure 4.8. SEM images of GaAs sample annealed at 460 °C and imaged in (a) Secondary Electron Mode, and (b) Backscattered Electron Mode.

As in Figure 4.3, the parameters analyzed were the mean particle diameter, the areal density, and the integrated particle volume as a fraction of the 4 nm film volume. To calculate the integrated volume the shape of each particle was approximated by a hemisphere defined by the calculated diameter from the image analysis data. The results of this analysis are shown in Figure 4.9 and are discussed below in terms of the effect of changes to the annealing temperature and substrate material.

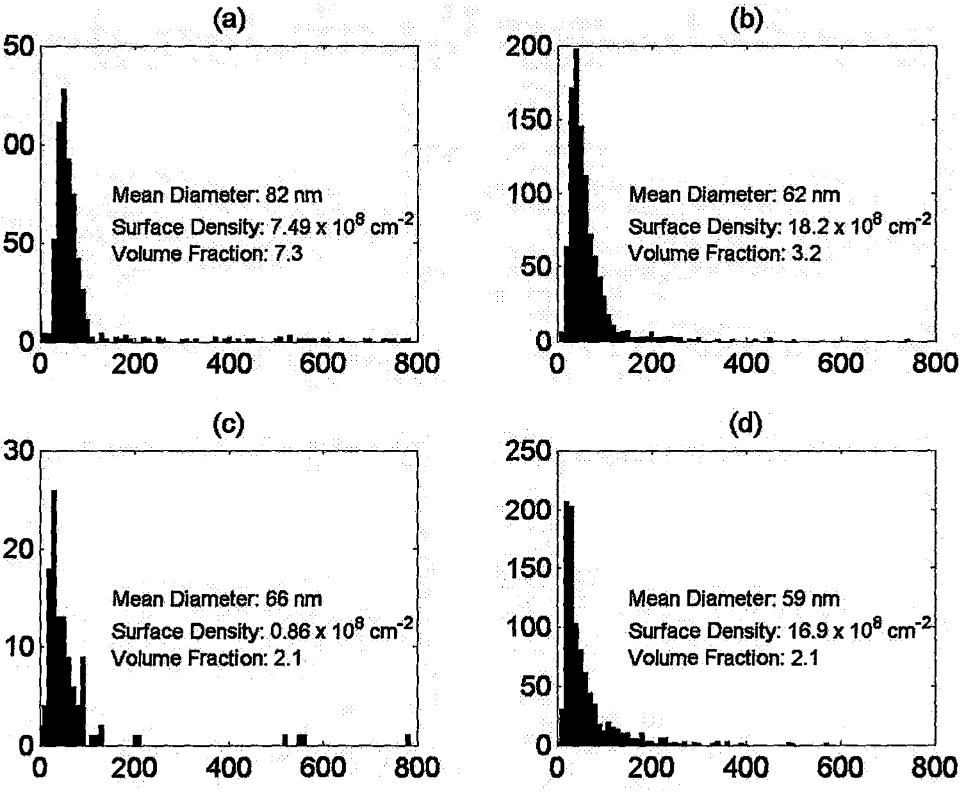

Figure 4.9. Diameter distributions, surface densities, and estimated Au volume data for annealed surfaces: (a) InP annealed at 460 °C, (b) GaAs annealed at 460 °C, (c) InP annealed at 550 °C, and (d) GaAs annealed at 550 °C. Particle diameter is shown on the horizontal axis and the counts are shown on the vertical axis.

4.4.1 Annealing Temperature

As described above, Au covered substrates of both InP and GaAs were annealed at the NW growth temperatures of 460 °C and 550 °C. This experiment offered the opportunity to explore the Au behaviour on a given material as a function of temperature. Figure 4.9 shows that the surface density decreases when the temperature is increased, as observed in a previous GaAs NW temperature study [4.7]. This means that the Au particles on the surface have a tendency to coalesce, forming larger particles and reducing the total particle count. However, the data of Figure 4.9 indicate that the mean particle diameter decreases with increasing temperature, which is unexpected if the Au volume is to be conserved. The change in shape of the Au particles on the high temperature surface (especially on InP) can explain this apparent discrepancy. As identified above in Figure 4.6a, the large Au particles on the low-temperature InP surface tend to form large, thin, six-sided plates. The tilted SEM image of this surface shown in Figure 4.7a confirms that the particles often form thin plates on the InP surface at 460 °C. These particles have a large plan-view area and, as such, cause a large overestimation of the integrated Au volume when using the hemispherical particle approximation in Figure 4.9a. In comparing Figure 4.6a and Figure 4.6c it is clear that the Au particles on the InP surface become much more circular and have a smaller maximum plan-view area at the higher annealing temperature, resulting in a smaller calculated mean diameter. Note also that the high-temperature particles show much better agreement with the hemispherical model used to calculate the integrated Au volume in Figure 4.9c. Figure 4.7c confirms that the particles seem to 'ball-up' on the InP surface at the higher annealing temperature, taking a more hemispherical form. Although less pronounced, this effect is also observed in the GaAs material system (Figure 4.7b versus Figure 4.7d).

4.4.2 Substrate Material: InP versus GaAs (111)B Surfaces

Of particular interest to the study of InP and GaAs NW growth is a comparison of the Au particle self-assembly process on these two material surfaces. By changing the material system from InP to GaAs Figure 4.9 shows that the mean diameter decreases and the surface density increases. This is consistent with observations made in the comparison of InP to GaAs NWs (Figure 4.3), providing evidence that the differences in the wire diameter and density are related to the differences in the way that the Au particles distribute on the two different substrate material surfaces during the 5-minute pre-anneal phase of NW growth. The exact parameter values, however, do not match, and the NW growth surfaces of Figure 4.1 are visually very different from the corresponding annealed surfaces (Figure 4.6a and Figure 4.6d). The surface annealing that takes place prior to NW growth in the MBE chamber has some important differences with the process that takes place in the RTA. First, the MBE system is operated at ultra-high vacuum pressures, whereas the RTA operates at atmospheric pressure in a nitrogen-purged environment. Secondly, the MBE annealing is performed under a hydrogen plasma to remove the surface oxides while the surface is stabilized with a group-V flux, a treatment not available in the RTA. The rough surfaces characteristic of the annealing experiment (Figure 4.8) might be due to the lack of a stabilizing group-V flux to prevent surface degradation. As noted above, the samples were capped with the matching substrate material but this may have been insufficient to prevent degradation of the surfaces.

A more appropriate comparison can be made between NWs and surfaces annealed in the MBE chamber, a study that will be conducted in future work. However, as described above, the differences observed in the particle distributions between the InP and GaAs annealed surfaces and the corresponding NW growths do show the same trends, demonstrating the influence of the substrate material choice on the Au self-assembly process and the subsequent NW growth.

4.5 Stacking Faults in InP Nanowires

TEM observations were conducted for InP NWs of varying length, as shown in Figure 4.10. Stacking faults, visible as dark bands, are evident in the long NWs such as those shown in Figure 4.10(b) and (c). This is the result of rotational twins, due to an alternation between ZB and W crystal structures, as described elsewhere [4.1, 15]. This high concentration of stacking faults is common in (111)B oriented NWs grown by MOVPE [4.1, 2, 4]. However, unlike these earlier studies, the GS-MBE-grown InP NWs presented here reveal no stacking faults for NW lengths below about 300 nm, such as that shown in Figure 4.10(a). Furthermore, it is found that stacking faults are only present in longer NWs (grown from smaller Au catalysts) and that these faults are concentrated at the wire tips near the Au catalyst, as shown in Figure 4.10(b) and (c). None of the wires examined showed faults near the base. This was true regardless of the viewing direction, which is known to influence the visibility of faults [4.15].

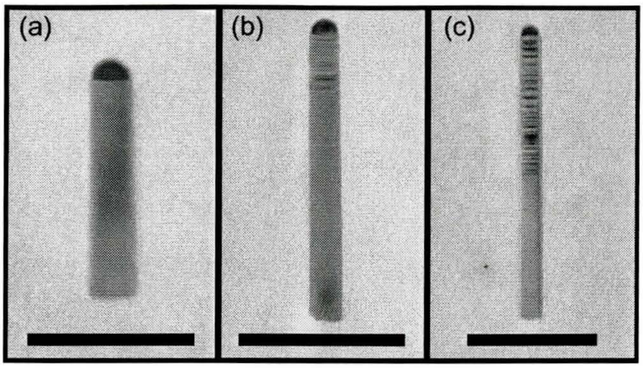

Figure 4.10. TEM images of InP NWs of different length. The scale bars represent 200 nm in each image.

These results indicate that there is a transitional wire height at which the crystal structure becomes disrupted and the formation of stacking faults becomes frequent. An empirical potential approach has shown that the energy difference between W and ZB structures is very small for III-V NWs [4.6]. For bulk InP, this energy difference is only 3.4 meV/atom, decreasing and becoming negative as the NW diameter approaches ~20 nm. Given this small energy difference between the two structures, the observed bistability of NWs is not surprising. Soshnikov et al. [4.16] suggested that this bistability may be driven by a quasi-periodic fluctuation in supersaturation of the Au particle due to the effective filling of the growing adatom layer. Hiruma et al. [4.17], for example, showed in their early work on InAs and GaAs NWs grown by MOVPE that either the ZB or W crystal structure could be favored, depending on growth conditions (temperature and V/III flux ratio). Similarly, previous studies of CdTe grown by colloidal methods [4.18] showed that the polytypism of ZB and W was related to the level of supersaturation, with high levels of supersaturation favoring ZB and low levels favoring W. In the case of InP NW growth by GS-MBE, adatom supersaturation of the Au particle relies on diffusion of adatoms from the base to the tip of the NW. It is plausible that as the NW height increases, the supersaturation diminishes, leading to a change from metastable to bistable conditions (i.e., the introduction of stacking faults). In a previous study on the growth of GaAsP/GaP heterostructure NWs grown by GS-MBE, it was noted that NWs with diameters below 20 nm exhibited no stacking faults at all [4.19]. This is consistent with previous empirical potential models that show the energy difference between ZB and W increases for NW diameters below 20 nm, in favor of the W structure [4.6]. However, for NWs with diameters greater than 20 nm, it was noted that the GaAsP segment contained a large density of stacking faults, while the GaP segment showed very few or no stacking faults. It is interesting to note that in the case of GaAs/GaP growth by MOVPE, a trend opposite to this has been observed: that is, GaP exhibited a large stacking fault density while GaAs showed none [4.20]. It is clear from this discussion that further elaborate growth models are necessary to predict the structural stabilities in III-V NWs.

4.6 Chapter Summary

InP NWs were grown by gas source molecular beam epitaxy on InP (111)B substrates, using Au nanoparticles as a growth catalyst. These structures were characterized by the analysis of SEM and TEM images. The rod-shaped NWs exhibited hexagonal sidewall facets oriented along the {-211} family of crystal planes for all NW diameters, indicating minimal sidewall growth. Stacking faults, when present, were concentrated near the NW tips, and NWs with lengths of less than 300 nm were completely free of stacking faults. Above this length, it appears that the changing supersaturation conditions of the Au particle introduce a bistability in the crystal structure, which depends on growth method (GS-MBE versus MOVPE), III-V composition (As- versus P-containing alloys), and growth conditions (temperature and V/III flux ratio). Compared to GaAs NWs, InP NWs were found to have a larger mean diameter and a lower areal density than GaAs NWs grown by the same method. An analysis of the Au particle distributions on both InP and GaAs (111)B substrates and under different annealing temperatures confirms that the differences between InP and GaAs Au particle distributions are reflected in NW diameter distributions. These differences, in particular the longer In adatom surface diffusion length, are important in the analysis of InGaAs/InP heterostructure NWs.

5 InGaAs/InP Core-Shell and Axial Heterostructure Nanowires

5.1 Introduction

NW devices to date have been mostly limited to simple material systems such as Si, or binary III-V semiconductors such as GaAs and InP. However, functional NW devices will only be fully realized by their extension into more complex material systems that include multiple group-III (e.g., Al, In, Ga) and/or group-V elements (P, As, Sb). Few studies exist for NWs in ternary compound material systems that are of interest in long wavelength optoelectronic devices, such as InGaAs [5.1, 2]. In this chapter, we report the growth and compositional analysis of InGaAs/InP heterostructure NWs.

In this study InGaAs/InP heterostructure nanowires (NWs) were grown by gas source molecular beam epitaxy on InP (111)B substrates using self-assembled Au particles as a growth catalyst. These structures were analyzed by scanning electron microscopy (SEM), high-resolution transmission electron microscopy (HR-TEM), and energy-dispersive x-ray spectroscopy (EDS). The material interfaces showed significant transition regions and a distinct bulging morphology, attributed to transient group-III material in the Au catalyst. Sidewall growth of InGaAs on InP and a deficiency of Ga in the InGaAs section were observed, and occur due to the shorter surface diffusion length of Ga adatoms compared to In.

5.2 Experimental Details

The NWs studied in this work were grown on (111)B *n*-type InP seeded with Au nanoparticles. The as-received Epi-Ready substrate was first submitted to a 20-minute UV-ozone treatment to remove any contamination from hydrocarbons and grow a sacrificial layer of oxide. After etching in a 10% buffered HF solution for 30 seconds and rinsing with deionized water, the sample was transported in ambient air to an e-beam evaporation system (base pressure better than 10^{-8} Torr), where a 1 nm-thick film of Au was deposited at room temperature and at an average rate of 0.1 nm/sec as monitored by a quartz crystal monitor. The substrate with Au deposit was then transferred in ambient air to the gas source molecular beam epitaxy (GS-MBE) growth chamber where the substrate temperature was ramped to the target growth temperature of 460 °C under a P_2 flux. These conditions allow a spontaneous reordering of the Au film into Au nanoparticles. Simultaneous desorption of native oxide was enhanced by the use of a hydrogen inductively coupled plasma source. After oxide removal and Au nanoparticle formation, the In shutter was opened to initiate the NW growth.

The NWs consisted of an initial InP segment, an InGaAs middle segment, and a terminating InP segment. In GS-MBE, the group-V constituents are supplied primarily in the form of As_2 and P_2 from the pyrolysis of AsH_3 and PH_3 in a dual filament cracker operating at 950 °C. Throughout growth the In flux rate remained constant, corresponding to a nominal 2D InP growth rate of 1 μm/hr with a V/III flux ratio of 2. Growth of the InGaAs layer was initiated by opening both the Ga and In shutters, giving a total growth rate of 1.88 μm/hr with a V/III flux ratio of 1.25. Group-III flux values were selected to achieve a lattice-matched $In_{0.53}Ga_{0.47}As$ composition as determined by earlier thin-film calibration growths. Switching of the molecular beams at the InGaAs-on-InP interface occurred by first shuttering the In beam to terminate growth of the InP segment, initiating AsH_3 flow, terminating PH_3 flow, waiting 30 seconds, and then opening the In and Ga shutters to initiate growth of the InGaAs layer. Similarly, molecular beam switching at the InP-on-InGaAs interface occurred by first shuttering the In and Ga beams to terminate growth of the InGaAs layer, initiating the PH_3 flow, terminating the AsH_3 flow, waiting 30 seconds, then reopening the In shutter. Growth times were 10, 1.06, and 2 minutes for the initial InP segment, the InGaAs segment, and the final InP segment, respectively. The growth number for this sample was #328.

After growth, the sample was characterized by scanning electron microscopy (SEM) using a JEOL JSM-7000F microscope set to image secondary electron emission. For further analysis by bright-field transmission electron microscopy (TEM), the NWs were removed from the InP substrate by sonicating in methanol solution for 1-2 minutes. A small volume (~50 μL) of the methanol solution was placed onto a holey carbon TEM support grid. After methanol evaporation, NWs were found to be dispersed onto the grid as observed by a JEOL 2010F high-resolution TEM (HR-TEM). To extract further compositional information energy dispersive x-ray spectroscopy (EDS) measurements were made with the TEM in scanning mode, using a probe size less than 1 nm, and measuring the In $L\alpha_1$, Ga $K\alpha_1$, As $K\alpha_1$, P $K\alpha_1$, and Au $L\alpha_1$ x-ray transitions. In this manner, the abruptness of the InGaAs/InP NW heterointerfaces and the elemental distributions throughout the NWs were investigated. Axial scans along the NW centre were performed to gather information on the interface abruptness and layer composition, while radial scans gave insight into composition variation across the wire with particular attention to sidewall growth. Point measurements were taken to quantify the composition at various locations along the wire.

5.3 Results and Discussion

60–degree tilted (Figure 5.1a) and plan-view (Figure 5.1b) SEM images reveal NWs oriented in the (111)B direction, orthogonal to the substrate surface. Au is evident at the top of the NWs, confirming that the NWs grew from the seed particles. The NW diameters ranged from 20 to 250 nm, as defined by the initial size distribution of the Au nanoparticles, and the height of the NWs ranged from 40 to 350 nm. Due to the thin Au film (1 nm) used in this growth, the maximum particle diameter is smaller than observed in earlier studies of GaAs and InP NWs grown using a 4 nm Au film [5.3, 4]. Faceting of the wire sidewalls with the {-211} family of crystal planes was usually observed as in Figure 5.1b, consistent with earlier observations for InP wires [5.4].

The InGaAs/InP wires grown by GS-MBE in this study revealed an unusual morphology with a prominent bulge near the wire middle followed by a slight reduction in wire diameter (Figure 5.1c). Slight kinking of the wires near the bulge was occasionally observed as illustrated in Figure 5.1a. Neither GaAsP/GaP heterostructure NWs nor binary (GaAs and InP) wires, grown in the same GS-MBE system, showed any bulges along their length [5.3-5]. Heterostructure NWs grown by metal-organic vapor-phase epitaxy (MOVPE) were also free of this bulging morphology [5.6-8]. As will be elaborated below, the bulging can be related to the effect of the group-III material transition in the GS-MBE system. The NW kinking is probably due to the influence of elastic strain energy introduced by the lattice mismatch between the InP and InGaAs segments. Although grown nominally lattice-matched, EDS measurements (discussed below) indicated a composition of $In_{0.74}Ga_{0.26}As$, resulting in a lattice mismatch of 1.4% relative to InP. GaAs NWs have been observed to grow along the [110] direction rather than the usual [111] direction due to the strain energy induced by proximity effects of neighboring NWs [5.9]. For similar reasons, compressively strained InAs NWs on GaAs substrates have been observed to grow along the [100] direction [5.10].

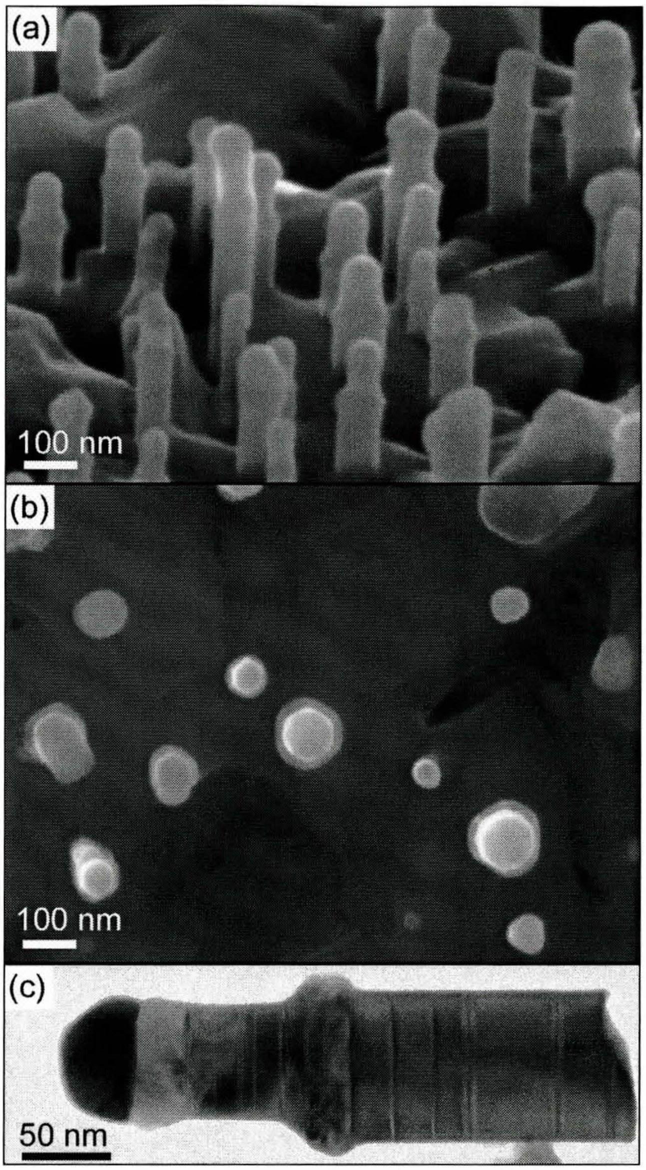

Figure 5.1. (a) 60-degree tilted SEM, (b) plan-view SEM, and (c) TEM images of InGaAs/InP heterostructure NWs.

To further examine the nature of the wire morphology and heterostructure interfaces, an EDS linescan was made along the centre axis of the wire shown in Figure 5.1c. Figure 5.2 shows these measurements along with corresponding TEM images. Several distinct growth regions were identified as labeled in the figure: (1) an InP base (far right portion of Figure 5.2b) with a diameter somewhat larger than the Au particle; (2) a transition region from the InP to the middle InGaAs segment in which a pronounced bulge disrupts the uniformity of the growth; (3) the InGaAs middle segment with about the same diameter as the Au particle; (4) a slight bulge immediately below the Au particle representing a transition region from the InGaAs segment to the final InP segment; (5) the terminating InP segment; and (6) the Au particle alloy (far left portion of Figure 5.2a). Each region is described in further detail below.

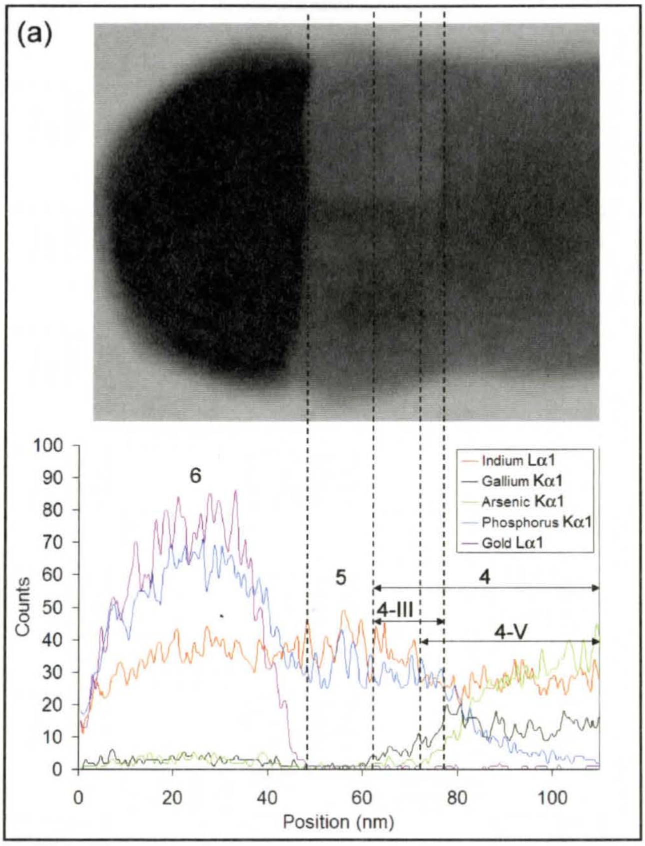

Figure 5.2. Axial EDS linescan of the InGaAs/InP heterostructure NW from Figure 5.1c, showing the 6 regions of interest as described in the text. The figure is split into two sections to aid visual clarity. The corresponding TEM image is aligned above the EDS results.

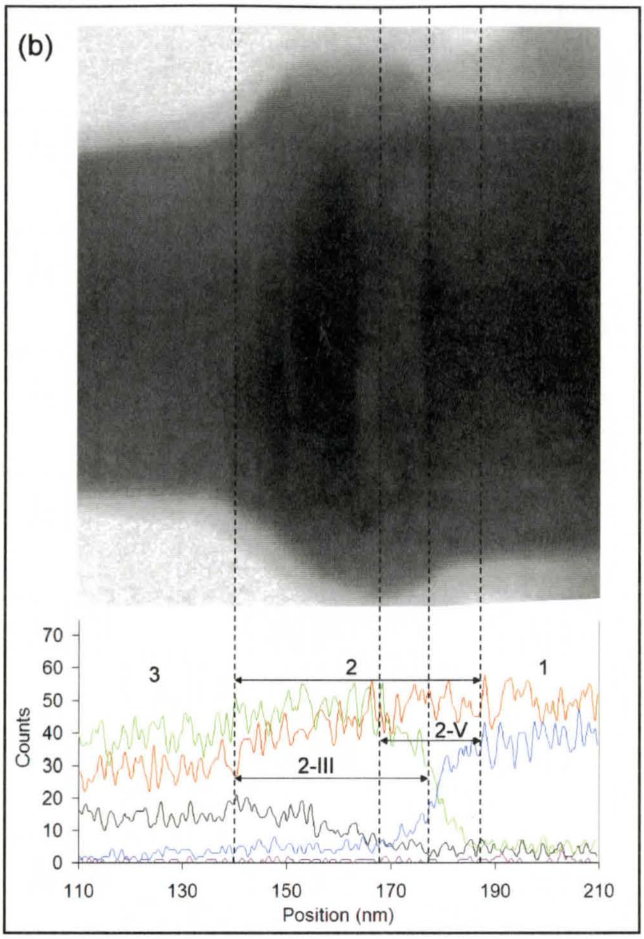

Figure 5.2 (continued)

5.3.1 Au Alloy Particle

First, we examine the EDS results for the Au particle (region 6 in Figure 5.2a). NW growth was completed by shuttering the group-III (In) source and cooling the sample under a group-V flux (P_2). The EDS linescans of Figure 5.2a suggest that both In and P remain in the Au particle after growth of the final InP segment. However, care is needed in the interpretation of the linescan results. The observation of significant group-V content in the Au particle is unexpected since it appears that group-V elements are not soluble in Au from phase diagram considerations and as confirmed by analysis of NWs grown by MOVPE and chemical beam epitaxy (CBE) methods [5.11, 12]. Indeed, EDS point measurements of the Au particle revealed a binary alloy of 46 atomic percent In and 54 atomic percent Au, close to the AuIn phase. Interestingly, if the AuIn alloy phase also persists during growth, then a solid phase NW growth mechanism may be occurring (AuIn alloy is solid at the growth temperature of 460 °C) [5.13], contrary to the case of GaAsP/GaP NWs in which there is evidence that the Au particle enters the liquid phase during growth [5.5]. The discrepancy between the linescan and point EDS measurements can be attributed to the method by which the INCA software [5.14] correlates x-ray counts. Point measurements involve a full deconvolution of overlapping peaks, while linescans collect counts based on a simple energy spectrum window, making the linescan measurement susceptible to confusion of the partially overlapping Au and P x-ray emission peaks (P $K\alpha_1 = 2.014$ keV and Au $M\alpha_1 = 2.123$ keV). This suggests that NW growth occurs by bulk diffusion of group-III elements in the Au particle, while group-V elements, being insoluble in Au, may only diffuse to the growth front via the Au-wire interface. The consequences of these different growth mechanisms on interface abruptness are now discussed.

5.3.2 InP-to-InGaAs Transition

The InP base region of the NW is identified as region 1 in the EDS linescan of Figure 5.2b. In addition to In and P, Ga and As are also present in region 1, which will be explained later in terms of InGaAs sidewall growth. As described above, switching of the molecular beams at the interface occurred by first shuttering the In beam to terminate growth of the InP segment, initiating AsH_3 flow, terminating PH_3 flow, waiting 30 seconds, and then opening the In and Ga shutters to initiate growth of the InGaAs segment. When applied to 2D growth, this gas-switching sequence results in an abrupt group-III transition and an interface consisting of a few monolayers of InGaAsP (~ 1 nm thick), due primarily to exchange of P with As during the growth interruption [5.15]. In the case of NWs, it is evident from the EDS measurements in Figure 5.2b that the transition zone (region 2) is much wider than the 2D analogue, demonstrating the retarding effect of the Au catalyst on changes to the material (group-III) supply. Region 2 contains two overlapping transitions, and begins with initiation of a group-V transition, resulting in a graded InAsP composition (InP to InAs). This group-V transition (region 2-V) is ~20 nm thick with relatively small changes in the group-III profile. The group-III transition (region 2-III) is spread across the latter ~37 nm of region 2 and comprises a graded InGaAs composition with relatively little change in the group-V profile. Note that the slight decline in the As signal within region 2-III may be attributed to the decreasing wire diameter associated with the bulge morphology discussed below.

Assuming a nominal $In_{0.53}Ga_{0.47}As$ composition, the Ga concentration is expected to rise from 0 atomic percent in the InP segment to 24 atomic percent in the InGaAs segment (region 3), while the In concentration is expected to decline from 50 to 27 atomic percent. However, EDS point measurements in the InGaAs region (region 3) of a similar wire indicated a Ga content of only 13 to 17 atomic percent. This Ga deficiency can be explained based on differences in the adatom diffusion lengths of In and Ga.

Since In adatoms have a longer diffusion length [5.1, 16] they can migrate along the NW sidewalls and deposit at the growth interface to a greater extent than Ga adatoms, resulting in the observed Ga deficiency in the InGaAs section of the heterostructure NWs studied here.

The bulging of region 2 is a conspicuous morphological feature of our wires. During VLS growth, the wire diameter is defined by the size of the Au alloy particle. Therefore, the bulge morphology is presumably due to a change in Au particle size that may be attributed to transient supersaturation with group-III material. Several observations are of interest: (1) For the InGaAs-on-InP interface of Figure 5.2b and for other wire interfaces examined, a partial group-V exchange precedes the bulge; (2) The bulge coincides predominantly with changes in group-III composition; and (3) GaAsP/GaP heterointerfaces grown by the identical GS-MBE system, which involve only group-V elemental exchange at the interfaces, did not exhibit any bulge morphology [5.5].

Although not completely understood at present, a reasonable suggestion based on these observations is that the bulging is due to a transient group-III material supply associated with group-III supersaturation of the Au particle (as opposed to transient group-V material). Note that the presence of the bulge at the InGaAs-on-InP interface cannot be attributed to the increased growth rate (nominal 2D growth rate of 1 μm/hr for the InP segments compared to 1.88 μm/hr for the InGaAs segment) since a similar, albeit smaller, bulge is observed for the inverted InP-on-InGaAs interface where the growth rate is reduced. Growth oscillations exhibiting NW diameter fluctuations have been associated with twinning phenomena [5.17-19], an interplay of the wire geometry and the surface energies of the wire and Au particle [5.20], or continuous changes in contact angle or Rayleigh instability [5.21-23]. Unlike these previous studies, the "oscillation" (i.e., the bulge) in our NWs is confined to the material interfaces.

At the InP-to-InGaAs interface (region 2), the group-V elements seem to achieve equilibrium more rapidly than the group-III elements. As a result, at this interface, growth initially takes place by purging the Au particle of In atoms remaining from growth of the previous InP segment. Hence, the In profile of region 2-V remains nearly constant during the group-V transition. With the purging distance (the wire length between the initiation of the group-V transition and the initiation of the group-III transition) estimated as 11 nm and the average NW diameter estimated as 105 nm over this distance, the number of In atoms in this region can be approximated as 1.8 x 10^6. The Au particle can be modeled as a hemisphere having a diameter of 79 nm with an In-Au alloy composition of 46 atomic percent In as measured above. Based on a triclinic unit cell [5.24], the number of In atoms contained in the particle can be estimated as 0.8 x 10^6, reasonably close to the required amount.

It is unclear whether this purging takes place during the growth interruption or after the group-III flux is reestablished. Others have observed a reduction in wire diameter at the wire tip (pinching) due to purging of the Au particle under a group-V flux at the end of the growth of GaAs NWs [5.12, 25]. This effect is not explicitly observed at the interfaces analyzed in Figure 5.2. In our work, the bulging phenomena associated with group-III transients, or overgrowth on the NW sidewalls discussed in section 5.3.4, may mask any anticipated pinching effect.

5.3.3 InGaAs-to-InP Transition

After growth of the uniform InGaAs segment (region 3) was completed, an InGaAs-to-InP growth transition occurred (region 4). Though a similar gas-switching sequence was used, the resulting elemental transitions in Figure 5.2a are somewhat different when compared to the InP-to-InGaAs transition. The group-V transition is spread across the first ~40 nm of region 4 (region 4-V) with a nearly constant In and Ga concentration spanning ~33 nm. The Ga concentration drops rapidly over the latter ~15 nm of region 4 (region 4-III), leaving only In and P in region 5 as in region 1. Based on the earlier analysis of the InP-to-InGaAs transition (region 2), we surmise that growth in region 4 begins with a purging of the In and Ga remaining in the Au following completion of the previous InGaAs segment. The long, constant In and Ga levels at the start of the group-V transition support this assertion. Once again, a bulge at the top of the wire coincides with the onset of the group-III transition.

The group-V transition of region 4-V occurred over a thickness of ~40 nm, twice as long as the group-V transition of region 2-V (20 nm). In a previous MOVPE GaP/GaAs heterostructure wire study [5.6, 7] the authors observed a similar lengthening of the As-to-P group-V transition and suggested that the effect was due to residual AsH_3 that lingers in the growth chamber after gas-switching. Similarly, in the case of GS-MBE as in this work, significant concentrations of As_2 can remain after growth of the InGaAs section, leading to an As tail that prolongs the group-V transition [5.26, 27]. The results of a previous x-ray diffraction study of thin-film superlattices grown in the same GS-MBE system provide evidence of a slowly dropping As tail of about 5% As in the InP barriers [5.15]. This As carry-over effect is also supported by the photoluminescence analysis presented in Chapter 3.

A comparison can be made between the NWs and the equivalent 2D growth for the same incident materials and growth times. In the latter case the intended InGaAs section (regions 2 to 3) and the intended final InP section (regions 4 to 5) would each have had a 2D interface abruptness on the order of 1 ML (in terms of group-III) and a layer thickness of 33 nm [5.15]. In the NW, the group-III transition regions are significant, and the lengths of regions 2-3 and 4-5 are ~61 nm and ~78 nm, respectively; roughly double the corresponding 2D thicknesses. Catalytic growth is expected to be faster than 2D growth due to adatom collection by the Au particle [5.3]. The slightly slower growth rate of the final InP section of the NW is not unexpected. As the wire lengthens the rate of adatoms migrating from the sample surface is diminished, reducing the effect of this adatom pathway, and the associated growth rate.

5.3.4 Sidewall Growth

Radial EDS linescans of different regions of the wire gave information regarding sidewall growth. The EDS linescan along the bottom InP segment, shown in Figure 5.3, indicates that significant growth takes place on the InP sidewalls during growth of the InGaAs segment. Significant counts of both Ga and As are present at the edges of the

NW as well as detectable levels throughout the scan. Within about 5 atomic percent, the sidewall is estimated to contain 34, 16, 24, and 26 atomic percent of In, Ga, As, and P, respectively. This sidewall growth on the InP bottom segment occurs as an effect of the migration of adatoms from the substrate surface along the sides of the wire [5.3, 5]. P may be present in the sidewalls either due to some lingering P after growth of the bottom InP segment, or due to some further unresolved sidewall deposition during growth of the top InP segment.

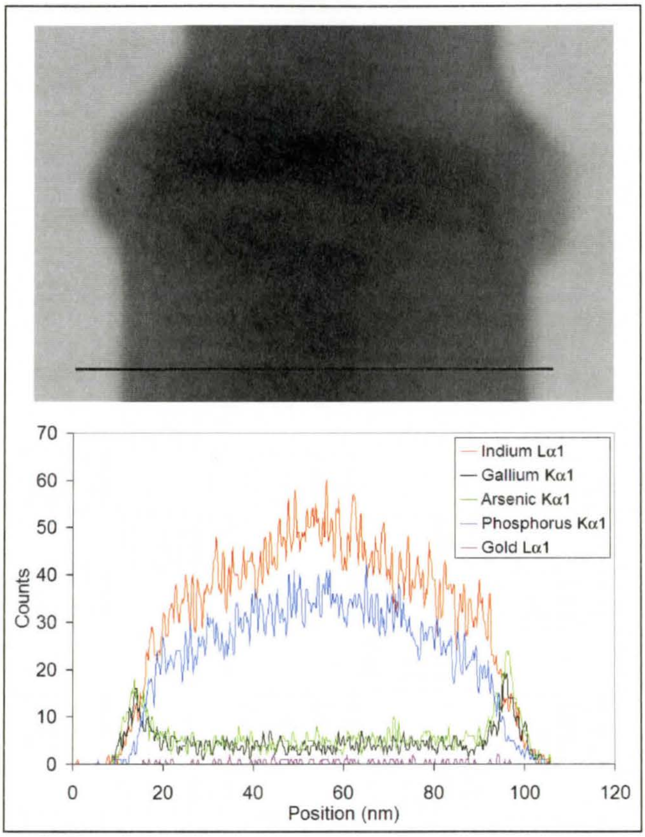

Figure 5.3. Radial linescan of the bottom InP segment of the NW shown in Figure 5.1c. The black line in the TEM image indicates the location of the scan line.

The sidewall growth was verified by HR-TEM imaging. Figure 5.4 shows a HR-TEM image of the bottom InP portion of the identical wire analyzed in Figures 2 and 3. The horizontal contrast lines perpendicular to the growth direction in Figure 5.4 are stacking faults observed frequently in (111)B oriented wires [5.28-30]. The InGaAs sidewall growth on InP is suggested by the lighter contrast along the outside of the wire, indicating a core-shell structure. This region measures about 6 nm in width, consistent with the full-width at half-maximum of the EDS peaks at the wire edge evident in Figure 5.3 (~5 nm).

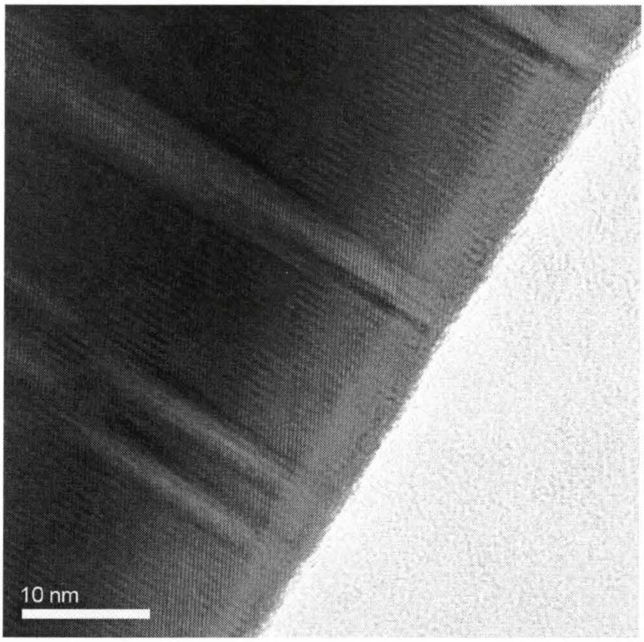

Figure 5.4. HR-TEM image of bottom InP portion of the NW shown in Figure 5.2 and Figure 5.3.

A radial EDS linescan of the top InP segment is shown in Figure 5.5. As expected, there is no evidence of InGaAs sidewall growth in this segment. In this case, no InGaAs sidewall growth is possible since the top InP segment is grown following completion of the InGaAs segment. Radial scans of the InGaAs section of one of these wires (not shown) showed no signs of P peaks due to InP sidewall growth. InP sidewall growth on the InGaAs sections was either too thin to detect or absent due to the ability of In adatoms to diffuse to the wire tip.

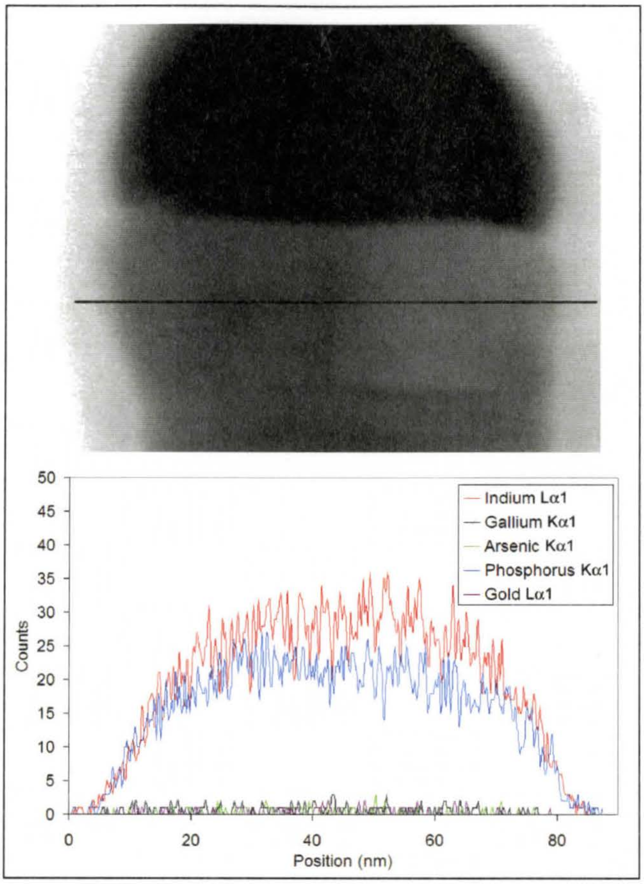

Figure 5.5. Radial EDS linescan of top InP portion of the NW shown in Figure 5.1c. The black line in the TEM image indicates the location of the scan line.

5.4 Chapter Summary

In contrast to the control of epitaxial film growth, variations in the EDS profile of InGaAs/InP heterostructure NWs grown by GS-MBE show that transient growth occurs during group-III switching at the material interfaces. The observed bulging morphology has been attributed to a transient group-III material supersaturation of the Au particle, and the exaggerated group-V exchange at the InGaAs-to-InP transition is due to the presence of residual As in the growth chamber after completion of the InGaAs segment. The Ga deficiency of the InGaAs section and the presence of significant InGaAs sidewall growth on the InP base are the result of the short diffusion length of Ga as compared to In.

6 Conclusions and Future Work

InGaAs/InP heterostructure nanowires were grown on *n*-type (111)B InP substrates by the vapor liquid solid growth mechanism, using Au as the metal catalyst, and gas source molecular beam epitaxy as the deposition method. The morphology of these wires was compared to pure InP nanowires grown in the same system. It was found that the InP NWs grew normal to the (111)B InP substrate with a uniform cross section (hexagonal rod-like shape) and sidewall facets aligned with the {-211} family of planes. These wires were also found to have stacking faults only near the wire tips, indicating that the wires grow free of stacking faults up to a height of ~300 nm. Since NW growth via MBE is diffusion induced, it is suggested that the onset of stacking faults results from changes to the supersaturation conditions of the Au particle due to the reduced rate at which source material reaches the Au-wire growth surface as the wire lengthens. It appears that the changing supersaturation conditions of the Au particle introduce a bistability in the crystal structure, which depends on growth method (GS-MBE versus MOVPE), III-V composition (As- versus P-containing alloys), and growth conditions (temperature and V/III flux ratio).

In contrast to the rod-like morphology of the InP NWs, the InGaAs/InP heterostructure NWs exhibited a distinct bulging morphology at the material interfaces. Based on the analysis of energy dispersive x-ray spectroscopy profiles these bulges are attributed to group-III transients in the Au catalyst during the gas-switching sequences. Sidewall growth of InGaAsP on the InP base and Ga deficiency in the InGaAs sections are caused by the low diffusion length of Ga compared to In adatoms.

A detailed structural model was developed to describe the material interfaces of InGaAs/InP superlattice structures grown by GS-MBE. A model consisting of 2 mixed group-V atomic layers at the InGaAs-on-InP interface and 1 mixed group-V atomic layer at the InP-on-InGaAs interface was supported by HRXRD and PL measurements. The results also indicated an As contamination of ~5% in the InP barriers due to residual As in the growth chamber after gas-switching. The asymmetric shape of the superlattice satellite peaks was not reproduced in the XRD simulations. Further simulations will be required to determine the cause of this rocking curve characteristic. The abruptness of the superlattice interfaces was compared to those of the InGaAs/InP heterostructure NWs and it was found that the VLS growth results in significant smearing of the interfaces due to the retarding effect of the Au catalyst particle on changes to the source material. The presence of a significant As tail in the top InP section of the heterostructure NWs is caused by residual As in the growth chamber as was the case in the SL growths.

Annealing experiments were also conducted on Au-covered GaAs and InP (111)B substrates to illustrate the link between the size distributions of the Au particles on annealed Au-covered substrates and NWs grown on the same surfaces. It was found that the same trends existed between InP and GaAs NWs, and InP and GaAs surfaces. However, deviations between the size and distribution of the Au particles and the resulting NWs are believed to be due to differences between the annealing processes occurring in the rapid thermal anneal and MBE chamber. To achieve a more appropriate comparison future annealing experiments should be conducted in the MBE chamber under a hydrogen plasma treatment as would be used before a NW growth. This would provide a more appropriate annealed surface to compare to the NW growths in terms of Au particle size distribution.

During the annealing experiment it was found that small areas of the Au-covered InP surface annealed at 550 °C were covered with nanowires several microns in length (Figure 6.1). These structures are notable since they were produced in the rapid thermal annealer at atmospheric pressure, not the ultra-high vacuum MBE system. These long nanowires were not observed in the lower temperature annealed surface (460 °C). The source material for these wires might come from the InP cap, but the reasons for growth and the composition of these structures has not yet been explored. Future experiments will be conducted to understand the growth mechanism of these structures.

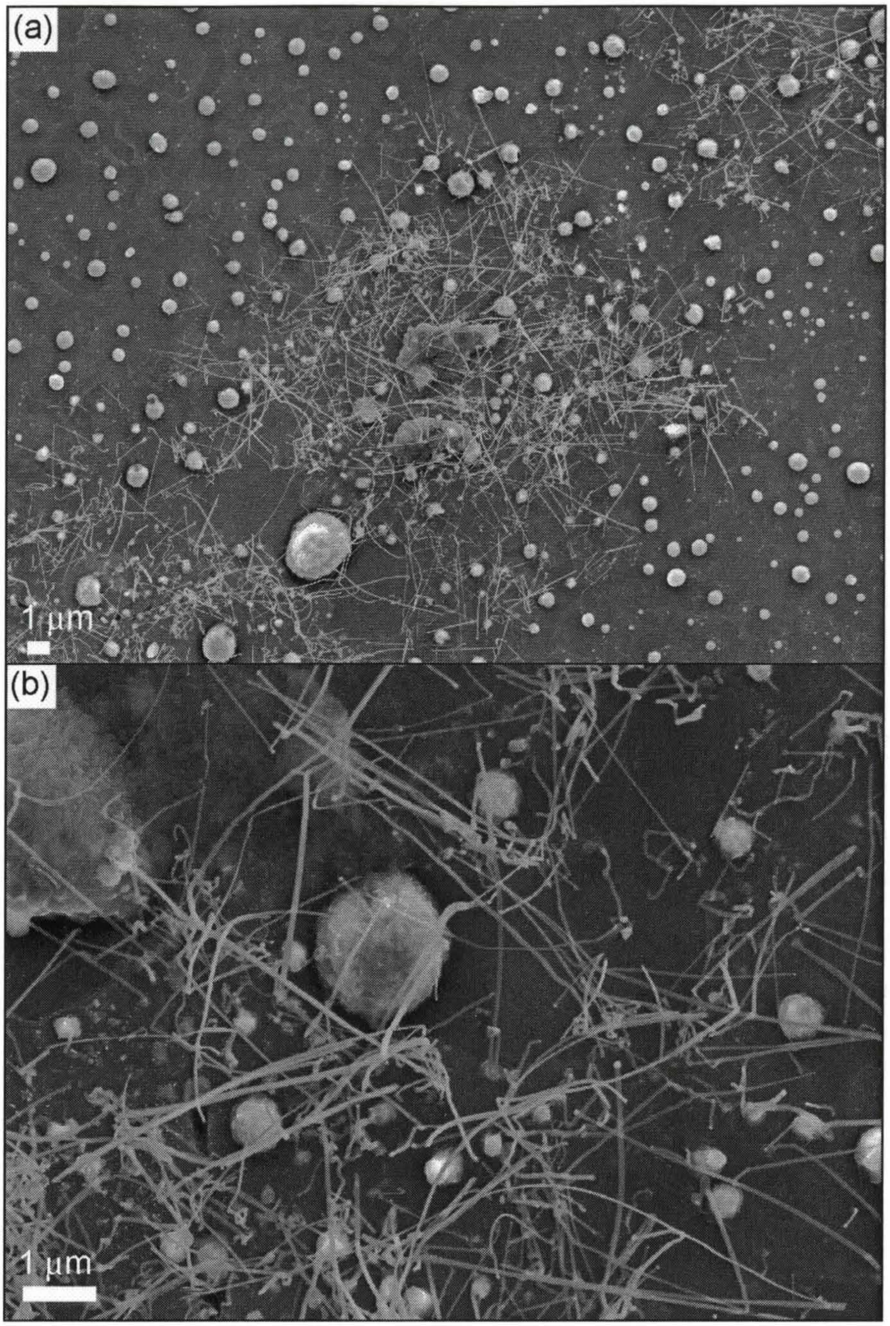

Figure 6.1. Secondary electron SEM images of nanowires grown in the rapid thermal annealer at atmospheric pressure. (a) 3,000 and (b) 10,000 times magnification.

To further elucidate the cause of the bulging, future growths will be conducted in which the growth of pure InP NWs is interrupted and resumed to simulate the gas-switching process without actually changing the source materials. The observation of bulging at the point of interruption would provide evidence that the bulging phenomenon is due to the slow purging of transient material from the catalyst and not changes to the source material. In the case that this interrupted InP NW growth shows no bulging, the growth of heterostructure NWs in which the group-III material remains constant (e.g. InAs/InP) will help to determine if the bulging and smearing observed at the interfaces is due to the interplay of different group-III materials in the Au catalyst or at the growth surface. Growths, in which the group-III material is changed but the group-V is not (e.g. InGaP/InP) will provide further evidence.

References

[1.1] Harriott L R, Proc IEEE **89**, 366 (2001).

[1.2] Frank D J, Dennard R H, Nowak E, Solomon P M, Taur Y and Wong H S P, Proc IEEE **89**, 259 (2001).

[1.3] Bjork M T, Ohlsson B J, Thelander C, Persson A I, Deppert K, Wallenberg L R and Samuelson L, Appl. Phys. Lett. **81**, 4458 (2002).

[1.4] Haraguchi K, Katsuyama T, Hiruma K and Ogawa K, Appl. Phys. Lett. **60**, 745 (1992).

[1.5] Gudiksen M S, Lauhon L J, Wang J, Smith D C and Lieber C M, Nature **415**, 617 (2002).

[1.6] Thelander C, Mårtensson T, Björk M T, Ohlsson B J, Larsson M W, Wallenberg L R and Samuelson L, Appl. Phys. Lett. **83**, 2052 (2003).

[1.7] Huang Y, Duan X F, Wei Q Q and Lieber C M, Science **291**, 630 (2001).

[1.8] Whang D, Jin S, Wu Y and Lieber C M, Nano Lett. **3**, 1255 (2003).

[1.9] Jin S, Whang D M, McAlpine M C, Friedman R S, Wu Y and Lieber C M, Nano Lett. **4**, 915 (2004).

[1.10] Huang Y, Duan X F, Cui Y, Lauhon L J, Kim K H and Lieber C M, Science **294**, 1313 (2001).

[1.11] Cui Y and Lieber C M, Science **291**, 851 (2001).

[1.12] Hahm J and Lieber C M, Nano Lett. **4**, 51 (2004).

[1.13] Patolsky F, Zheng G and Lieber C M, Nanomedicine **1**, 51 (2006).

[1.14] Duan X F, Huang Y, Agarwal R and Lieber C M, Nature **421**, 241 (2003).

[1.15] Barrelet C J, Greytak A B and Lieber C M, Nano Lett. **4**, 1981 (2004).

[1.16] Huang Y, Duan X F and Lieber C M, Small **1**, 142 (2005).

[1.17] Huang M H, Mao S, Feick H, Yan H Q, Wu Y Y, Kind H, Weber E, Russo R and Yang P D, Science **292**, 1897 (2001).

[1.18] Pettersson H, Trägårdh J, Persson A I, Landin L, Hessman D and Samuelson L, Nano Lett. **6**, 229 (2006).

[1.19] Greytak A B, Barrelet C J, Li Y and Lieber C M, Appl. Phys. Lett. **87**, 151103 (2005).

[1.20] Bakkers E P A M, van Dam J A, De Franceschi S, Kouwenhoven L P, Kaiser M, Verheijen M, Wondergem H and van der Sluis P, Nat. Mater. **3**, 769 (2004).

[1.21] Watanabe Y, Hibino H, Bhunia S, Tateno K and Sekiguchi T, Physica E **24**, 133 (2004).

[1.22] Khorenko V, Regolin I, Neumann S, Prost W, Tegude F J and Wiggers H, Appl. Phys. Lett. **85**, 6407 (2004).

[1.23] Yazawa M, Koguchi M and Hiruma K, Appl. Phys. Lett. **58**, 1080 (1991).

[1.24] Watanabe Y, Bhunia S, Fujikawa S, Kawamura T, Nakashima H, Furukawa K and Torimitsu K, Thin Solid Films **464-65**, 248 (2004).

[1.25] Chuang L C, Moewe M, Chase C, Kobayashi N P, Chang-Hasnain C and Crankshaw S, Appl. Phys. Lett. **90**, 043115 (2007).

[1.26] Kim Y, Joyce H J, Gao O, Tan H H, Jagadish C, Paladugu M, Zou J and Suvorova A A, Nano Lett. **6**, 599 (2006).

[1.27] Sudfeld D, Regolin J, Kastner J, Dumpich G, Khorenko V, Prost W and Tegude F J, Phase Transit. **79**, 727 (2006).

[1.28] Wagner R S and Ellis W C, Appl. Phys. Lett. **4**, 89 (1964).

[1.29] Hiruma K, Yazawa M, Katsuyama T, Ogawa K, Haraguchi K, Koguchi M and Kakibayashi H, J. Appl. Phys. **77**, 447 (1995).

[1.30] Duan X F and Lieber C M, Adv Mater **12**, 298 (2000).

[1.31] Bhunia S, Kawamura T, Fujikawa S and Watanabe Y, Physica E **24**, 138 (2004).

[1.32] Plante M C and LaPierre R R, J. Cryst. Growth **286**, 394 (2006).

[1.33] Dubrovskii V G, Cirlin G E, Soshnikov I P, Tonkikh A A, Sibirev N V, Samsonenko Y B and Ustinov V M, Phys. Rev. B **71**, 205325 (2005).

[1.34] Dubrovskii V G, Sibirev N V, Cirlin G E, Harmand J C and Ustinov V M, Phys Rev E. **73**, 021603 (2006).

[1.35] Schubert L, Werner P, Zakharov N D, Gerth G, Kolb F M, Long L, Gosele U and Tan T Y, Appl. Phys. Lett. **84**, 4968 (2004).

[1.36] Bhunia S, Kawamura T, Fujikawa S, Nakashima H, Furukawa K, Torimitsu K and Watanabe Y, Thin Solid Films **464-65**, 244 (2004).

[1.37] Krishnamachari U, Borgstrom M, Ohlsson B J, Panev N, Samuelson L, Seifert W, Larsson M W and Wallenberg L R, Appl. Phys. Lett. **85**, 2077 (2004).

[1.38] Mattila M, Hakkarainen T, Mulot M and Lipsanen H, Nanotechnology **17**, 1580 (2006).

[1.39] Seifert W, Borgström M, Deppert K, Dick K A, Johansson J, Larsson M W, Mårtensson T, Skold N, Svensson C P T, Wacaser B A, Wallenberg L R and Samuelson L, J. Cryst. Growth **272**, 211 (2004).

[1.40] Lu W and Lieber C M, J. Phys. D-Appl. Phys. **39**, R387 (2006).

[1.41] Herman M A and Sitter H, "Molecular Beam Epitaxy: Fundamentals and Current Status", (Springer-Verlag, New York, 1996), Chap. 1, pp. 1-32.

[1.42] Cornet D M, LaPierre R R, Comedi D and Pusep Y A, J. Appl. Phys. **100**, 043518 (2006).

[1.43] Cornet D M, Mazzetti V G M and LaPierre R R, Appl. Phys. Lett. **90**, 013116 (2007).

[2.1] Herman M A and Sitter H, "Molecular Beam Epitaxy: Fundamentals and Current Status", (Springer-Verlag, New York, 1996), Chap. 1, pp. 1-32.

[2.2] Grange J D, "Technology and Physics of Molecular Beam Epitaxy", (Plenum Press, New York, 1985), Chap. 3, pp. 47-60.

[2.3] Bowen D K and Tanner B K, "High Resolution X-ray Diffractometry and Topography", (Taylor & Francis, United Kingdom, 1998), Chap. 2, pp. 14-49.

[2.4] Bowen D K and Tanner B K, "High Resolution X-ray Diffractometry and Topography", (Taylor & Francis, United Kingdom, 1998), Chap. 1, pp. 1-13.

[2.5] Bowen D K and Tanner B K, "High Resolution X-ray Diffractometry and Topography", (Taylor & Francis, United Kingdom, 1998), pp. 55-56.

[2.6] Bowen D K and Tanner B K, "High Resolution X-ray Diffractometry and Topography", (Taylor & Francis, United Kingdom, 1998), pp. 141-142.

[2.7] Fewster P F, Semicond. Sci. Technol. **8**, 1915 (1993).

[2.8] Perkowitz S, "Optical Characterization of Semiconductors: Infrared, Raman, and Photoluminescence Spectroscopy", (Academic Press, San Diego, 1993), Chap. 4.3, pp. 50-54.

[2.9] Reimer L, "Scanning Electron Microscopy: Physics of Image Formation and Microanalysis", (Springer-Verlag, Heidelberg, 1985), Chap. 1.2, pp. 3-7.

[2.10] Egerton R F, "Physical Principles of Electron Microscopy: An Introduction to TEM, SEM, and AEM", (Springer, New York, 2005), Chap. 5.3, pp. 131-136.

[2.11] Egerton R F, "Physical Principles of Electron Microscopy: An Introduction to TEM, SEM, and AEM", (Springer, 2005), Chap. 5.4, pp. 137-139.

[2.12] Egerton R F, "Physical Principles of Electron Microscopy: An Introduction to TEM, SEM, and AEM", (Springer, New York, 2005), Chap. 5.1, pp. 125-129.

[2.13] Reimer L, "Scanning Electron Microscopy: Physics of Image Formation and Microanalysis", (Springer-Verlag, Heidelberg, 1985), Chap. 2.2, pp. 20-36.

[2.14] Reimer L, "Scanning Electron Microscopy: Physics of Image Formation and Microanalysis", (Springer-Verlag, Heidelberg, 1985), Chap. 5.1, pp. 176-185.

[2.15] Reimer L, "Transmission Electron Microscopy: Physics of Image Formation and Microanalysis", (Springer-Verlag, Heidelberg, 1984), Chap. 1.1, pp. 1-8.

[2.16] Reimer L, "Transmission Electron Microscopy: Physics of Image Formation and Microanalysis", (Springer-Verlag, Heidelberg, 1984), Chap. 4.4, pp. 112-120.

[2.17] Egerton R F, "Physical Principles of Electron Microscopy: An Introduction to TEM, SEM, and AEM", (Springer, New York, 2005), Chap. 3.6, pp. 78-88.

[2.18] Reimer L, "Transmission Electron Microscopy: Physics of Image Formation and Microanalysis", (Springer-Verlag, Heidelberg, 1984), Chap. 5, pp. 135-184.

[2.19] Garratt-Reed A J and Bell D C, "Energy-Dispersive X-Ray Analysis in the Electron Microscope", (BIOS Scientific Publishers Limited, Oxford, 2003), Vol. 49, Chap. 2.1.1, pp. 5-7.

[2.20] Egerton R F, "Physical Principles of Electron Microscopy: An Introduction to TEM, SEM, and AEM", (Springer, New York, 2005), Chap. 2.2, pp. 10-12.

[2.21] Egerton R F, "Physical Principles of Electron Microscopy: An Introduction to TEM, SEM, and AEM", (Springer, New York, 2005), Chap. 2.3, pp. 12-13.

[2.22] INCA: The Microanalysis Suite - Issue 14, **version 4.04,** Oxford Instruments Analytical Limited, (2003).

[2.23] DigitalMicrograph, **version 3.10.1,** Gatan Inc., Pleasantson, CA, USA, (1996-2003).

[3.1] Smith D L and Mailhiot C, J. Appl. Phys. **62**, 2545 (1987).

[3.2] Aifer E H, Jackson E M, Boishin G, Whitman L J, Vurgaftman I, Meyer J R, Culbertson J C and Bennett B R, Appl. Phys. Lett. **82**, 4411 (2003).

[3.3] Johnson J L, Samoska L A, Gossard A C, Merz J L, Jack M D, Chapman G R, Baumgratz B A, Kosai K and Johnson S M, J. Appl. Phys. **80**, 1116 (1996).

[3.4] Mohseni H, Tahraoui A, Wojkowski J, Razeghi M, Brown G J, Mitchel W C and Park Y S, Appl. Phys. Lett. **77**, 1572 (2000).

[3.5] Beltram F, Allam J, Capasso F, Koren U and Miller B, Appl. Phys. Lett. **50**, 1170 (1987).

[3.6] Rajamani V and Chakrabarti P, Opt. Quant. Electron. **31**, 69 (1999).

[3.7] Benzaquen R, Roth A P and Leonelli R, J. Appl. Phys. **79**, 2640 (1996).

[3.8] Vandenberg J M, Macrander A T, Hamm R A and Panish M B, Phys. Rev. B **44**, 3991 (1991).

[3.9] Krost A, Bohrer J, Roehle H and Bauer G, Appl. Phys. Lett. **64**, 469 (1994).

[3.10] McKay H A, Feenstra R M, Poole P J and Aers G C, J. Cryst. Growth **249**, 437 (2003).

[3.11] Sherwin M E, Terry F L, Munns G O, Herman J S, Woelk E G and Haddad G I, J Electron Mater **21**, 269 (1992).

[3.12] Francesio L, Franzosi P and Landgren G, Journal of Physics D-Applied Physics **28**, A169 (1995).

[3.13] Camassel J, Laurenti J P, Juillaguet S, Reinhardt F, Wolter K, Kurz H and Grutzmacher D, J. Cryst. Growth **107**, 543 (1991).

[3.14] Vandenberg J M, Panish M B, Hamm R A and Temkin H, Appl. Phys. Lett. **56**, 910 (1990).

[3.15] Vandenberg J M, Chu S N G, Hamm R A, Panish M B and Temkin H, Appl. Phys. Lett. **49**, 1302 (1986).

[3.16] Shiau G J, Chao C P, Burrows P E and Forrest S R, J. Appl. Phys. **77**, 201 (1995).

[3.17] Leys M R, Rongen R T H, Hopkins J, Vonk H, Vanes C M, Wolter J H and Tichelaar F D, J. Cryst. Growth **150**, 633 (1995).

[3.18] Bede RADS Mercury, **version 3.88,** Bede Scientific Instruments Ltd., Bowburn South Industrial Estate, Bowburn, Durham, England.

[3.19] Wormington M, Panaccione C, Matney K M and Bowen D K, Philos. Trans. R. Soc. Lond. Ser. A-Math. Phys. Eng. Sci. **357**, 2827 (1999).

[3.20] Bartels W J, "Thin Film Growth Techniques for Low-Dimensional Structures", (Plenum Press, New York, 1987), Vol. 163, pp. 441-458.

[3.21] Bartels W J, Hornstra J and Lobeek D J W, Acta Crystallogr. Sect. A **42**, 539 (1986).

[3.22] Lakshmi B, Robinson B J, Cassidy D T and Thompson D A, J. Appl. Phys. **81**, 3616 (1997).

[3.23] LaPierre R R, Robinson B J and Thompson D A, J. Appl. Phys. **79**, 3021 (1996).

[3.24] Pusep Y A, Rodrigues A D, Galzerani J C, Comet D M, Comedi D and LaPierre R R, Phys. Rev. B **73**, 235344 (2006).

[3.25] Pusep Y A, Dasilva S W, Galzerani J C, Lubyshev D I and Basmaji P, Phys. Rev. B **51**, 9891 (1995).

[3.26] Seifert W, Liu X and Samuelson L, Appl. Phys. Lett. **62**, 949 (1993).

[3.27] Chen H J, Feenstra R M, Piva P G, Goldberg R D, Mitchell I V, Aers G C, Poole P J and Charbonneau S, Appl. Phys. Lett. **75**, 79 (1999).

[3.28] Mozume T, Kashima H, Hosomi K, Ouchi K, Sato H, Masuda H, Tanoue T and Ohbu I, J. Vac. Sci. Technol. B **13**, 276 (1995).

[3.29] Muraki K, Fukatsu S, Shiraki Y and Ito R, Appl. Phys. Lett. **61**, 557 (1992).

[3.30] Lourenco S A, Dias I F L, Duarte J L, Laureto E, Pocas L C, Filho D O T and Leite J R, Braz. J. Phys. **34**, 517 (2004).

[3.31] Pankove J I, "Optical Processes in Semiconductors", (Dover Publications, Inc, New York, 1971), Chap. 7, pp. 160-169.

[3.32] Lourenco S A, Dias I F L, Duarte J L, Laureto E, Meneses E A, Leite J R and Mazzaro I, J. Appl. Phys. **89**, 6159 (2001).

[3.33] Pankove J I, "Optical Processes in Semiconductors", (Dover Publications, Inc, New York, 1971), Chap. 2-B, pp. 27-28.

[3.34] LaPierre R R, Okada T, Robinson B J, Thompson D A and Weatherly G C, J. Cryst. Growth **158**, 6 (1996).

[3.35] LaPierre R R, Robinson B J and Thompson D A, Appl. Surf. Sci. **90**, 437 (1995).

[3.36] Onabe K, Japanese Journal of Applied Physics Part 1-Regular Papers Short Notes & Review Papers **21**, 797 (1982).

[3.37] Bastard G, "Wave Mechanics Applied to Semiconductor Heterostructures", (Halsted Press, France, 1988), pp. 63-117.

[3.38] Vurgaftman I, Meyer J R and Ram-Mohan L R, J. Appl. Phys. **89**, 5815 (2001).

[3.39] Murphy R D and Phillips J M, Am. J. Phys. **44**, 574 (1976).

[3.40] Pankove J I, "Optical Processes in Semiconductors", (Dover Publications, Inc, New York, 1971), Chap. 6-D-2-a, pp. 124-126.

[3.41] Zielinski E, Schweizer H, Streubel K, Eisele H and Weimann G, J. Appl. Phys. **59**, 2196 (1986).

[3.42] Pocas L C, Lopes E M, Duarte J L, Dias I F L, Lourenco S A, Laureto E, Valadares M, Guimaraes P S S, Cury L A and Harmand J C, J. Appl. Phys. **97**, 103518 (2005).

[3.43] Pocas L C, Duarte J L, Lopes E M, Dias I F L, Laureto E, Cesar D F and Harmand J C, J. Appl. Phys. **100**, 053519 (2006).

[3.44] Pierret R F, "Advanced Semiconductor Fundamentals", (Addison-Wesley Publishing Company, Reading, Massachusetts, 1989), Vol. 6, Chap. 3, pp. 53-90.

[4.1] Bhunia S, Kawamura T, Fujikawa S, Nakashima H, Furukawa K, Torimitsu K and Watanabe Y, Thin Solid Films **464-65**, 244 (2004).

[4.2] Krishnamachari U, Borgstrom M, Ohlsson B J, Panev N, Samuelson L, Seifert W, Larsson M W and Wallenberg L R, Appl. Phys. Lett. **85**, 2077 (2004).

[4.3] Mattila M, Hakkarainen T, Mulot M and Lipsanen H, Nanotechnology **17**, 1580 (2006).

[4.4] Seifert W, Borgström M, Deppert K, Dick K A, Johansson J, Larsson M W, Mårtensson T, Skold N, Svensson C P T, Wacaser B A, Wallenberg L R and Samuelson L, J. Cryst. Growth **272**, 211 (2004).

[4.5] Watanabe Y, Bhunia S, Fujikawa S, Kawamura T, Nakashima H, Furukawa K and Torimitsu K, Thin Solid Films **464-65**, 248 (2004).

[4.6] Akiyama T, Sano K, Nakamura K and Ito T, Jpn. J. Appl. Phys. Part 2 - Lett. Express Lett. **45**, L275 (2006).

[4.7] Plante M C and LaPierre R R, J. Cryst. Growth **286**, 394 (2006).

[4.8] Dubrovskii V G, Cirlin G E, Soshnikov I P, Tonkikh A A, Sibirev N V, Samsonenko Y B and Ustinov V M, Phys. Rev. B **71**, 205325 (2005).

[4.9] Schubert L, Werner P, Zakharov N D, Gerth G, Kolb F M, Long L, Gosele U and Tan T Y, Appl. Phys. Lett. **84**, 4968 (2004).

[4.10] W. S. Rasband, ImageJ, **version 1.37,** U. S. National Institutes of Health, Bethesda, Maryland, USA, http://rsb.info.nih.gov/ij/, (1997-2006).

[4.11] T. Knoll, M. Hamburg and M. Pawliger, Adobe Photoshop Elements, **version 1.0,** Adobe Systems Incorporated, (1989-2001).

[4.12] Kim Y, Joyce H J, Gao O, Tan H H, Jagadish C, Paladugu M, Zou J and Suvorova A A, Nano Lett. **6**, 599 (2006).

[4.13] Verschuren C A, Leys M R, Vonk H and Wolter J H, Appl. Phys. Lett. **74**, 2197 (1999).

[4.14] Egerton R F, "Physical Principles of Electron Microscopy: An Introduction to TEM, SEM, and AEM", (Springer, 2005), Chap. 5.4, pp. 137-139.

[4.15] Johansson J, Karlsson L S, Svensson C P T, Mårtensson T, Wacaser B A, Deppert K, Samuelson L and Seifert W, Nat. Mater. **5**, 574 (2006).

[4.16] Soshnikov I P, Cirlin G E, Tonkikh A A, Samsonenko Y B, Dubovskii V G, Ustinov V M, Gorbenko O M, Litvinov D and Gerthsen D, Phys. Solid State **47**, 2213 (2005).

[4.17] Hiruma K, Yazawa M, Katsuyama T, Ogawa K, Haraguchi K, Koguchi M and Kakibayashi H, J. Appl. Phys. **77**, 447 (1995).

[4.18] Milliron D J, Hughes S M, Cui Y, Manna L, Li J B, Wang L W and Alivisatos A P, Nature **430**, 190 (2004).

[4.19] Chen C, Plante M C, Fradin C and LaPierre R R, J. Mater. Res. **21**, 2801 (2006).

[4.20] Verheijen M A, Immink G, de Smet T, Borgström M T and Bakkers E P A M, J. Am. Chem. Soc. **128**, 1353 (2006).

[5.1] Kim Y, Joyce H J, Gao O, Tan H H, Jagadish C, Paladugu M, Zou J and Suvorova A A, Nano Lett. **6**, 599 (2006).

[5.2] Sudfeld D, Regolin J, Kastner J, Dumpich G, Khorenko V, Prost W and Tegude F J, Phase Transit. **79**, 727 (2006).

[5.3] Plante M C and LaPierre R R, J. Cryst. Growth **286**, 394 (2006).

[5.4] Cornet D M, Mazzetti V G M and LaPierre R R, Appl. Phys. Lett. **90**, 013116 (2007).

[5.5] Chen C, Plante M C, Fradin C and LaPierre R R, J. Mater. Res. **21**, 2801 (2006).

[5.6] Verheijen M A, Immink G, de Smet T, Borgström M T and Bakkers E P A M, J. Am. Chem. Soc. **128**, 1353 (2006).

[5.7] Borgström M T, Verheijen M A, Immink G, de Smet T and Bakkers E P A M, Nanotechnology **17**, 4010 (2006).

[5.8] Regolin I, Sudfeld D, Lüttjohann S, Khorenko V, Prost W, Kästner J, Dumpich G, Meier C, Lorke A and Tegude F J, Journal of Crystal Growth **298**, 607 (2007).

[5.9] Wu Z H, Mei X, Kim D, Blumin M, Ruda H E, Liu J Q and Kavanagh K L, Appl. Phys. Lett. **83**, 3368 (2003).

[5.10] Bjork M T, Ohlsson B J, Sass T, Persson A I, Thelander C, Magnusson M H, Deppert K, Wallenberg L R and Samuelson L, Appl. Phys. Lett. **80**, 1058 (2002).

[5.11] Dick K A, Deppert K, Karlsson L S, Wallenberg L R, Samuelson L and Seifert W, Adv. Funct. Mater. **15**, 1603 (2005).

[5.12] Persson A I, Larsson M W, Stenström S, Ohlsson B J, Samuelson L and Wallenberg L R, Nat. Mater. **3**, 677 (2004).

[5.13] Okamoto H, J. Phase Equilib. Diffus. **25**, 197 (2004).

[5.14] INCA: The Microanalysis Suite - Issue 14, **version 4.04,** Oxford Instruments Analytical Limited, (2003).

[5.15] Cornet D M, LaPierre R R, Comedi D and Pusep Y A, J. Appl. Phys. **100**, 043518 (2006).

[5.16] Verschuren C A, Leys M R, Vonk H and Wolter J H, Appl. Phys. Lett. **74**, 2197 (1999).

[5.17] Johansson J, Karlsson L S, Svensson C P T, Mårtensson T, Wacaser B A, Deppert K, Samuelson L and Seifert W, Nat. Mater. **5**, 574 (2006).

[5.18] Xiong Q H, Wang J and Eklund P C, Nano Lett. **6**, 2736 (2006).

[5.19] Hao Y F, Meng G W, Wang Z L, Ye C H and Zhang L D, Nano Lett. **6**, 1650 (2006).

[5.20] Ross F M, Tersoff J and Reuter M C, Phys. Rev. Lett. **95**, 146104 (2005).

[5.21] Givargizov E I, J. Cryst. Growth **31**, 20 (1975).

[5.22] Zhang H Z, Yu D P, Ding Y, Bai Z G, Hang Q L and Feng S Q, Appl. Phys. Lett. **73**, 3396 (1998).

[5.23] Peng H Y, Wang N, Shi W S, Zhang Y F, Lee C S and Lee S T, J. Appl. Phys. **89**, 727 (2001).

[5.24] Pearson W B, "A Handbook of Lattice Spacings and Structures of Metals and Alloys", (Pergamon Press, 1967), Vol. 2, pp. 153-154.

[5.25] Harmand J C, Patriarche G, Pere-Laperne N, Merat-Combes M N, Travers L and Glas F, Appl. Phys. Lett. **87**, 203101 (2005).

[5.26] Seifert W, Liu X and Samuelson L, Appl. Phys. Lett. **62**, 949 (1993).

[5.27] Chen H J, Feenstra R M, Piva P G, Goldberg R D, Mitchell I V, Aers G C, Poole P J and Charbonneau S, Appl. Phys. Lett. **75**, 79 (1999).

[5.28] Watanabe Y, Bhunia S, Fujikawa S, Kawamura T, Nakashima H, Furukawa K and Torimitsu K, Thin Solid Films **464-65**, 248 (2004).

[5.29] Mattila M, Hakkarainen T, Mulot M and Lipsanen H, Nanotechnology **17**, 1580 (2006).

[5.30] Krishnamachari U, Borgstrom M, Ohlsson B J, Panev N, Samuelson L, Seifert W, Larsson M W and Wallenberg L R, Appl. Phys. Lett. **85**, 2077 (2004).